REPORT DOCUMENTATION PAGE

Form Approved OMB NO. 0704-0188

1. REPORT DATE (DD-MM-YYYY)	2. REPORT TYPE	3. DATES COVERED (From - To)
16-07-2018	Final Report	13-May-2015 - 12-May-2018

4. TITLE AND SUBTITLE
Final Report: Control of Static and Dynamic Stall in a Wide Range of Mach Numbers by Plasma Actuators with Combined Energy/Momentum Action

5a. CONTRACT NUMBER
W911NF-15-1-0236

5b. GRANT NUMBER

5c. PROGRAM ELEMENT NUMBER
611102

6. AUTHORS

5d. PROJECT NUMBER

5e. TASK NUMBER

5f. WORK UNIT NUMBER

7. PERFORMING ORGANIZATION NAMES AND ADDRESSES
Princeton University
PO Box 36
87 Prospect Avenue, Second Floor
Princeton, NJ 08544 -2020

8. PERFORMING ORGANIZATION REPORT NUMBER

9. SPONSORING/MONITORING AGENCY NAME(S) AND ADDRESS (ES)
U.S. Army Research Office
P.O. Box 12211
Research Triangle Park, NC 27709-2211

10. SPONSOR/MONITOR'S ACRONYM(S)
ARO

11. SPONSOR/MONITOR'S REPORT NUMBER(S)
64561-EG.8

12. DISTRIBUTION AVAILIBILITY STATEMENT
Approved for public release; distribution is unlimited.

13. SUPPLEMENTARY NOTES
The views, opinions and/or findings contained in this report are those of the author(s) and should not contrued as an official Department of the Army position, policy or decision, unless so designated by other documentation.

14. ABSTRACT

15. SUBJECT TERMS

16. SECURITY CLASSIFICATION OF:			17. LIMITATION OF ABSTRACT	15. NUMBER OF PAGES	19a. NAME OF RESPONSIBLE PERSON
a. REPORT	b. ABSTRACT	c. THIS PAGE			Richard Miles
UU	UU	UU	UU		19b. TELEPHONE NUMBER 609-258-5131

Standard Form 298 (Rev 8/98)
Prescribed by ANSI Std. Z39.18

RPPR Final Report
as of 18-Oct-2018

Agency Code:

Proposal Number: 64561EG **Agreement Number: W911NF-15-1-0236**
INVESTIGATOR(S):

Name: Richard Miles
Email: miles@princeton.edu
Phone Number: 6092585131
Principal: Y

Organization: **Princeton University**
Address: PO Box 36, Princeton, NJ 085442020
Country: USA
DUNS Number: 002484665 EIN: 210634501

Report Date: 12-Aug-2018 Date Received: 16-Jul-2018

Final Report for Period Beginning 13-May-2015 and Ending 12-May-2018
Title: Control of Static and Dynamic Stall in a Wide Range of Mach Numbers by Plasma Actuators with Combined Energy/Momentum Action
Begin Performance Period: 13-May-2015 **End Performance Period:** 12-May-2018
Report Term: 0-Other

Submitted By: Richard Miles Email: miles@princeton.edu
Phone: (609) 258-5131

Distribution Statement: 1-Approved for public release; distribution is unlimited.

STEM Degrees: 1 **STEM Participants:** 3

Major Goals: High speed helicopters must accommodate significant changes in the rotor lift performance as a function of rotor angle. The advancing blade can achieve transonic conditions while the retreating blade experiences relatively low speed. The high Mach number of the advancing blade requires an angle of attack below 5 degrees for maximum lift, whereas the retreating blade requires high an angle of attack in excess of 10 degrees. Under high speed and high load conditions, stall occurs during the retreating cycle and destabilizes the aircraft. Thus operation requires that the angle of attack of the blades be changed during the cycle and optimized with flight speed. The focus of this research is to determine to what degree plasma actuators can be used to optimize high speed flight performance, particularly focusing on suppressing the dynamic stall by retreating blade separation control and increasing lift.

Accomplishments: This study is the first demonstration of dynamic stall control for reversed flow over an airfoil, as well as a demonstration of stall control at higher velocities than previously recorded. Wind tunnel testing of SDBD plasma actuators at V = 50-150 mph was performed. An increase in the critical stall angle of attack (from 12 to 25 degrees) was observed at a discharge power ~5 W/m for static and dynamic stall conditions. Fast response time was demonstrated. Dynamic stall control using NS SDBD was demonstrated. It was shown that low-energy actuation could increase the integral lift force by more than 10% and prevent the abrupt lift force decrease when the blade reaches the critical value of the angle of attack. Dynamic stall control by NS SDBD plasma actuators was shown for the first time for normal and reverse flow configuration. Lift force increase up to 40% was demonstrated for both forward and reverse flow for angles of attack up to 32 degrees for flow speed 20-70 m/s. A lift force increase up to 20% in a hover mode of a model helicopter was demonstrated for fixed engine power.
A new SiC diodes-based array was designed and fabricated under DURIP support and tested under this effort as a method to increase the induced jets velocity. The sequential element "pull-it forward" concept of SDBD performance enhancement was developed and tested. Momentum generation by synchronized NS-SDBD was demonstrated. The "microblast" SDBD flow control technology was demonstrated using 4-electrode SDBD synchronization over a microsecond time scale.
The new Femtosecond Laser Electronic Excitation Tagging (FLEET) method was used to follow the dynamics of the air flow and separation over the air foil as the angle of attack is varies.

RPPR Final Report
as of 18-Oct-2018

Training Opportunities: Graduate student support
Kris Meehan
Undergraduate Princeton senior thesis project on ozone measurement
Madelyn Baron class of 2018
Rutgers undergraduate student summer training project on model helicopter lift increase
Nikita Persikov class of 2020

Results Dissemination:
1. Kiyoshi Kinefuchi, Andrey Starikovskiy, and Richard B. Miles. Control of Shock- Wave/Boundary-Layer Interaction Using Nanosecond-Pulsed Plasma Actuators. Journal of Propulsion and Power, Vol. 34, No. 4, July–August 2018.
2. Nikolay Aleksandrov, Andrey Starikovskiy. Ozone formation and energy transfer mechanisms in nonequilibrium plasma of ns-SDBD. Plasma Sources Science and Technology. 2018. Submitted.
3. Andrey Starikovskiy, Nikita Persikov, Kristofer Meehan, Richard B. Miles. Static and Dynamic Stall Control by NS SDBD Actuators. Plasma Sources Science and Technology. 2018. Submitted.
4. Andrey Starikovskiy, Kristofer Meehan, and Richard B. Miles. Dynamic Stall Control by NS SDBD Actuator, 2018 AIAA Aerospace Sciences Meeting, AIAA SciTech Forum, (AIAA 2018-0681)
5. Andrey Starikovskiy, Nikita Persikov, and Richard B. Miles. Helicopter Lift Force Increase in Hover Mode by NS-SDBD Plasma Actuators, 2018 AIAA Aerospace Sciences Meeting, AIAA SciTech Forum, (AIAA 2018-0936)
6. Andrey Starikovskiy, Kristofer Meehan, Arthur Dogariu, Richard B. Miles. Dynamic Stall Control at High Angle of Attack by NS pulsed Actuator in Burst Mode (AIAA 2017- 3342) 48th AIAA Plasmadynamics and Lasers Conference, 2017, 10.2514/6.2017-3342
7. Andrey Starikovskiy, Kristofer Meehan, Julian Williams, Richard B. Miles. NS Dielectric Barrier Discharge Development and Thrust Generation in 4-Electrode Geometry (AIAA 2017-3344) 48th AIAA Plasmadynamics and Lasers Conference, 2017, 10.2514/6.2017- 3344
8. Andrey Starikovskiy, Richard B. Miles. Dielectric Barrier Discharge Control and Thrust Enhancement by Diode Surface (AIAA 2017-4159) 48th AIAA Plasmadynamics and Lasers Conference, 2017, 10.2514/6.2017-4159
9. Andrey Starikovskiy, Kristofer Meehan, Julian Williams, Richard B. Miles. Static and Dynamic Stall Control at High Angle of Attack by NS pulsed Actuator in Burst Mode (AIAA 2017-1342) 55th AIAA Aerospace Sciences Meeting, 2017, 10.2514/6.2017-1342
10. Andrey Starikovskiy, Richard B. Miles. Experimental Investigation of Dynamic Stall Control in a Wide Range of Mach Numbers by Plasma Actuators (AIAA 2016-4017) 47th AIAA Plasmadynamics and Lasers Conference, 2016, 10.2514/6.2016-4017
11. Andrey Starikovskiy, Richard B. Miles. Plasma Actuators with Combined Energy/Momentum Action (AIAA 2016-4017) 54th AIAA Aerospace Sciences Meeting, 2016, 10.2514/6.2016-0452

Honors and Awards: Nothing to Report

Protocol Activity Status:

Technology Transfer: Nothing to Report

PARTICIPANTS:

Participant Type: PD/PI
Participant: Richard B Miles
Person Months Worked: 1.00 **Funding Support:**
Project Contribution:
International Collaboration:
International Travel:
National Academy Member: Y
Other Collaborators:

Participant Type: Co-Investigator
Participant: Andrey Starikovskiy
Person Months Worked: 4.00 **Funding Support:**
Project Contribution:

RPPR Final Report
as of 18-Oct-2018

International Collaboration:
International Travel:
National Academy Member: N
Other Collaborators:

CONFERENCE PAPERS:

Publication Type: Conference Paper or Presentation **Publication Status:** 1-Published
Conference Name: AIAA SciTech 2016
Date Received: 02-Sep-2016 Conference Date: 04-Jan-2016 Date Published: 04-Jan-2016
Conference Location: San Diego, CA
Paper Title: Experimental Investigation of Dynamic Stall in a Wide Range of Mach Numbers by Plasma Actuators with Combined Energy/Momentum Action
Authors: Andrey Starikovskiy, Richard Miles
Acknowledged Federal Support: **Y**

Publication Type: Conference Paper or Presentation **Publication Status:** 1-Published
Conference Name: AIAA Aviation 2016
Date Received: 02-Sep-2016 Conference Date: 13-Jun-2016 Date Published: 13-Jun-2016
Conference Location: Washington, DC
Paper Title: Experimental Investigation of Dynamic Stall in a Wide Range of Mach Numbers by Plasma Actuators with Combined Energy/Momentum Action
Authors: Andrey Starikovskiy, Richard Miles
Acknowledged Federal Support: **Y**

Publication Type: Conference Paper or Presentation **Publication Status:** 1-Published
Conference Name: AIAA Aviation 2016
Date Received: 02-Sep-2016 Conference Date: 13-Jun-2016 Date Published: 13-Jun-2016
Conference Location: Washington, DC
Paper Title: Experimental Investigation of Dynamic Stall in a Wide Range of Mach Numbers by Plasma Actuators with Combined Energy/Momentum Action
Authors: Andrey Starikovskiy, Richard Miles
Acknowledged Federal Support: **Y**

Publication Type: Conference Paper or Presentation **Publication Status:** 1-Published
Conference Name: AIAA Aviation 2017
Date Received: 26-Jun-2017 Conference Date: 05-Jun-2017 Date Published: 05-Jun-2017
Conference Location: Denver, Colorado
Paper Title: Stall Control at High Angle of Attack by NS pulsed Actuator in Burst Mode
Authors: Andrey Starikovskiy, Kristofer Meehan, Julian Williams, Arthur Dogariu, Richard B. Miles
Acknowledged Federal Support: **Y**

Publication Type: Conference Paper or Presentation **Publication Status:** 1-Published
Conference Name: AIAA Aviation 2017
Date Received: 26-Jun-2017 Conference Date: 05-Jun-2017 Date Published: 05-Jun-2017
Conference Location: Denver, Colorado
Paper Title: Nanosecond Dielectric Barrier Discharge Development and Thrust Generation in 4-Electrode Geometry
Authors: Andrey Starikovskiy, Kristofer Meehan, Julian Williams, Richard B. Miles
Acknowledged Federal Support: **Y**

RPPR Final Report
as of 18-Oct-2018

Project Summary - Grant # W911NF-15-1-0236
(Reporting Period: August 1, 2015 - July 31, 2018)

Control of Static and Dynamic Stall in a Wide Range of Mach Numbers by Plasma Actuators with Combined Energy/Momentum Action

PI Prof. Richard Miles
Department of Mechanical and Aerospace Engineering
Princeton University
D-412 Engineering Quadrangle, Olden Street
Princeton, NJ 08544-2020
UNITED STATES

Objective

The proposed research effort has two major thrusts – research on new nanosecond pulse driven surface plasma devices for enhanced control authority in high speed air, and research on the use of these surface mounted plasma devices for the suppression of dynamic stall on helicopter blades. The two components are complimentary and will be undertaken simultaneously as a unified research effort. The goal is to establish a new capability that provides robust helicopter blade control over a wide range of frequencies with systems that are low weight and flush mounted, so very little flow perturbation occurs when they are not in operation.

Approach

The research will concentrate on the development and characterization of the surface plasma devices and static testing in the wind tunnel for different type of actuators during the first year. During the second year initial static and dynamic pitching testing will be initiated in the wind tunnel, and that work will continue into year three with analysis of the efficiency and effectiveness of the surface plasma devices. The program addresses four basic plasma device configurations:

Single electrode Surface Dielectric Barrier Discharge (SDBD) device for rapid heat addition,

Multi electrode Surface Dielectric Barrier Discharge (MeSDBD1) device for microsecond synchronized local shock formation and shock coalescence

Close-spaced Multi electrode Surface Dielectric Barrier Discharge (MeSDBD2) device for nanosecond synchronized operation to transfer charge and suppress backward breakdown

Semiconducting Surface Dielectric Barrier Discharge (SSDBD) device for suppression of backward breakdown.

Relevance to Army

High speed helicopters must accommodate significant changes in the rotor lift performance as a function of rotor angle. The advancing blade can achieve transonic conditions while the retreating blade experiences relatively low speed. The high Mach number of the advancing blade requires an angle of attack below 5 degrees for maximum lift, whereas the retreating blade requires high an angle of attack in excess of 10 degrees. Under high speed and high load conditions, stall occurs during the retreating cycle and destabilizes the aircraft. Thus operation requires that the angle of attack of the blades be changed during the cycle and optimized with flight speed. The focus of this research is to determine to what degree plasma actuators can be used to optimize high speed flight performance, particularly focusing on suppressing the dynamic stall by retreating blade separation control.

Accomplishments for Reporting Period

- Development of the blade pitching system and the real-time data acquisition system for dynamic stall control experiments;
- FLEET technique adaptation for dynamic flow field measurements;
- New configuration multi-electrode NS-SDBD was tested and the flow acceleration in synchronized nanosecond discharge has been demonstrated;
- NS-SDBD over multi-diode asymmetric surface was developed using high-current SiC diodes;
- Demonstration of dynamic stall control by NS-DBD plasma actuators for normal and reverse flow configuration. Lift force increase up to 40% is shown for both cases for maximal angle of attack up to 32^0 for flow speed 20-70 m/s;
- The lift force increase up to 20% in a hover mode is demonstrated for a fixed engine power.

Collaborations and Technology Transfer

Multi-diode asymmetric surface development is made in close collaboration with United Silicon Carbide, Inc. USCi is responsible for customized SiC Schottky diodes fabrication and micro-assembly.

Resulting Journal Publications during Reporting Period

1. Kiyoshi Kinefuchi, Andrey Starikovskiy, and Richard B. Miles. *Control of Shock-Wave/Boundary-Layer Interaction Using Nanosecond-Pulsed Plasma Actuators.* Journal of Propulsion and Power, Vol. 34, No. 4, July–August 2018.

2. Nikolay Aleksandrov, Andrey Starikovskiy. *Ozone formation and energy transfer mechanisms in nonequilibrium plasma of ns-SDBD.* Plasma Sources Science and Technology. 2018. Submitted.

3. Andrey Starikovskiy, Nikita Persikov, Kristofer Meehan, Richard B. Miles. *Static and Dynamic Stall Control by NS SDBD Actuators.* Plasma Sources Science and Technology. 2018. Submitted.

4. Andrey Starikovskiy, Kristofer Meehan, and Richard B. Miles. *Dynamic Stall Control by NS SDBD Actuator*, 2018 AIAA Aerospace Sciences Meeting, AIAA SciTech Forum, (AIAA 2018-0681)

5. Andrey Starikovskiy, Nikita Persikov, and Richard B. Miles. *Helicopter Lift Force Increase in Hover Mode by NS-SDBD Plasma Actuators*, 2018 AIAA Aerospace Sciences Meeting, AIAA SciTech Forum, (AIAA 2018-0936)

6. Andrey Starikovskiy, Kristofer Meehan, Arthur Dogariu, Richard B. Miles. *Dynamic Stall Control at High Angle of Attack by NS pulsed Actuator in Burst Mode* (AIAA 2017-3342) 48th AIAA Plasmadynamics and Lasers Conference, 2017, 10.2514/6.2017-3342

7. Andrey Starikovskiy, Kristofer Meehan, Julian Williams, Richard B. Miles. *NS Dielectric Barrier Discharge Development and Thrust Generation in 4-Electrode Geometry* (AIAA 2017-3344) 48th AIAA Plasmadynamics and Lasers Conference, 2017, 10.2514/6.2017-3344

8. Andrey Starikovskiy, Richard B. Miles. *Dielectric Barrier Discharge Control and Thrust Enhancement by Diode Surface* (AIAA 2017-4159) 48th AIAA Plasmadynamics and Lasers Conference, 2017, 10.2514/6.2017-4159

9. Andrey Starikovskiy, Kristofer Meehan, Julian Williams, Richard B. Miles. *Static and Dynamic Stall Control at High Angle of Attack by NS pulsed Actuator in Burst Mode* (AIAA 2017-1342) 55th AIAA Aerospace Sciences Meeting, 2017, 10.2514/6.2017-1342

10. Andrey Starikovskiy, Richard B. Miles. *Experimental Investigation of Dynamic Stall Control in a Wide Range of Mach Numbers by Plasma Actuators* (AIAA 2016-4017) 47th AIAA Plasmadynamics and Lasers Conference, 2016, 10.2514/6.2016-4017

11. Andrey Starikovskiy, Richard B. Miles. *Plasma Actuators with Combined Energy/Momentum Action* (AIAA 2016-4017) 54th AIAA Aerospace Sciences Meeting, 2016, 10.2514/6.2016-0452

Graduate Students Involved During Reporting Period

Kristofer Meehan (grad student)

Awards, Honors and Appointments

None

Contents

NS-SDBD dynamics, ozone formation and energy transfer mechanisms

Currently, the problem of flow active control by low-temperature plasma is considered to be one of the most significant topics in aerodynamics [1, 2]. One of the main practical advantages of plasma-assisted flow control is its zero reaction time. This, in principle, provides control over a wide range of frequencies as well as covering a wide range of processes beginning from stationary to separated and turbulent flows. Two other important advantages of plasma systems are their low weights and sizes. If combined with relatively low energy consumption, their features allow the possibility of principally developing new systems of flight control at high velocities [3].

Promising applications of plasma systems to control flow involve the management of laminar-to-turbulent transition in the boundary layer, the management of flow detachment or attachment to the surface, and the resulting management of the lift and drag force of an airfoil. This also provides management of noise and vibrations, and control of shock wave patterns as well as shock wave interactions with the boundary layer.

Flow control opportunities by plasma can be divided into two groups: 1) main flow control, including shock wave configuration in supersonic and hypersonic regimes; 2) boundary layer control.

Main flow control includes shock wave pattern control, aerodynamic breaking, drag reduction, heat mitigation, flow vectorization, flow acceleration and flow deceleration, as well as MHD power extraction and breaking.

Boundary layer control could be subdivided into laminar-turbulent transition control, boundary layer separation control, lift and drag force control, acoustic noise control, and mixing enhancement. Nonequilibrium plasma may also be very efficient in ignition and flame stabilization control, and engine performance enhancement [4, 5].

Three different physical mechanisms control the efficiency of plasma aerodynamics. They are: 1) gas heating; 2) electrostatic momentum transfer to the gas; and 3) magneto-hydrodynamic effects, including MHD flow acceleration and on-board electricity generation using gas flow kinetic energy. Sometimes it is necessary to take into account gas dissociation and the change in the average molecular weight of the gas, but strong dissociation or ionization of the gas requires huge amounts of energy. That is why for aerospace applications we generally try to keep gas excitation at a minimal level. This decreases the role of the variation of gas composition in the discharge.

On the whole, plasma governs flow through two main mechanisms - either by momentum or by energy transfer.

Discharge energy transfer to the flow is a rather complicated multistep process [6]. The electrons gain energy from the electric field because they possess small masses and long mean free paths. The slow rate of energy exchange of electrons with neutral gas results in a significant deviation of the mean electron energy from the energy of translational degrees of freedom of molecules. Depending on the value of the applied electric field, the mean electron energy in the discharge can reach several electron-volts. These conditions provide active excitation of the internal degrees of freedom of molecules, as well as their dissociation and ionization by electron impact. At the same time, the energy flux into translational and fast-thermalizing rotational degrees of freedom is relatively low.

Consequently, the energy release at VT-relaxation, the recombination of neutral and charged components and the quenching of electronically excited molecules is the main mechanism of increasing gas temperature in non- equilibrium plasma. VT relaxation and atom recombination are rather slow and can last tens of microseconds or longer even at atmospheric pressure, which is comparable to typical gas dynamic times within a scale of several millimeters. Energy release during excitation of electronically excited states, molecular dissociation and molecular ionization by electron impact are much faster processes. For instance, a molecule being excited by electron impact to a repulsive state dissociates to form products with a high translational energy. The rate of thermalization of such "hot" atoms and radicals usually reaches units of nanoseconds. The quenching of electronically excited molecules and electron-ion and ion-ion recombination proceed on the same time scale. A heating mechanism like this can become a governing process and heat gas quickly in the discharge region under high values of reduced electric field - E/n (close to or higher than the breakdown threshold) [7-9].

Presently, most researchers applying plasma actuators for flow control propose to use this device to accelerate the flow in the boundary layer near the airfoil surface in the region of flow separation. They consider induced velocity to be one of the main features developed by the actuator in the discharge zone. The gas flow velocity can be changed during the interaction between the electric field and the uncompensated spatial plasma charge. Two different mechanisms, stationary and non-stationary, lead to such an interaction. In a stationary case the electrical field is limited by breakdown threshold. In the paper [10], the estimations based on the volumetric force equation $F = e \times n \times E$ and the Poisson equation lead to simple relation for induced velocity

$$v_g = E^*(\varepsilon_i/\rho)^{1/2}$$

where ρ is the gas density, E is an applied electric field and ε_i is the ion mobility. This equation describes the gas flow in stationary discharges using the condition that E cannot exceed the breakdown threshold. For free space this equation predicts the maximum induced velocity up to 80 m/s, but close to the surface, due to the effects of viscosity, this maximum cannot be achieved [10]. In point of fact, the estimation proposed in [10] assumes the permanent presence of a spatial charge in the plasma region. In a weak electrical field this charge cannot be generated by gas ionization or emission from the electrodes [6]. Thus the estimation [10] is an upper limit of the induced velocity in the presence of an external source of uncompensated charge in the plasma region.

As a rule, the presence of significant uncompensated spatial charges in gas is associated with the presence of strong electric field gradients and ionization waves [11]. A streamer discharge is an example of such a case. The strong electric field of the streamer's head influences the uncompensated charge on the ionization wave front at the streamer's head. This results in significant acceleration of the gas in the region of the strong field. This process lasts only fractions of a nanosecond. The calculations presented in [12] have shown that the velocity of gas in a single streamer's channel may reach units of centimeters per second. This mechanism is implemented in pulsed non-stationary discharges without bias.

AC discharges and pulsed discharges with significant bias are situated in between these two limiting cases. Presently, the possibility of gas acceleration reaching a velocity up to nearly 10 m/s has been shown with the help of positive corona [13-15].

It should be noted that the nature of gas acceleration is the same in all cases. The interaction between the uncompensated plasma charge and the electric field, together with the effective momentum transfer from charged to neutral gas components, generate flux acceleration as a whole.

In 2005, Opaits et al. [12] proposed using pulsed nanosecond periodic discharges for plasma actuators. The E/n value for this type of discharge can exceed the breakdown threshold by several magnitudes. The high value of the reduced electric field seems to be an evident advantage of such a discharge. Relatively low energy consumption, the possibility of using such discharges within a wide range of pressures, flow velocities, and gas compositions, including high humidity, also contribute to the advantages of the approach proposed. The first experiments [12] have shown that it is possible to firmly control the boundary layer separation using this nanosecond pulsed discharge at velocities of up to 75 m/s and at an energy consumption lower than 1 W/cm of wingspan.

The nanosecond pulsed discharges have demonstrated an extremely high efficiency for aerodynamic plasma actuators over a very wide range of velocities (M = 0.03 - 0.75) and Reynolds number (Re = 10^4 - 2×10^6). For further technological development it is extremely important to understand the physics of the nanosecond plasma actuator and differences between different types of SDBD in terms of their efficiencies [16-20].

In [16] the mechanism of pulsed nanosecond high-voltage discharge influence on boundary layer separation was experimentally demonstrated. It was shown that fast nonequilibrium plasma thermalization (on the time scale of hundreds of nanoseconds) produces a hot, over-pressurized gas layer in the discharge zone, followed by a strong shock wave formation. The interaction of the density gradient and the velocity gradient in the shear layer separating free stream and separation bubbles causes strong flow perturbations and provokes flow re-attachment through the formation of large scale vortices in the shear layer [16]. Later, experimental results [21] proved that nanosecond SDBD plasma performs as an active excitation at pre-stall angles of attack and provides high amplitude perturbations that manipulate flow instabilities and generate coherent spanwise vortices at post-stall angles. These coherent structures entrain freestream momentum thereby reattaching the normally separated flow to the suction surface of the airfoil.

This means that we need a high rate of energy release from the electric field to translational degrees of freedom of gas. Fast energy transfer (in a time frame that is shorter than gas-dynamic time in the plasma layer) means the efficient generation of the density gradient and efficient excitation of perturbations in the flow [22]. That is why the dynamics of energy transfer in nonequilibrium plasma is the most critical issue for pulsed NS-SDBD actuators.

As mentioned previously, the main mechanism of pulsed nanosecond SDBD effect on the flow is extremely fast heating of gas. Energy release in the gas is sometimes considered to be $Q=U\times I\times\tau$, whereas gas heating is defined by $\Delta T = Q/C_p$. Such an estimate includes some strong assumptions. The electric field energy is supposed to be completely absorbed by the gas. This is not always true in the case of strong electric fields, since part of the energy is lost to radiation processes. In the case of high-current discharges at small electric fields, some energy is lost in the near-electrode regions. In this case, part of the energy goes to heat the electrodes. Thus, the current multiplied by voltage in the discharge gap gives only the upper estimate for energy release. Estimations of temperature changes in the discharge are still stronger suppositions. The equation $\Delta T = Q/C_p$ is completely valid for the thermal equilibrium state when internal degrees of freedom of the gas are in equilibrium with the translational degrees of freedom. That is not the case for strongly nonequilibrium plasma of gas discharge. On the other hand, using specific heat under constant pressure, C_p, presumes that energy release occurs at time scale noticeably greater than gas-dynamic one. Then, it is quite reasonable to use the supposition $P = const$. Therefore, when analyzing the thermal mechanism of the plasma actuator impact on the flow, it is necessary

to take into account not only radiation energy loss, wall heating, etc., but also the rate of energy relaxation in comparison to the typical times of plasma layer expansion.

Fast gas heating after the discharge energy deposition at high *E/n* plays a key role in flow control by SDBD plasmas. The mechanisms of fast gas heating under such conditions have been studied and discussed in [7-9,23]. It was shown that at high *E/n* a large amount of deposited energy is spent on ionization and that the efficiency of gas heating depends on the mechanisms and products of electron-ion and ion-ion recombination. In particular, possible products of the recombination of charged particles in air plasmas are O atoms. The formation of O atoms is followed by the production of ozone which is an indicator of O_2 dissociation. Ozone is also a harmful species that can restrict SDBD applications. Thus, branching ratios in recombination of charged particles influence not only the amount of energy transferred to heat, but the production of ozone as well.

This paper reviews experimental studies of a nanosecond SDBD in air, including the discharge development for various pressures, measurements of energy distribution, electric fields and ozone production in SDBD plasmas. The mechanisms of fast gas heating in nanosecond SDBD discharges and their relationship to ozone production are also discussed.

SDBD development. Plasma layer dynamics at different pressures

A low-pressure chamber was built for low-pressure SDBD development experiments. The chamber allows for excellent optical access to the object through multiple viewports. The removable top provides precise positioning and allows for focusing of the optical systems. The system is evacuated prior to the experiments to a pressure of $P \sim 10^{-2}$Torr. A low initial pressure allows one to check the water vapor influence on the discharge development and propagation.

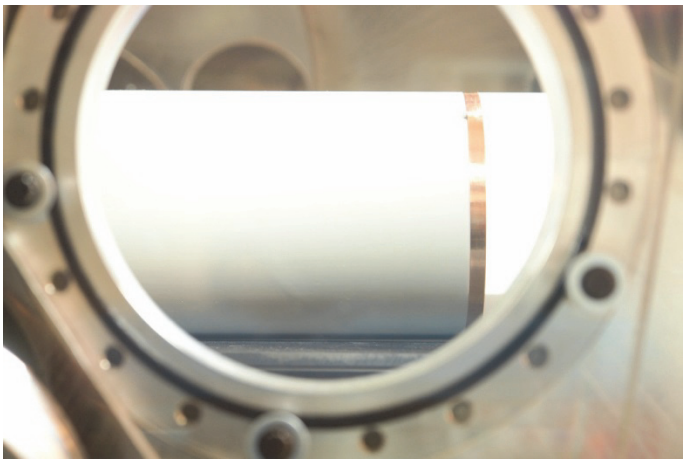

Figure 1. Model inside of the vacuum chamber on the dielectric table. Side view. Location of the exposed electrode is the same for all images.

The interior chamber dimensions are 50×50×80 cm^3. Thus even for low-pressure experiments we can ensure the absence of a short-circuit between the high-voltage electrodes and the walls of the chamber. A typical velocity of streamer propagation is close to 1-2 mm/ns in air and we expect the discharge propagation distance to be up to 50-100 mm in all directions from the high-voltage electrode during a 50-ns pulse. A closed stainless-steel chamber minimized the EMI from the discharge and simplified the measurements of the discharge parameters.

The ns-SDBD was initiated on a cylindrical model. The dielectric cylinder has an external diameter of 120 mm. The grounded electrode was placed on the side surface of the cylinder and covered with 0.45 mm-thick PVC film. The model was placed in the vacuum chamber. A dielectric plate was used to separate the model from the walls and floor of the stainless-steel chamber. Figure 1 shows the model location behind the vacuum window in the chamber.

As a result of these experiments it is possible to restore the structure and dynamics of the zone of energy release. This data will be used to construct the analytical approximation of the discharge energy distribution near the surface.

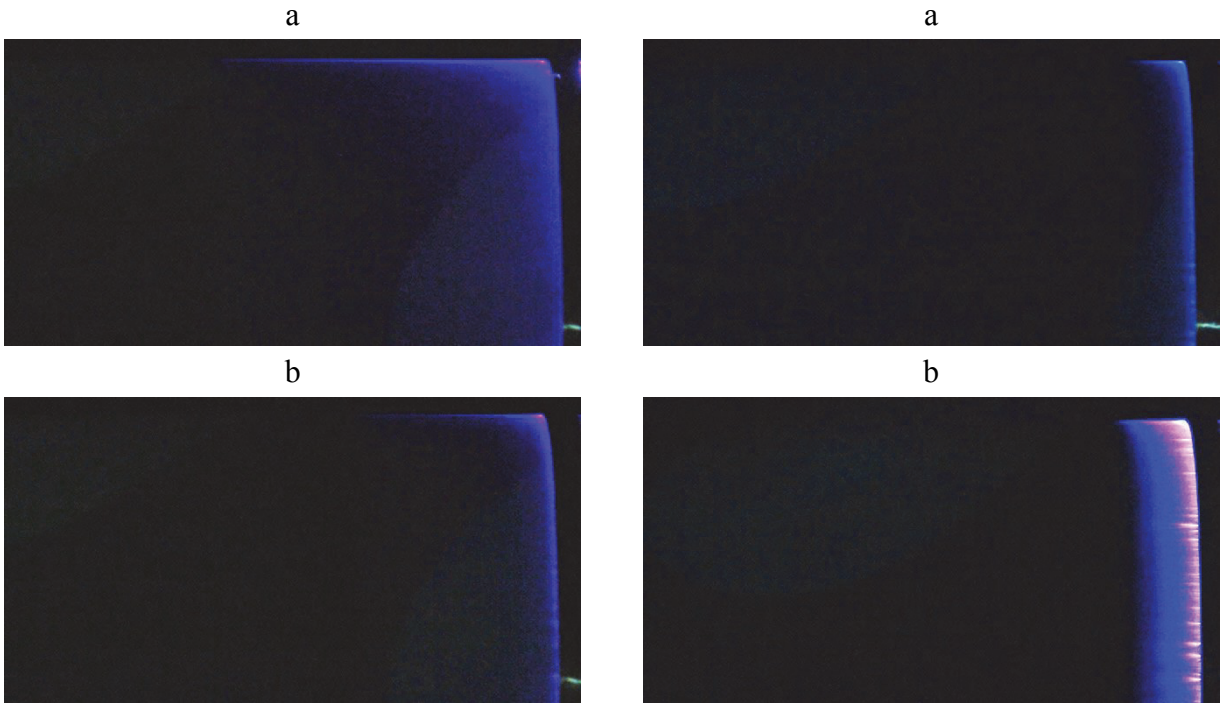

Figure 2. Discharge in air. Left column: U = 16 kV; f = 10 Hz; a) P = 0.1 atm, b) P = 0.5 atm. Right column: P = 1 atm. a) U = 16 kV; f = 10 Hz; b) U = 25 kV; f = 50 Hz.

Figure 2 shows the discharge development at different pulse voltages. It is clear that for low-frequency operation the discharge dynamics does not depend on the frequency. The length of streamer propagation and thickness of the plasma layer are proportional to the pulse voltage.

Plasma layer geometry and uniformity of discharge

Dynamics of the pulsed discharge development was investigated for pressures 12, 20, 40, 80, 160, 320, 640 Torr and 1 atm. Four different types of nanosecond pulse generators were used to initiate the surface DBD. The generators use a Fast Ionization Device (FID) as a switch. The generator's pulse parameters (Figure 3) were the following, amplitude in the coaxial 50-Ohm cable was up to 12 kV, rise time was 3 ns, duration on half-height was 7 ns (Type 1), amplitude up to 25kV, rise time 1.3 ns, duration 12 ns (Type 2), amplitude up to 50 kV, rise time 7 ns, duration 25 ns (Type 3), and amplitude up to 50 kV, rise time 3 ns, duration 45 ns (Type 4). The high voltage pulses were transmitted from the pulse generator to the high-voltage electrode by means of a 50-Ohm coaxial RC-50-11-11 cable (Figure 3). For this series of experiments the pulsed voltage was U = 10 and 20 kV, pulse duration ~20 ns (rise time ~8 ns), discharge frequency 100 and 1000 Hz. ICCD camera gate was 1 ns, time shift between images 1 ns (Type 3).

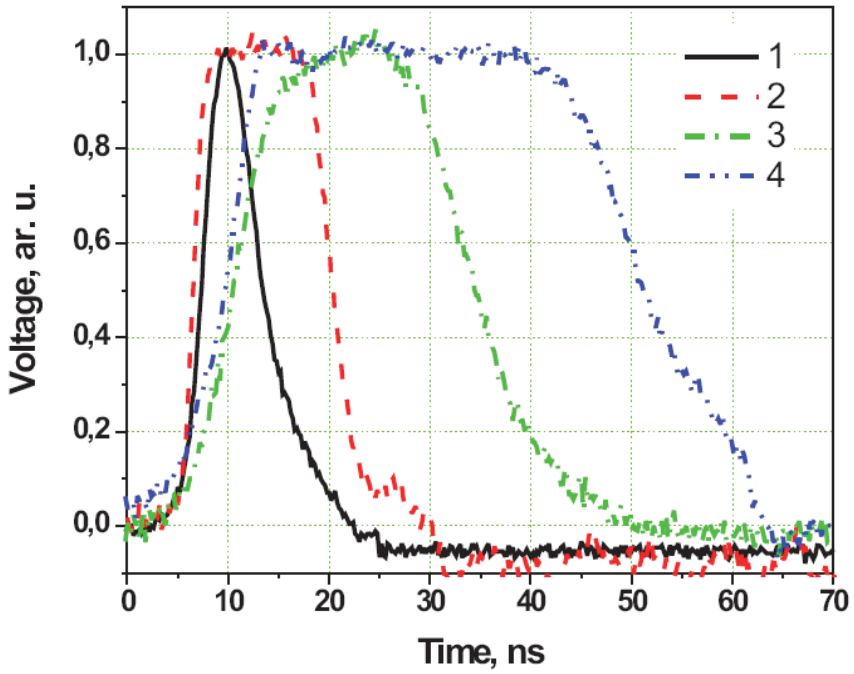

Figure 3. Pulse voltage shape for different types of generators. 1) Type 1, 2) Type 2, 3) Type 3, 4) Type 4.

One sequence of images for P = 20 Torr, U = 10 kV, f = 1000 Hz was demonstrated (Figure 4). The others are available in electronic form. Standard asymmetrical SDBD geometry, dielectric – 6-layers PVC film with a total thickness of 0.4 mm (Figure 4).

The same measurements were made for a wide range of pressures for pulse voltages +10, +5, -5 and -10 kV in the cable. This voltage doubles on the high-voltage electrode of the actuator because of electric pulse reflection in the coaxial line. The plasma layer thickness h, maximal propagation length L, typical velocity of the ionization front propagation V, and an average front velocity during first the 10 ns of the discharge development were extracted from the sequences of images. Below there is a summary of the measurements made.

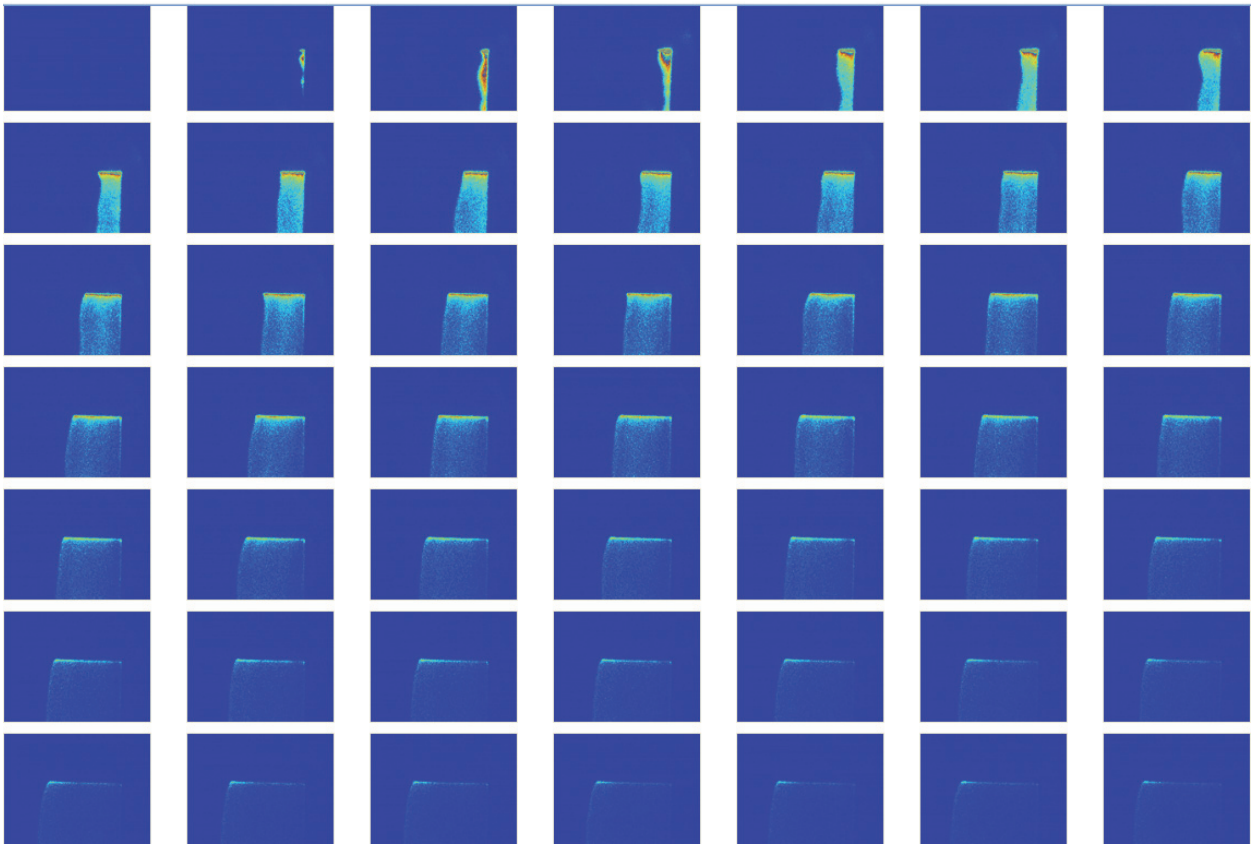

Figure 4. SDBD dynamics for P = 20 Torr, U = +10 kV, f = 1000 Hz.

Figure 5 shows the dependence of the plasma layer length on the air pressure. It is clear that the plasma layer length does not depend on the discharge frequency for f = 100, 1000 Hz. The length depends on the pulse polarity (for a negative polarity the length is two times shorter than for a positive polarity). A pulse voltage decrease from 10 to 5 kV leads to a plasma layer length reduction of 1.5-2 times – almost proportional to the pulse voltage.

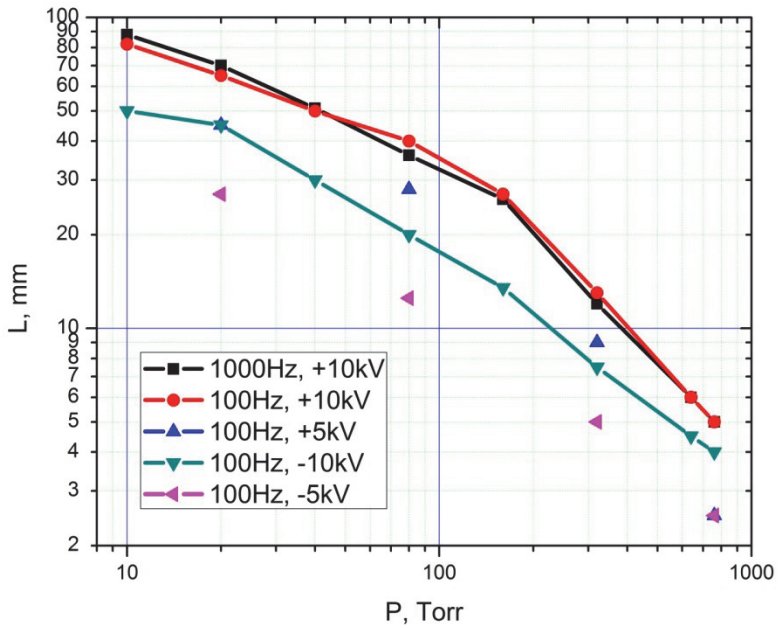

Figure 5. Dependence of plasma layer length on the air pressure.

For a pressure range of 760-160 Torr, the plasma layer length is inversely proportional to the pressure. At $P < 160$ Torr the plasma layer length is proportional to $L \sim P^{(-1/2)}$ (Figure 5). The plasma layer length decrease for negative polarity of the pulse is due to a smaller velocity of the anode-directed discharge propagation

Figure 6 demonstrates the plasma layer thickness for different pulse polarities, voltages and air pressures. For all regimes at f = 100 Hz the plasma layer thickness is close to $h \sim P^{(-1/2)}$ (Figure 6). For a higher frequency (f = 1000 Hz) the dependence on the pressure is weaker. The same dependence on the voltage applied is shown. The plasma layer thickness is almost proportional to the pulse voltage, both for positive and negative pulse polarities (Figure 6).

An average ionization front propagation velocity is shown in Figure 7. The discharge for negative polarity has two times lower propagation velocity. Pulse voltage decrease leads to proportional ionization front velocity decrease. Dependence on the pressure in all the ranges investigated is close to $V \sim P^{(-1/2)}$ (Figure 7). Dependence on the discharge frequency for f = 100 and 1000 Hz is almost nonexistent.

Thus, the dynamics of the pulsed discharge development was investigated for pressures 12, 20, 40, 80, 160, 320, 640 Torr and 1 atm. For these experiments pulsed voltage was U = 10 and 20 kV, pulse duration ~20 ns (rise time ~5 ns), discharge frequency 100 and 1000 Hz.

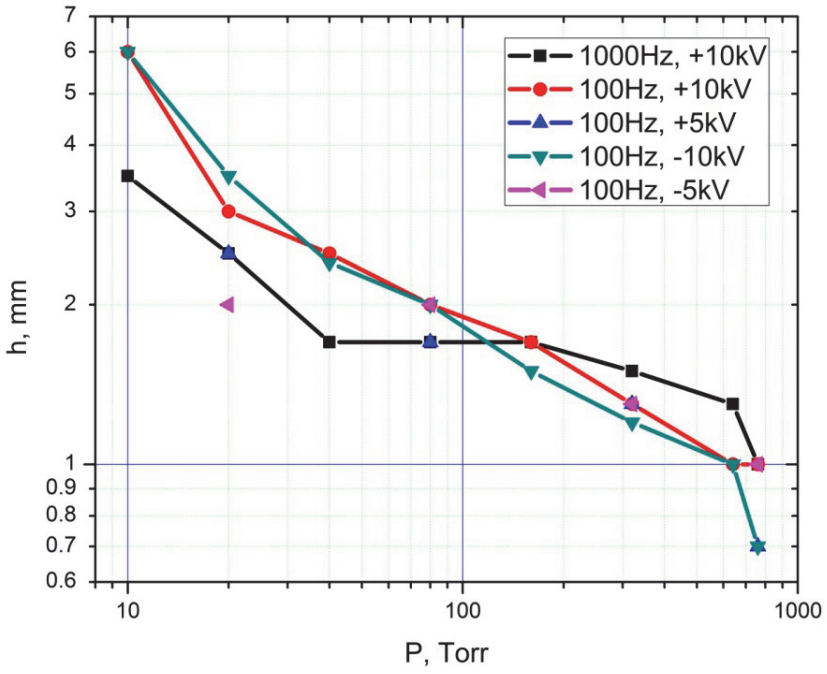

Figure 6. Dependence of plasma layer thickness on the air pressure.

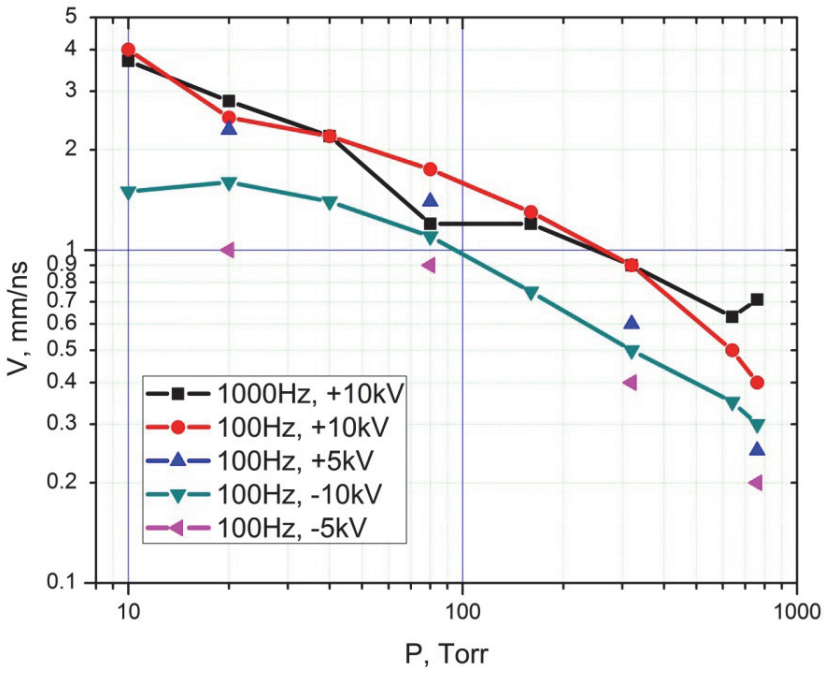

Figure 7. Dependence of ionization front propagation velocity on the air pressure.

Discharge energy distribution and electric fields

The experimental setup for plasma layer dynamic measurements consisted of a cubic vacuum chamber with a side size 220 mm (Figure 8). The system was evacuated by a 2NVR-5DM rotary vacuum pump down to pressure of 10^{-1} Torr. The gas supply system allowed one to fill the chamber with different gas mixtures up to a maximum pressure of two atmospheres. N_2:O_2 = 80:20 synthetic air of spectral purity was used in these experiments. The usual asymmetric plasma actuator geometry was used to initiate surface nanosecond barrier discharge.

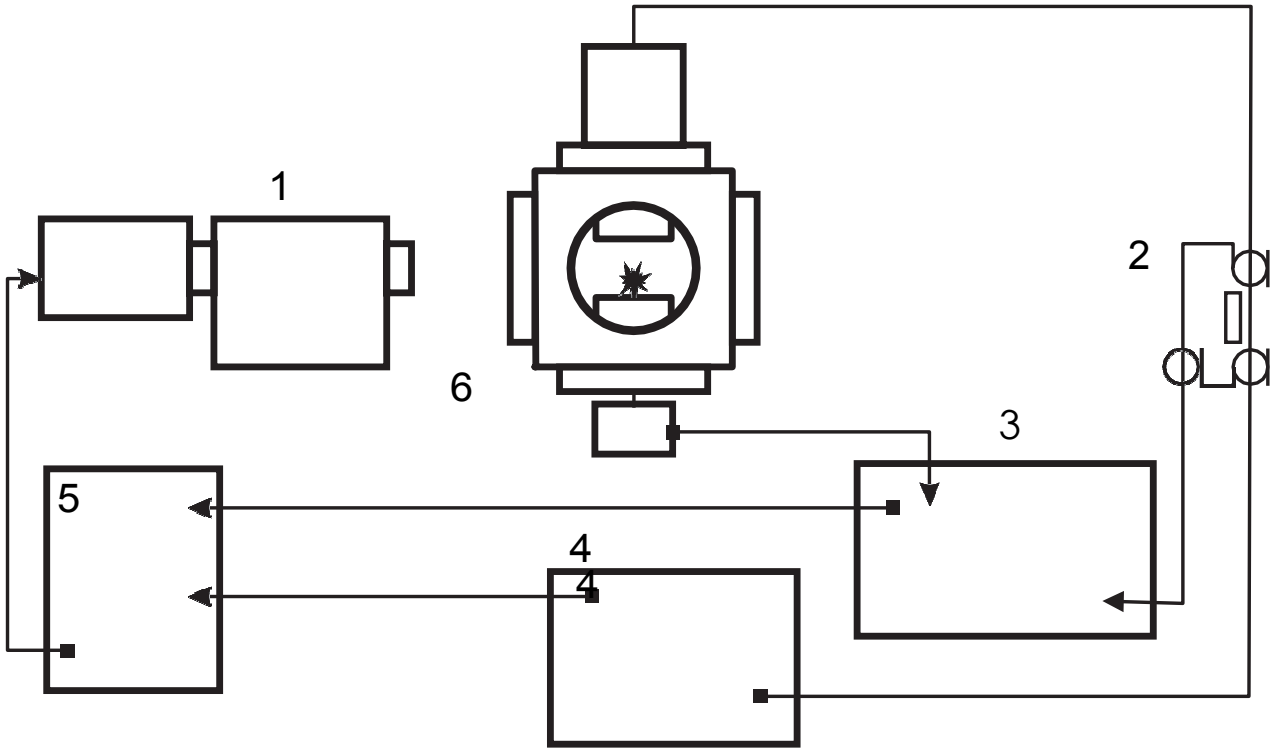

Figure 8. Scheme of the experimental setup. 1 — PicoStar HR-12 LaVision ICCD system; 2 — back current shunt, R=0.15 Ohm; 3 —Tektronix TDS3054B digital phosphor oscilloscope; 4 — FID-based Generator of Type 1 (amplitude 12 kV, rise time 3 ns, duration on half-height 7 ns); 5 —control computer for ICCD camera system with synchronization from the high-voltage pulse generator; 6 — direct current shunt with R = 2.0 Ohm.

The high-voltage electrode and low-voltage electrodes were made of copper foil 0.05 mm thick, 5 mm wide, and 85 mm long. The low-voltage electrode was covered by a fluorocarbon film with a thickness of 0.3 mm. The scheme of the discharge gap is presented in Figure 9.

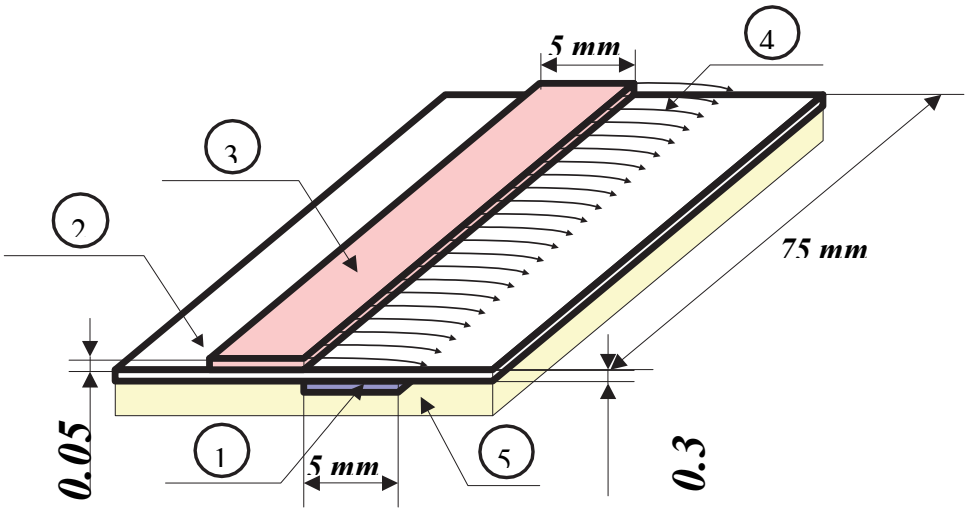

Figure 9. Scheme of discharge gap. 1 — high-voltage exposed electrode; 2 — dielectric layer; 3 — low-voltage electrode, 4 — zone of discharge propagation, 5 — dielectric base.

Electric field measurements

The reduced electric field was measured using the emission profiles of the first negative system of the nitrogen ion and the second positive system of the nitrogen molecule. The given spectroscopic technique to estimate *E/n* values can be applied when the upper emitting electronic levels are excited by direct electron impact from the ground state. In our case we have a short (7 ns on the half-width) high-voltage pulse and thus the concentration of metastable states cannot reach the level when cascade processes would significantly contribute to populating the upper levels. High values of *E/n* can also lead to direct population by electron impact. This technique has been successfully applied to measure the fields in streamer and barrier discharges (see, for example, [16]). The emission profiles at 337.1 nm and 391.7 nm were obtained with nanosecond temporal resolution. Typical oscillograms are shown in Figure 10 for anode-directed discharge. Radiation was measured by a photomultiplier FEU-100 with a multi-alkaline photocathode (spectral response 170-650 nm). The radiation was selected using the monochromator MDR-41 (grating 3000 lines/mm, f = 300 nm, dispersion 0.95 nm/mm) which was placed in front of the plasma actuator. The widths of the front and back slits of the monochromator were 0.2 mm and 0.35 mm, respectively. The discharge was initiated by a high-voltage pulse with a duration at half height, 7 ns (Figure 10, Type 1). The measurements were performed with and without the diaphragm. The diaphragm allows one to measure the radiation flux coming only from the discharge central part. In the latter case the optical system catches emission from the region of the high-voltage electrode edge. The mean electric field measured without the diaphragm was higher in both the anode and cathode-directed discharges. From this, it can be concluded that the *E/n* value is almost uniform along the streamers' zone and is higher near the exposed electrode edge.

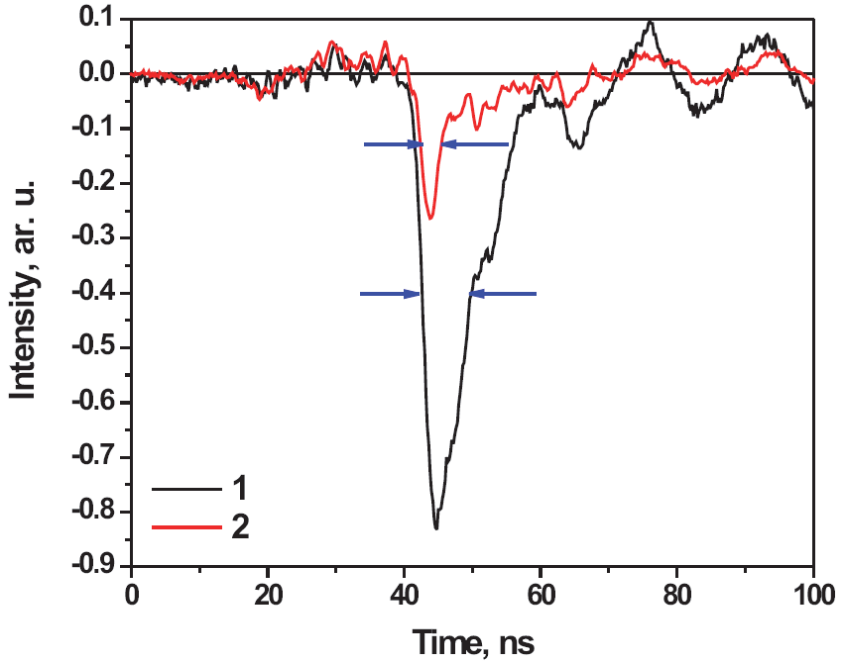

Figure 10. Typical oscillograms of N_2 second positive and N_2^+ first negative systems emission dynamics. 1 –337.1 nm, 2 – 391.7 nm.

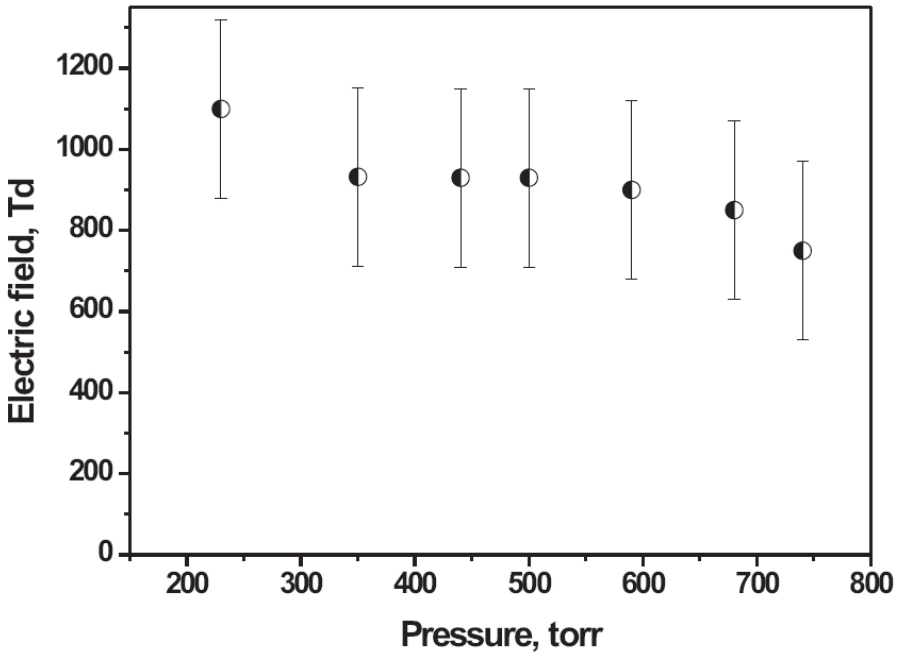

Figure 11. Reduced electric field value *E/n* in anode-directed discharge.

Figure 11 shows the mean electric field in the center of the discharge zone. Emission from the edges of the high and low voltage electrodes were blinded by the diaphragm. The electric field reaches a maximum at the lowest pressures (1150 Td at a pressure of 220 Torr) and decreases while the pressure increases (800 Td at atmospheric pressure). The ambiguity of the experimental data is mainly due to statistical pulse-to-pulse discharge variations and the fluctuation of radiation of the 1^- system of the nitrogen ion. The value of radiation of the 2^+ system of molecular nitrogen was quite stable. This fluctuation of radiation of the 1^- system is connected to a higher excitation threshold of this system. A greater sensitivity of the population rate constant of $N_2^+(B^2)$ state is connected to the discharge development.

Ozone generation and energy transfer

The measurement of ozone formation by an asymmetric plasma actuator and an analysis of possible ways to reduce the amount of ozone generated were analyzed. The discharge geometry was the same as in previous chapter.

A back-current shunt inserted into the break of the cable shield was used to control the parameters of the high voltage pulse. The direct current shunt was used to measure the electrodynamic characteristics. The low-voltage electrode tip was shunted to the ground through TVO resistors with a total resistance of 0.5 Ohm.

Energy input in the discharge was calculated as a difference of the energy stored in the incident and reflected pulses (Figure 12). Typically the value of energy input was in the range from 10 to 8 mJ per pulse and decreased slowly as the pressure increased (Figure 13).

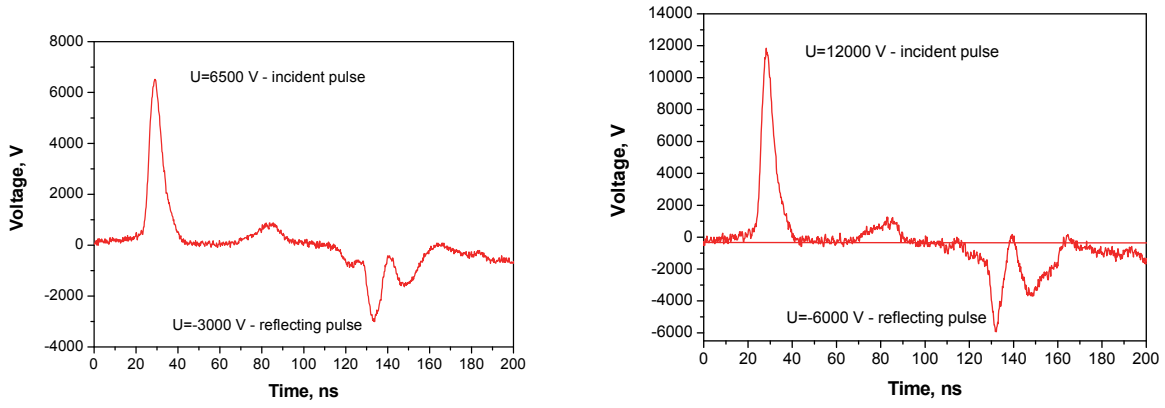

a b

Figure 12. High voltage pulse shape. a) U = 6.5 kV in the cable; U = 9.5 kV on the discharge gap. b) U = 12 kV in the cable; U = 18 kV on the discharge gap.

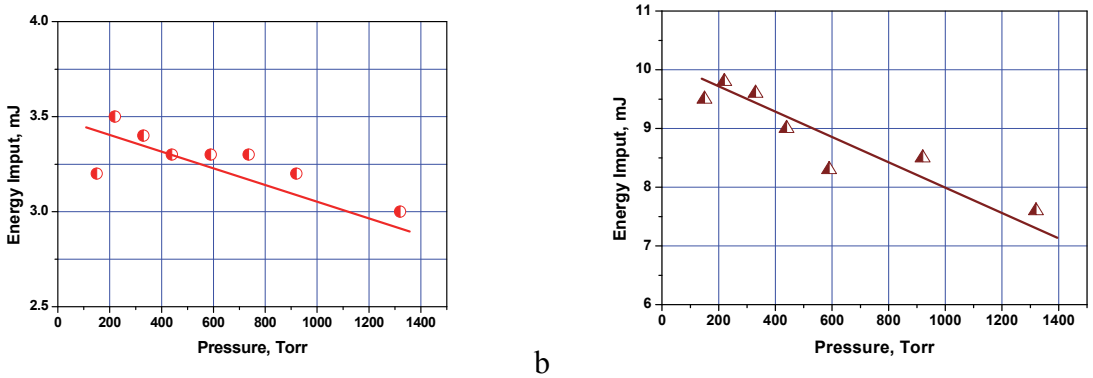

a b

Figure 13. High voltage discharge energy input.
a) U = 9.5 kV b) U = 12 kV on the discharge gap.

For ozone concentration measurements we used UV absorption spectroscopy. The ozone has strong absorption band (the Hartley band) with a maximum at 250 nm. A deuterium arc spectroscopic lamp - DDS-30 was used as a radiation source at this wavelength. The collimation system consists of two diaphragms and a quartz lens. This system allows us to measure the absorption near the surface with a spatial resolution of about 0.5 mm.

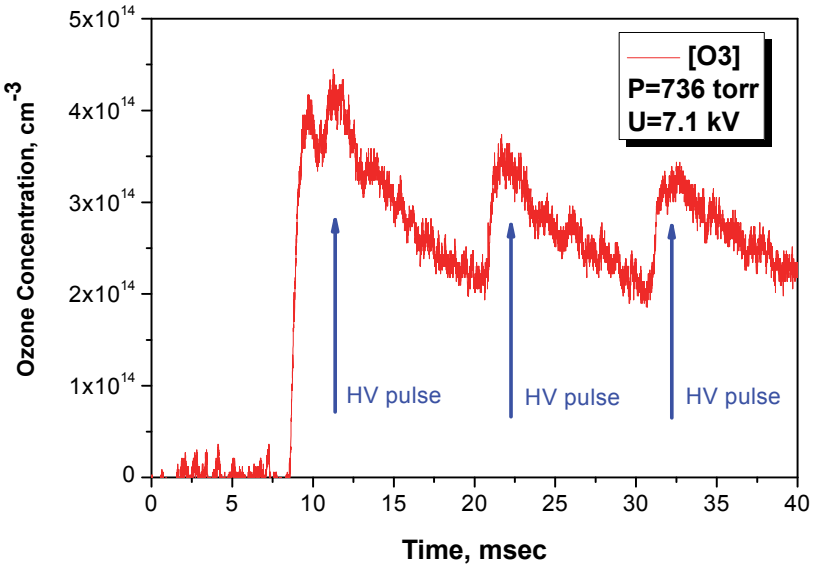

Figure 14. Ozone concentration in repetitive mode of pulsed discharge.
P = 736 Torr, U = 10.7 kV.

Typical results for measurements for ozone formation in the repetitive mode of the discharge are shown in Figure 14. The discharge frequency was 100 Hz. It can be clearly seen that the formation of the ozone in the discharge afterglow is a very fast process in contrast to diffusion.

Diffusion leads to the ozone concentration decrease between pulses (Figure 14). To avoid the complex kinetic analysis connected with ozone accumulation in the discharge region, we used the single – pulse regime of the generator for ozone production measurements. In this regime high-voltage pulses produce the discharge every time in the fresh air.

Measurements were performed for two pulse voltages – 9.5 kV and 18 kV. In Figure 15, the ozone concentration vs gas pressure after the pulse was presented. For the low-voltage regime (U = 9.5 kV), the ozone concentration is varied from 2×10^{14} cm^{-3} at P = 200 Torr to 2×10^{15} cm^{-3} at P = 1400 Torr. For the high-voltage case (U = 18 kV), ozone concentration is varied from 3×10^{14} cm^{-3} at P = 200 Torr to 4×10^{15} cm^{-3} at P = 1400 Torr. In both cases the concentration is rather small and so all secondary processes which may lead to ozone decomposition, such as reactions with atomic oxygen, nitric oxides, etc. can be neglected. In our case, almost all atomic oxygen produced in the discharge is converted into ozone in several microseconds. Thus, to analyze the efficiency of ozone formation we should estimate the efficiency of molecular oxygen dissociation in the discharge.

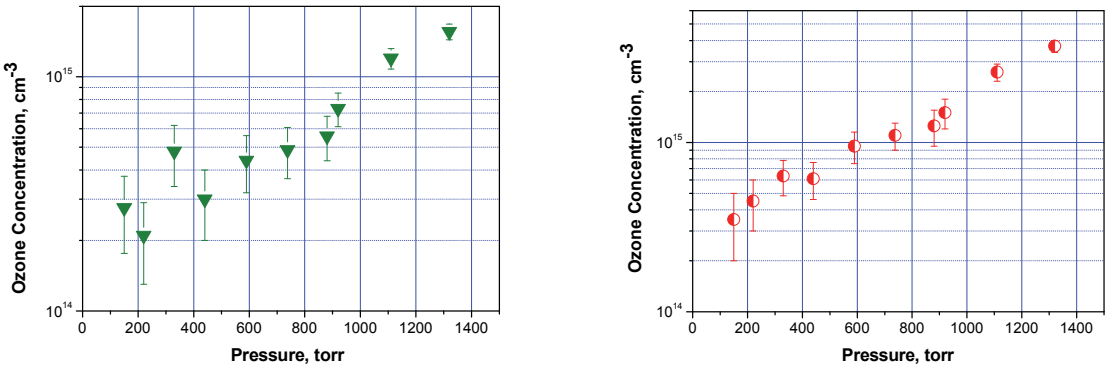

Figure 15. Ozone Concentration in Single Pulse Regime Pressure Range 0.2-1.8 atm, U= 9.5 (a) and 18 kV (b)

Numerical modeling of ozone generation

The most important issue from the point of view of practical applications is the ability to predict and minimize ozone production in plasma actuators. Numerical modeling of sliding surface dielectric barrier discharge is an extremely difficult task which involves complex physics. To describe this process, it is necessary to know the ionization rate constant in the given location at a particular moment in time as well as the transport properties of the electron's ensemble. The solution of the Boltzmann equation gives us an electron distribution function (EDF). Using the EDF we can obtain the ionization rate and calculate the electron's motion. The electric field in the case of the pulsed nanosecond barrier discharge may be extremely high in the region of the discharge development. This means that the so-called "local" EEDF approximation may not be

valid due to formation of run-away electrons. On the other hand, the modeling of SDBD using the Monte-Carlo approach to analyze the high-energy part of electrons is not solved yet [24]. Therefore, it is very difficult to take into account the non-local and non-stationary effects of the EEDF formation. These effects can arise from the final time and spatial scale of the EEDF relaxation. These effects can lead to the deviation of the calculated ionization rate value from the true value in the high gradient electric field region near the ionization wave front (see paper [8]).

Distribution of the discharge energy through different processes

To model the energy distribution through different processes we used the two-term approximation of the Boltzmann equation for an electron energy distribution function. We used the cross-section database published by Phelps [25].

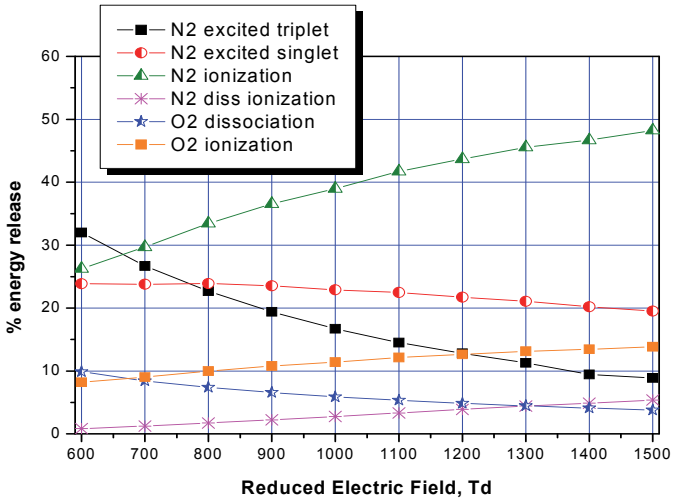

Figure 16. Distribution of the Discharge Energy through Different Processes in dependence on the *E/n*.

The results of the analysis are presented in Figure 16. One can see that the increase of the *E/n* value leads to the increase of the ionization rate in comparison to other processes. Thus, at high *E/n* values the main process in the discharge is the gas ionization. At moderate *E/n* values the main part of the discharge energy came into excitation of the electronic levels of the molecules. Direct dissociation by electron impact takes about 10% of the discharge energy in the range *E/n* = 500 – 2000 Td (Figure 16). For our geometry of the discharge cell, the reduced electric field is very high and reaches the value of ~1 kTd (Figure 11). Under such conditions the main part of the discharge energy is spent for excitation of electronic levels, dissociation and ionization of the gas.

Main processes which leads to ozone formation in the discharge

Excitation of electronic states of nitrogen

$$N_2(X^1\Sigma_g^+) + e \rightarrow N_2(A^3\Sigma_u^+) + e$$
$$N_2(X^1\Sigma_g^+) + e \rightarrow N_2(B^3\Pi_g) + e$$
$$N_2(X^1\Sigma_g^+) + e \rightarrow N_2(C^3\Pi_u) + e$$

$$N_2(A^3\Sigma_u^+) + O_2 \rightarrow N_2(X^1\Sigma_g^+) + O + O$$
$$N_2(B^3\Pi_g) + O_2 \rightarrow N_2(X^1\Sigma_g^+) + O + O$$
$$N_2(C^3\Pi_u) + O_2 \rightarrow N_2(X^1\Sigma_u^+) + O + O$$

Molecular nitrogen is excited during the discharge phase in the triplet states (A^3, B^3, C^3). The efficiency of such excitation is rather high (Figure 17). Formation of electronically-excited nitrogen molecules and subsequent quenching of excited molecules in collisions with oxygen lead to oxygen dissociation. This channel of atomic oxygen formation is one of the most important channels of O production in the discharge. Conversion of atomic oxygen into ozone at atmospheric pressure conditions is a very fast process.

Excitation of electronic states of oxygen

$$O_2(X^3\Sigma_g^-) + e \rightarrow O_2(B^3\Sigma_u^-) + e$$
$$O_2(X^3\Sigma_g^-) + e \rightarrow O_2(\Pi) + e$$
$$O_2(X^3\Sigma_g^-) + e \rightarrow O_2(A^1\Delta_u) + e$$

$$O_2(el.excited) \rightarrow O(^3P) + O(^1D)$$
$$O_2(el.excited) \rightarrow O(^3P) + O(^3P)$$
$$O_2(el.excited) \rightarrow O(^1D) + O(^1D)$$

Direct dissociation of molecular oxygen by electron impact occurs through electronically excited states of molecular oxygen. The efficiency of this process is lower than the process of collisional quenching of nitrogen excited states but remains a very important mechanism of atomic oxygen formation.

Ions conversion to the radicals

$$N_2^+ + O_2 = N_2 + O_2^+ \quad (1)$$
$$O_2^+ + O_2 + M = O_4^+ + M \quad (2)$$
$$O_2^+ + e = O + O \quad (3)$$
$$O_2^+ + e + M = O_2 + M \quad (4)$$
$$O_4^+ + e = O_2 + O_2 \quad (5)$$

At high *E/n* values a lot of the discharge energy went into the gas ionization. This channel became the most important channel of energy losses for *E/n* > 1000 Td. Thus we needed to analyze the ion's kinetics and analyze atomic oxygen production by conversion of ions. The

main channel of atomic oxygen production is dissociative recombination of the molecular ion (3). The main ion during the discharge phase is the nitrogen ion (Figure 17), but the fast charge transfer process (1) leads to the quick formation of molecular oxygen ions. Mechanisms (1) and (3) lead to the conversion of ions into oxygen atoms as well as to ozone production. Three-body recombination (4) is also very important at high pressure conditions and suppresses the chain (1), (3) decreasing the molecular ion concentration and electron concentration. The most important path is the conversion of molecular oxygen ions into complex ions O_4^+ (2). This process is extremely fast at $P \sim 1$ atm and leads to a change in ion composition from O_2^+ to O_4^+. Dissociative recombination of complex ions does not lead to the formation of atoms (5). Thus, the mechanisms (2), and (5) also suppress atomic oxygen production in the discharge. We used the kinetic model [26] to estimate the dynamics of plasma recombination in the discharge afterglow. This was used to analyze the role of different mechanisms of recombination and the influence of ion formation on the atomic oxygen production in the discharge. The conclusion was made that under room temperature conditions gas ionization does not lead to the dissociation because of the very fast conversion of ions into complex ions (2) and because of dissociative recombination (5).

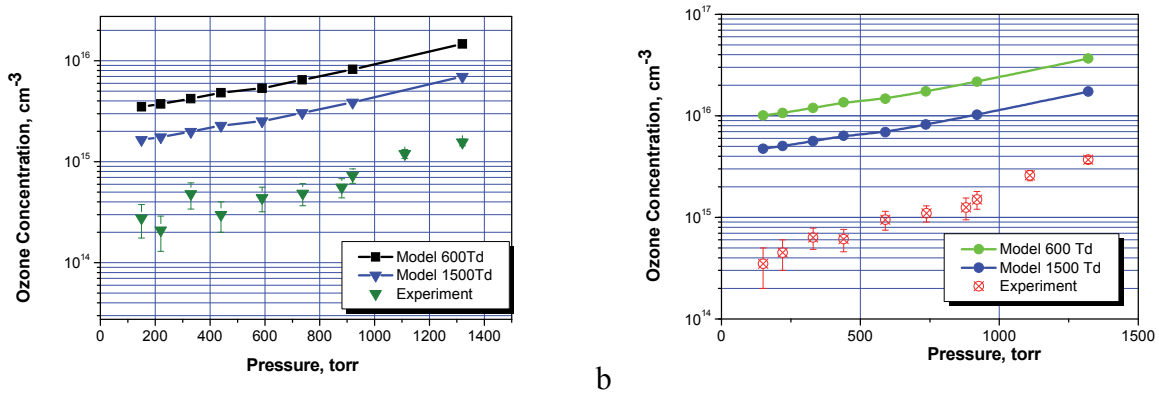

a b

Figure 17. Ozone production modeling. U = 9.5 kV (a) and 18 kV (b)

An increase in *E/n* value from 600 to 1500 Td leads to an ozone production decreased by a factor of 3 for all pressure ranges investigated. Nevertheless, the calculated amount of ozone production remains too high in comparison to the experiment (Figure 17).

Influence of the gas temperature

The ozone production decreases significantly with temperature growth. We assume that the main influence of the temperature increase is a decrease in gas density, and competition between reactions of ozone formation and decomposition:

$O_2+O+M \Rightarrow O_3 + M$ ($k_1 = 5.1\times10^{-27}\times T^{-2.3}$) (1)

and

$O_3+O \Rightarrow O_2+O_2$ ($k_2 = 8\times10^{-12}\times\exp(-2060/T)$) (2)

The rate coefficient of the reaction (1) decreases with the temperature, while the rate coefficient of the reaction (2) increases. As a result, a steady-state ozone concentration in the discharge afterglow depends on the temperature:

$$\frac{[O_3](T)}{[O_3](T_0)} = \left(\frac{T}{T_0}\right)^{-3.3} exp\left(-2060\left[\frac{T-T_0}{TT_0}\right]\right)$$

The ozone production measurements at different temperatures were made using the same technique (Figure 8). We varied the temperature of the discharge chamber from 293 K to 336 K (Figure 18). The decrease of the ozone concentration with the temperature increase indicates an important role of the gas heating in the discharge region on ozone formation.

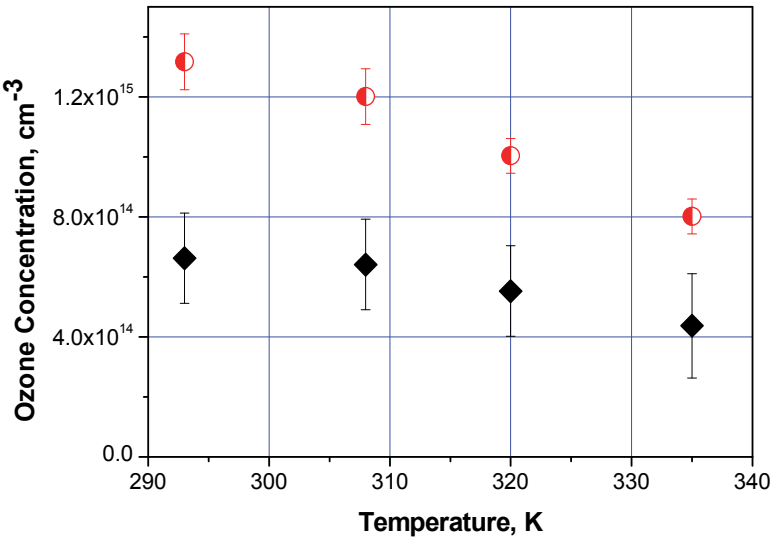

Figure 18. Ozone Concentration vs. Temperature. Single pulse regime, Pressure 1 atm, U = 9 kV (black symbols) and 18 (red symbols) kV on the gap.

It should be noted, that the temperature of the ambient gas affects the ozone formation by several different ways: it changes the kinetics in the discharge afterglow, but simultaneously changes the discharge itself, decreasing the gas density and increasing reduced electrical fields *E/n*. The second effect does not work in the case of gas heating by the discharge – in this case the discharge propagates in the gas with initial parameters and only later the energy transfer

processes will increase the gas temperature and pressure. Further gas expansion decreases the pressure. This difference should be taken into account for analysis of the ozone formation at different temperatures (Figure 18).

Temperature measurements in ns-SDBD

Gas temperature dynamics was measured using emission spectra of the 0–0 transition of the second positive system of nitrogen with nanosecond resolution. The quartz lens focused the emission of the discharge onto the slit of the monochromator. The output optical plane of the monochromator was adjusted to the photocathode of the high-speed camera, which was synchronized with the high-voltage pulses. The exposure time was equal to 100 ns. During one experiment the full rotational spectra of the 0–0 transition of the second positive system of molecular nitrogen was obtained. To increase the signal-to-noise ratio, we collected and averaged 2000 spectra in one regime (Figure 19).

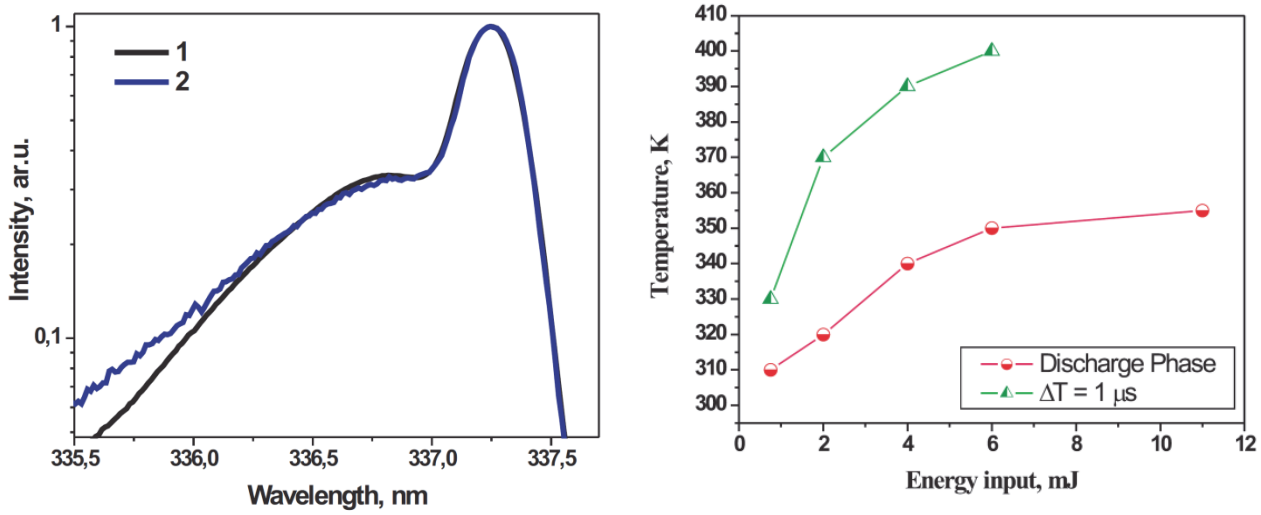

Figure 19. Temperature measurements in ns-SDBD. Left: emission intensity distribution in 0-0 band of 2+ system of nitrogen. 1 - ICCD time shift is 0 ns, 2 - 1000 ns after the discharge start. ICCD gate is 100 ns. Right: gas temperature measured in plasma and plasma afterglow after the discharge vs ns-SDBD energy input. Pulse voltage U = 14 kV, pulse duration 20 ns.

We compared this spectrum with the one calculated at a given temperature (see details in [16,18,22]). This procedure allows us to estimate the rotational temperature of the molecules. The gas temperature dynamics was measured using the additional coaxial cable connected with the actuator. The length of the additional cable was varied from 0 to 100 meters. The high-voltage pulse travelling through the additional coaxial line led to initiation of an additional weak discharge with a delay of up to 1 μs. The energy input in this additional discharge was about 10% of the main discharge. Direct temperature measurements with nanosecond temporal resolution were performed to estimate the part of the energy that was quickly converted into heat (Figure 19). In [22], it was found that the temperature increase is 200 K *(*290→490 K*)* after 1 μs at U = 17 kV (an energy input of 0.2 mJ mm^{-1}*)*. At lower voltage, U = 12 kV, it was found that the temperature increase was 70 K *(*290 → 360 K*)* during the discharge phase and 110 K

*(*290 → 400 K*)* after 1 μs (an energy input of 0.1 mJ mm^{-1}), which is in an excellent agreement with the current results (Figure 19).

Mechanisms of fast gas heating in air plasmas at high *E/n*

Mechanisms of fast gas heating for low electrical fields (*E/n* < 20 Td) mainly include elastic electron scattering and electron-impact rotational excitation of molecules. Here, the typical relaxation time is rather short because of fast energy exchange between rotational and translational degrees of freedom. The total energy fraction of this excitation is very small (see Figure 20). According to this data, at moderate electrical fields (*E/n* = 20 - 100 Td) there is efficient excitation of vibrational and electronic degrees of freedom. VT relaxation under low temperature conditions is slow and almost all the vibrational excitation energy is "frozen" for about 100 sec (at 1 atm) before real gas heating takes place [27]. Under such conditions formation of a shock wave (strong perturbations) is impossible. Instead, weak compression waves will appear. Under higher *E/n* (100-200 Td), efficient excitation of electronic degrees of freedom and molecule dissociation will take place (Figure 20). Dissociation by electron impact takes place through repulsive states and 20-30% of the electron energy goes directly to the translational motion of fragments (for example, $e + O_2 \rightarrow e + 2O + \Delta E$). Collisional quenching of electronically excited states (in air there are nitrogen triplets – N_2(A, B, C, a', ...) also leads to energy release into translational degrees of freedom:

$$e + N_2 \rightarrow e + N_2^*(A, B, C, a', ...)$$
$$N_2^*(A, B, C, a', ...) + O_2 \rightarrow N_2 + 2O + \Delta E$$
$$O(^1D) + N_2 \rightarrow O + N_2 + \Delta E$$

This mechanism was proposed for air in [7].

In SDBDs, the reduced electrical field reaches extremely high values (*E/n* ~ 800-1200 Td) when a significant part of the electron energy goes to gas ionization. Extension of the energy relaxation mechanism to high *E/n* values was proposed in [8]. We have analyzed the results of two experiments with nonequilibrium air plasmas produced by high-voltage nanosecond discharges. These results involved the measurement of the velocity of a shock wave that propagated through air, heated by a pulsed discharge at 20 Torr and the experimental study of a SDBD in atmospheric-pressure air. The electron power transferred into heat in air plasmas was estimated in high (~10^3 Td) electric fields. It was shown that around 50% of the discharge power can be transferred into heat for a short period of time (~ 1 μs at atmospheric pressure). This effect is much more profound than that observed at low and moderately reduced electric fields.

A kinetic model was suggested to simulate the fast heating of air plasmas under the conditions considered [8]. This model extended the kinetic schemes developed previously for describing

fast heating in moderate (~10^2 Td) reduced electric fields. The model takes into account electron-impact excitation of high-energy states followed by their collisional quenching, as well as ion–molecule reactions and electron–ion and ion–ion recombination processes 8]. These reactions play an important role in plasmas produced at high electric fields when electron energy losses due to electron-impact ionization play an important role. Based on this model, the fractional electron power transferred into heat was calculated as a function of the reduced electric field in dry and humid air at various pressures. Calculations agreed well with the results of the experimental analysis of the SDBD at atmospheric pressure. There was also reasonable agreement between the theory and the measurements in the pulsed high-voltage nanosecond discharge initiated in the air at 20 Torr.

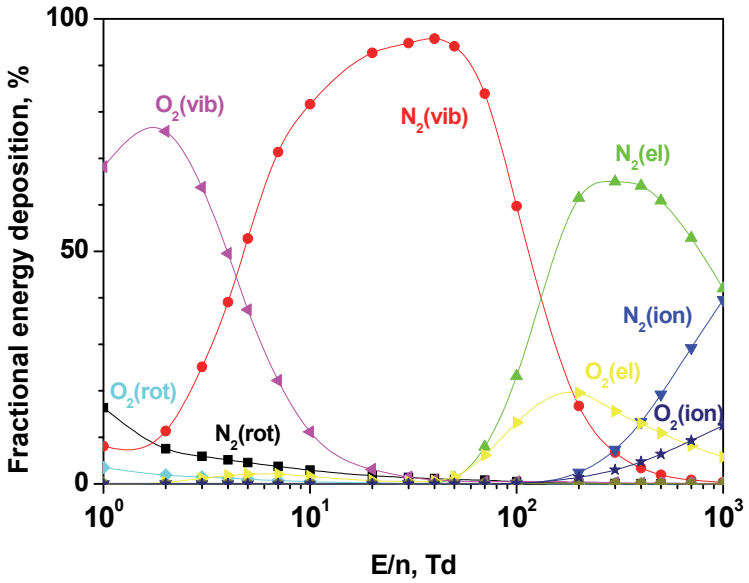

Figure 20. Fractional electron power dissipated into the different degrees of freedom in air as a function of *E/n* [6].

According to the calculation at 20 Torr, approximately equal parts (~10%) of the electron power are converted into heat; (i) through electron-impact dissociation of O_2 and excitation of N_2*(A,B,C,a)* states followed by quenching by O_2, which are suggested to describe fast gas heating in air plasmas at moderate electric fields; (ii) through electron-impact excitation of higher electronic N_2 states followed by dissociation and quenching by O_2 and (iii) through electron–ion recombination. At atmospheric pressure, the calculated total fractional electron power transferred into heat could be increased by ~20% due to three-body recombination of positive and negative ions and, to a smaller extent, due to ion–molecule reactions in the discharge afterglow. Thus, total energy transferred into heat by "fast" mechanisms in air plasma at low pressure conditions is ~30-40%, at atmospheric pressure ~50-60%. The calculations

showed that, under the conditions considered, the characteristic time of gas heating lies in the range 0.3–5 ns for 1 atm and in the range 5–80 ns for a pressure of 20 Torr (Figure 21).

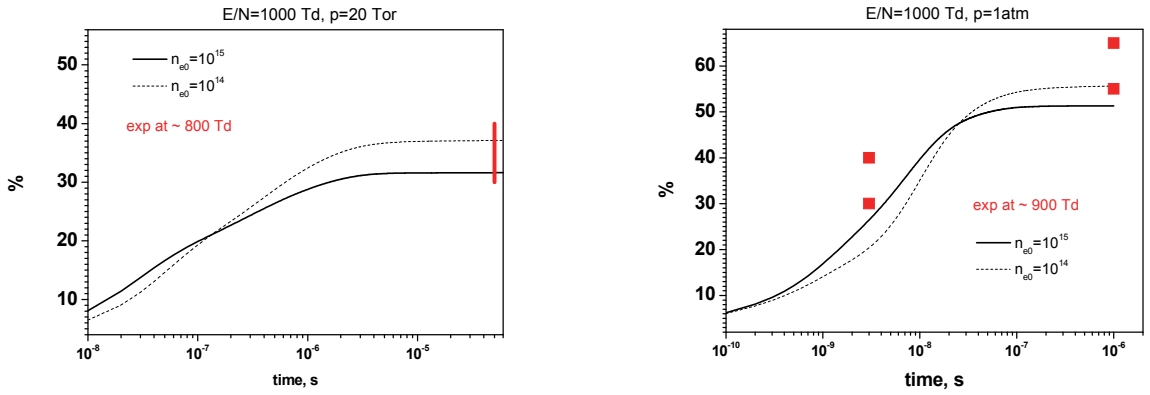

Figure 21. Evolution in Time of Total Fractional Electron Power Transferred into Heat in Dry Air [8]. Left: P = 20 Torr; Right: P = 760 Torr [8].

Ozone formation in the plasma afterglow

To develop a kinetic mechanism of fast gas heating in air at high *E/n*, assumptions must be made about the branching ratios of some important reactions. For instance, the products of the dominant recombination reactions for charged particles in air are well understood only for dissociative electron recombination with O_2^+ ions,

$$e + O_2^+ \rightarrow O + O.$$

In this case, the branching ratios for O atoms in various excited states have been measured [28]. Information about branching ratios for electron recombination with other important ions (O_4^+, etc.) and for ion-ion recombination is absent. To calculate the electron power converted into heat, it was assumed in [8] that, in these recombination reactions, the released ionization energy is spent on gas heating rather than on the dissociation of molecules. Because of this assumption, the effect of fast gas heating can be somewhat overestimated in this calculation. Nevertheless, this assumption allows agreement between measurements and calculations, not only for the electron power rapidly converted into heat (see [8]), but for the concentrations of ozone produced in the SDBD plasmas.

As a result, both factors – fast temperature increase in the discharge and decrease of the efficiency of atomic oxygen generation because of O_4^+ cluster ions formation lead to a significant decrease of ozone production in ns-SDBD. These two mechanisms completely describe the reduction of the ozone yield in the discharge (Figure 22).

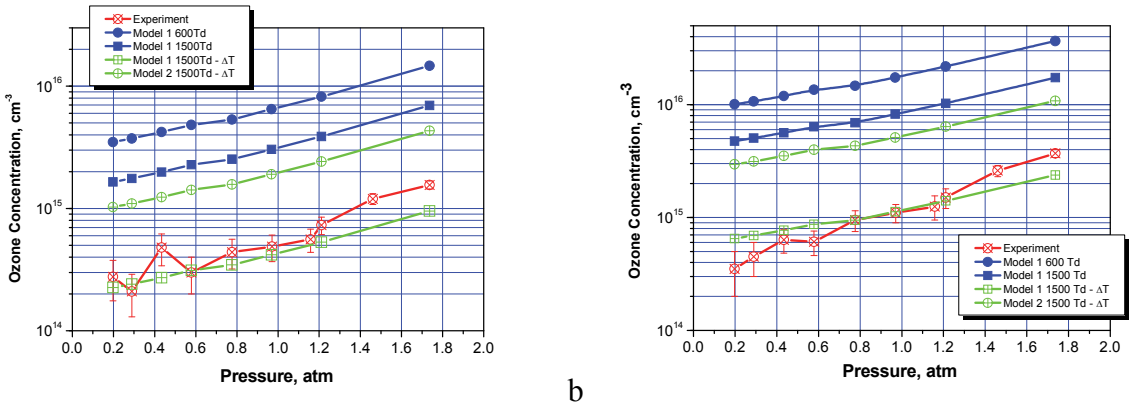

a b

Figure 22. Ozone production modeling. U = 9.5 kV (a) and 18 kV (b). Model 1 represents the results of present paper; Model 2 is calculations with the model [23]. Δ*T* mark shows where the fast temperature increase because of plasma recombination was taken into account.

The kinetic model developed in [23] for fast gas heating was based on somewhat different assumptions. In particular, it was assumed that any recombination of positive oxygen ions with electrons or negative ions is accompanied by O_2 dissociation to form two O atoms. As a result, the electron power rapidly converted into heat at very high (~ 1000 Td) *E/n* did not exceed 40 %. In earlier work the value obtained had been around 50% [8]. The branching ratios used in [23] for the recombination processes in air plasmas follows from available interpretations of the measured yield of ozone in pulse radiolysis of gaseous oxygen at high doze radiation [29-31]. It should be noted that if it were admitted that O atoms are efficiently produced in electron recombination with cluster positive ions and in ion-ion recombination, it would lead to an increase in the calculated concentration of ozone produced in the SDBD not only because of increased concentration of atomic oxygen, but also because of the decrease of the energy amount transferred into heat during “fast heat” stage. Thus, the mechanism proposed in [23] leads to a significant disagreement with present experiments (Figure 22).

Thus, ozone formation in surface DBD was experimentally measured for a large pressure range. Temperature and *E/n* influence were investigated. It was shown that both parameters significantly influence the mechanism of ozone formation. Decreases in pressure lead to a significant increase in *E/n* value in the discharge and reduce the efficiency of oxygen dissociation as well as ozone formation. The temperature increase decelerates reaction of atomic oxygen conversion into ozone and accelerates secondary reactions of ozone decomposition. It was shown that high-voltage pulsed nanosecond discharge due to extremely high *E/n* value produces a smaller ozone concentration in comparison to other discharges. The kinetic model was proposed to describe ozone formation in the pulsed nanosecond SDBD.

NS dielectric barrier discharge development and thrust generation

We use the FID pulser (4-channels, maximal voltage 35 kV, frequency 30 kHz, pulse length 15 ns, interchannel jitter less than 100 ps) for nanosecond excitation of the gas. This pulser is externally controlled by BNC Model 575 8-challel synchro-source.

The measurements of dynamics of multi-electrode NS-SDBD are based on the combination of several pulsed discharges. Phase synchronization of the discharges allows us to remove the residual charge from previous discharge and, as a result, the NS discharge could generate a significant trust. Figure 23 demonstrates the principles of the new actuator design and operations.

The first discharge starts at time moment τ_1, and transfers the charge to the surface. The second discharge is synchronized with the trailing edge of the first pulse, and removes the negative charge of first discharge downstream. The mechanism could be described as a controlled breakdown of the gas gap between first and second pairs of electrodes. Simultaneously the second pulse increases the positive charge on the surface further downstream. The third pulse starts at the moment of the voltage decrease on the second pair of electrodes; this pulse transfers the charge further to the right and prevents the reverse discharge formation on the second pair of electrodes. The forth pulse is synchronized with the trailing edge of the third pulse and serves as a charge removal mechanism only.

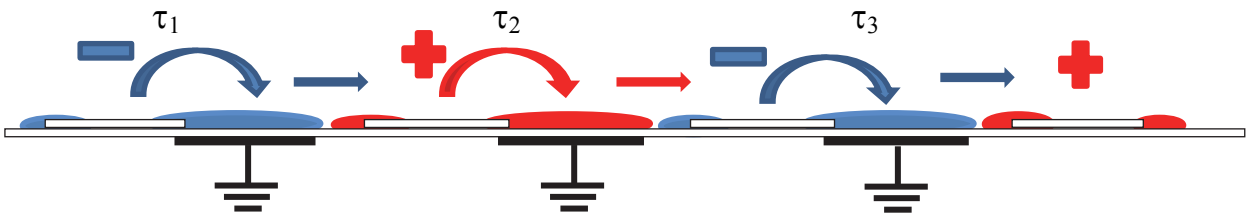

Figure 23. Charge transfer mechanism and discharge synchronization for Combined Energy-Momentum Actuation.

We can place any number of electrode pairs increasing the total charge transfer per single sequence of pulses and increasing the induced momentum. The pulsed discharge has reduced limitations on the electric field applied compared to low-frequency AC driven discharges; a typical electric field in the nanosecond driven SDBD is 10 times higher than the arc breakdown threshold; thus, we can expect approximately 10 times the induced velocity increase with compare to typical AC plasma actuators. The price of the induced velocity increase is the precise

synchronization between discharges in nanosecond time scale. For these experiments the 4-channel pulser described above is used.

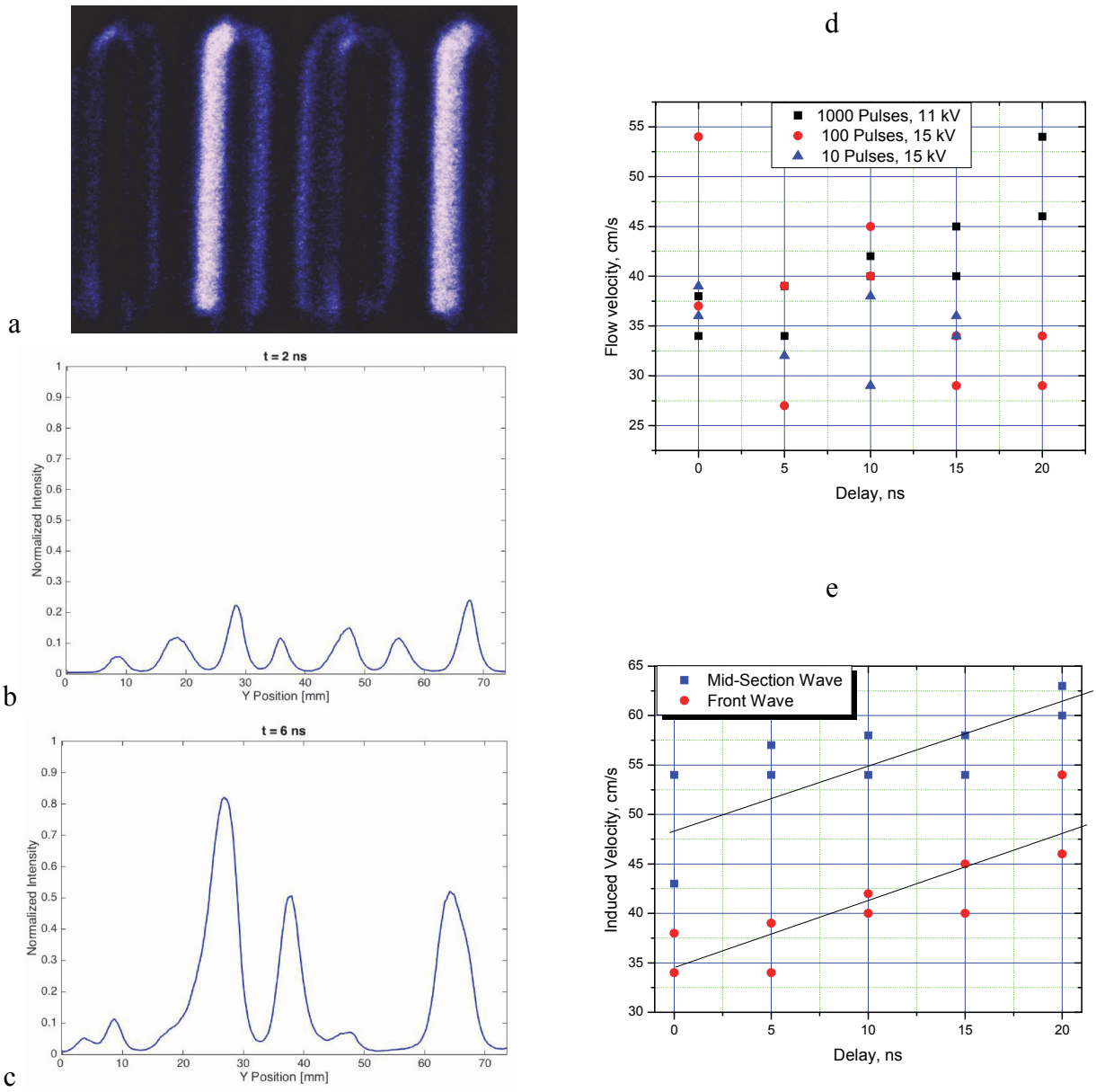

Figure 24. Dynamics and thrust generation by multi-electrode NS-SDBD. a) Image of the discharge development. ICCD gate is 1 ns, time from the discharge start 2 ns. b) Emission profile at t = 2 ns; c) Emission profile at t = 6 ns; d) Induced flow velocity for different number of pulses; e) Induced flow velocity for 1000 pulses vs delay time between discharges.

Figure 24 demonstrates the 4-electrode NS-SDBD development. Fig. 24a shows the discharge at t = 2 ns after the high-voltage pulse start. The delay time between discharges is zero, and all four ionization regions develop with almost the same dynamics. Fig. 24b shows the emission profile at the same time moment. All 8 ionization waves demonstrate the same luminosity. In 4 nanoseconds (Figure 24c) the positive and negative waves start to interact and local electrical field in the interaction region and gas excitation increases dramatically.

The induced flow was measured using shadow visualization of the flow development (Figure 24 d, c). Figure 24 d shows the induced velocity vs number of NS pulses, and figure 24 e demonstrates the dependence of induced flow speed on the delay time between consequent discharges.

Thus, the "pull-it-forward" concept of NS DBD was demonstrated for the first time. Momentum generation by synchronized NS-SDBD is shown. Further optimization of this configuration could provide a significant surface jet formation together with the pulsed flow excitation by NS energy release in the discharge.

Multi-diode asymmetric surface

We have developed a major redesign of the SDBD surface. With ARO DURIP funding, we work with United Silicon Carbide, Inc. to design a device with Schottky barrier diodes inlaid into the surface as shown in Figure 25. Thin (0.150 mm) metal strips are embedded in a dielectric matrix and connected together with SiC diodes that are sealed into the dielectric material (Figure 25). The number of the diodes has been reduced to 30 across a 1 cm square tile, corresponding to a 0.33 mm cycle spacing.

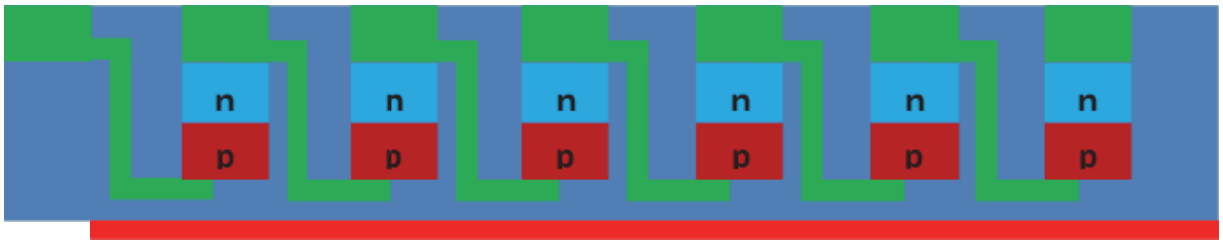

Figure 25. New semiconducting dielectric concept for suppression of backward breakdown. Green, red – metal layers; Blue – dielectric material; np – 1A, 650V blocking SiC Schottky diodes.

The surface demonstrated in Figure 25 has a selective conductivity. The negative polarity pulse generates the surface dielectric barrier discharge above the surface from left to right, while the backward breakdown is suppressed because of high reverse conductivity of the structure.

The key element of the structure is a miniature high-frequency, high-voltage blocking Schottky diode. United Silicon Carbide, Inc offers the xR series of high-performance SiC Schottky diodes. With zero reverse recovery charge and 175°C maximum junction temperature, USCI's diodes are ideally suited for high- frequency and high-efficiency power systems with minimum cooling requirements. These diodes feature:

- Positive temperature coefficient for safe operation and ease of paralleling
- 175°C maximum operating junction temperature
- Extremely fast switching not dependent on temperature
- Essentially no reverse or forward recovery
- Maximum DC forward current: 1 A
- DC blocking voltage: 650 V
- Forward voltage: 1.25 V

Figure 26 summarizes the performance of the SiC diodes. Typical direct voltage for the entire structure based on these diodes could be as low as U_R = 30×1.25V = 37.5 V/cm. Peak direct current is adjusted to ~50 A. Breakdown voltage reaches U_B = 30×650V = 19500 V/cm.

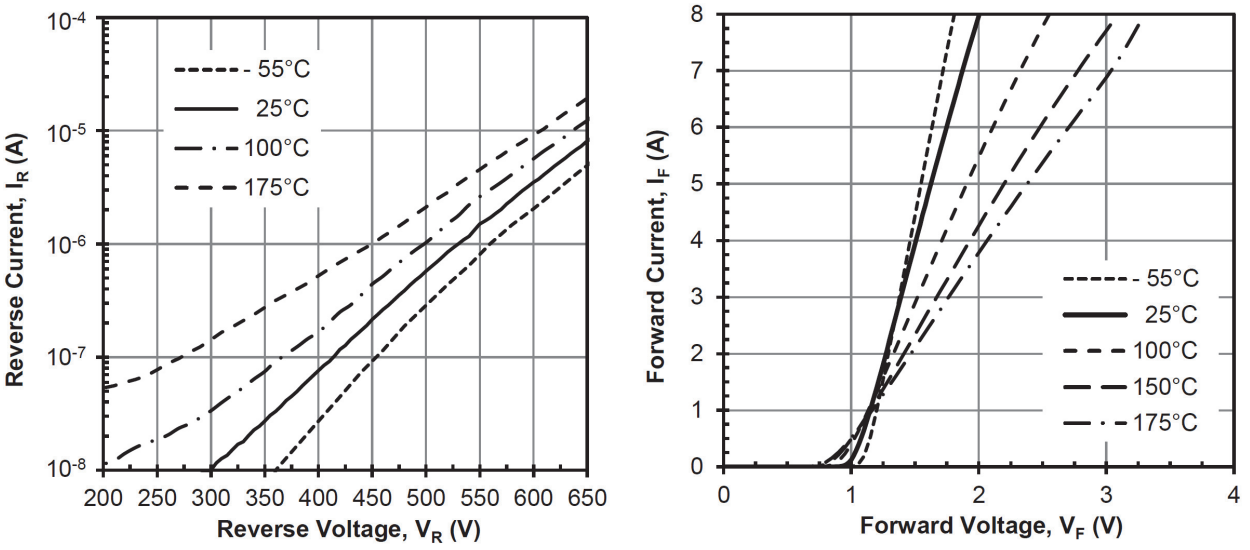

Figure 26. Typical performance of blocking SiC Schottky diodes. A) Reverse characteristics; B) Forward characteristics.

The proposed design allows solving all major problems of the previous version. Specifically, there are no edges and gaps between separate blocks; no exposed connecting wires; much lower direct voltage. Breakdown voltage is limited by ~20 kV, which allows using a wide range of experimental conditions. Very high operational temperature of the diodes (up to 175C) allows high-frequency operations. Thus, the new equipment allows a significant improvement in ionic wind generation by surface dielectric barrier discharges due to high efficiency in backward breakdown suppression and possibilities for high-frequency operations.

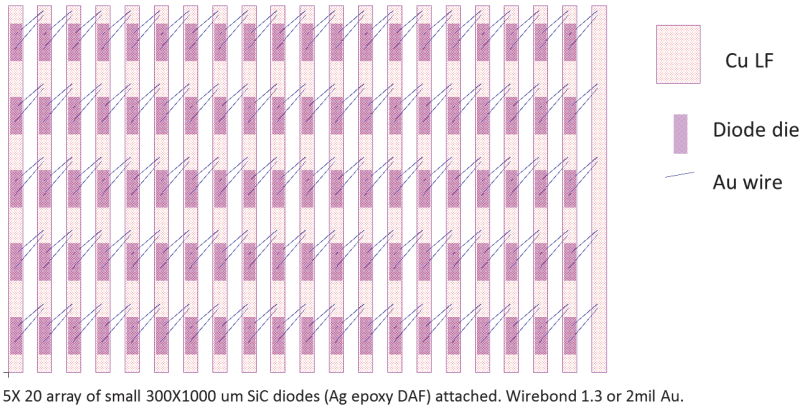

Figure 27. QFN diode array – assembling design by United SiC, Inc. for semiconducting dielectric material concept for suppression of backward breakdown.

.

Figures 27, 28 demonstrate the assembling design for a QFN diode array. The actual design is shown in figure 29.

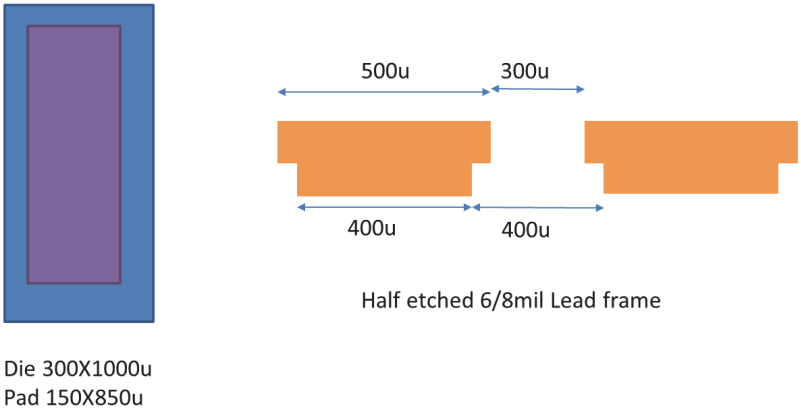

Figure 28. Die size and lead frame details.

QFN diode array manufacturing and assembling

The first step of QFN packages assembling was a custom SiC diodes fabrication. Device yields were excellent, ~99% on three of four wafers. Wafer #1 has somewhat reduced yild, ~92%, possibly related to the intrinsic wafer defects. Low forward voltage drop, V_f ~ 1.4 V, has been demonstrated at rated forward current I_f = 1A per diode. Low reverse leakage currents, Ir < 50 nA, have been demonstrated at rated blocking voltage V_r = 650 V.

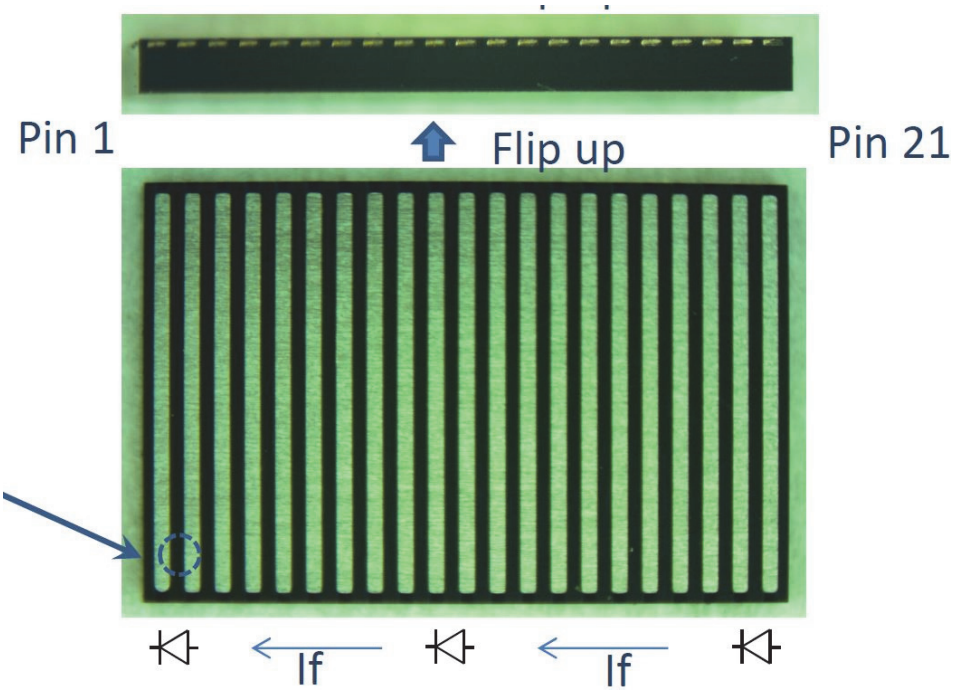

Figure 29. Photo of actual design of the QFN package.

Figure 29 demonstrates the design of the diode surface. Conductive stripes are connected to each other by SiC diodes. The distance between conductive strips is about 0.4 mm. These gaps are filled by plasma during the high-voltage pulse. Above the conductive surfaces the electric field is much weaker than in the gaps, but because of small strips size the plasma zones overlap each other at some distance above the surface.

SiC surface test results

Figure 30 shows the oscillograms of high-voltage pulses used for plasma formation experiments. Three voltages were used: 20 kV, 10 kV and 7 kV. The pulses have a typical rise time ~3 ns, and a total pulse duration ~25 ns. Figure 31 demonstrates dynamics of the emission of second positive system of nitrogen ($N_2(C^3)\rightarrow N_2(B^3)$ transition) in air. Fast quenching of the upper state by molecular oxygen allows to trace the dynamic of the state excitation by electron impact. The

time step between frames is 1 ns, and the ICCD camera gate is also 1 ns. It is clear that the SiC diode surface for the pulse polarity chosen acts almost as a conductive cupper strips and suppresses the plasma formation over the surface. It means that the conductivity of SiC surface is high enough to redistribute the electric potential and reduce the electric fields. The discharge propagates only above the dielectric surface around the metal strips and the diode surface (Figure 31). After t=25ns above the dielectric surface the reverse breakdown formation is observed. The SiC surface shows no reverse discharge in these conditions. This demonstration indicates the possibility to control the reverse breakdown even at high pressure conditions using diode surfaces.

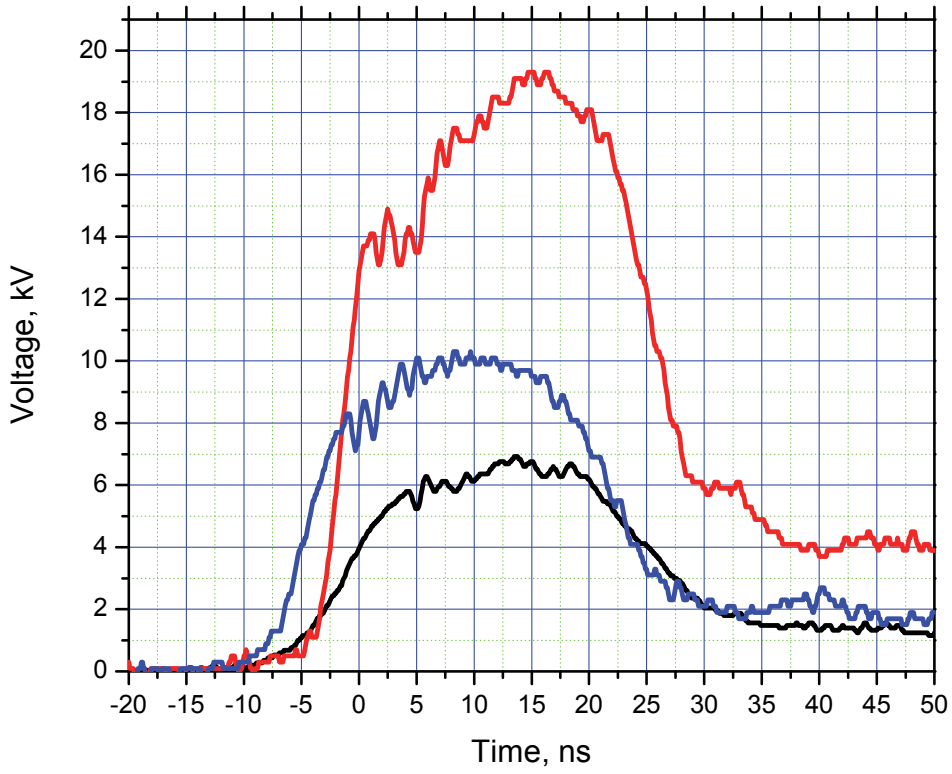

Figure 30. NS high-voltage pulses used in experiments.

Thus, new configuration of multi-diode asymmetric surface was developed using high-current SiC diodes. The new equipment allows a significant improvement in ionic wind generation by surface dielectric barrier discharges due to high efficiency in backward breakdown suppression and possibilities for high-frequency operations. New SiC diodes-based design is proposed to increase the induced jet velocity. The design demonstrates much better performance than an old version of SiC-based diode surface.

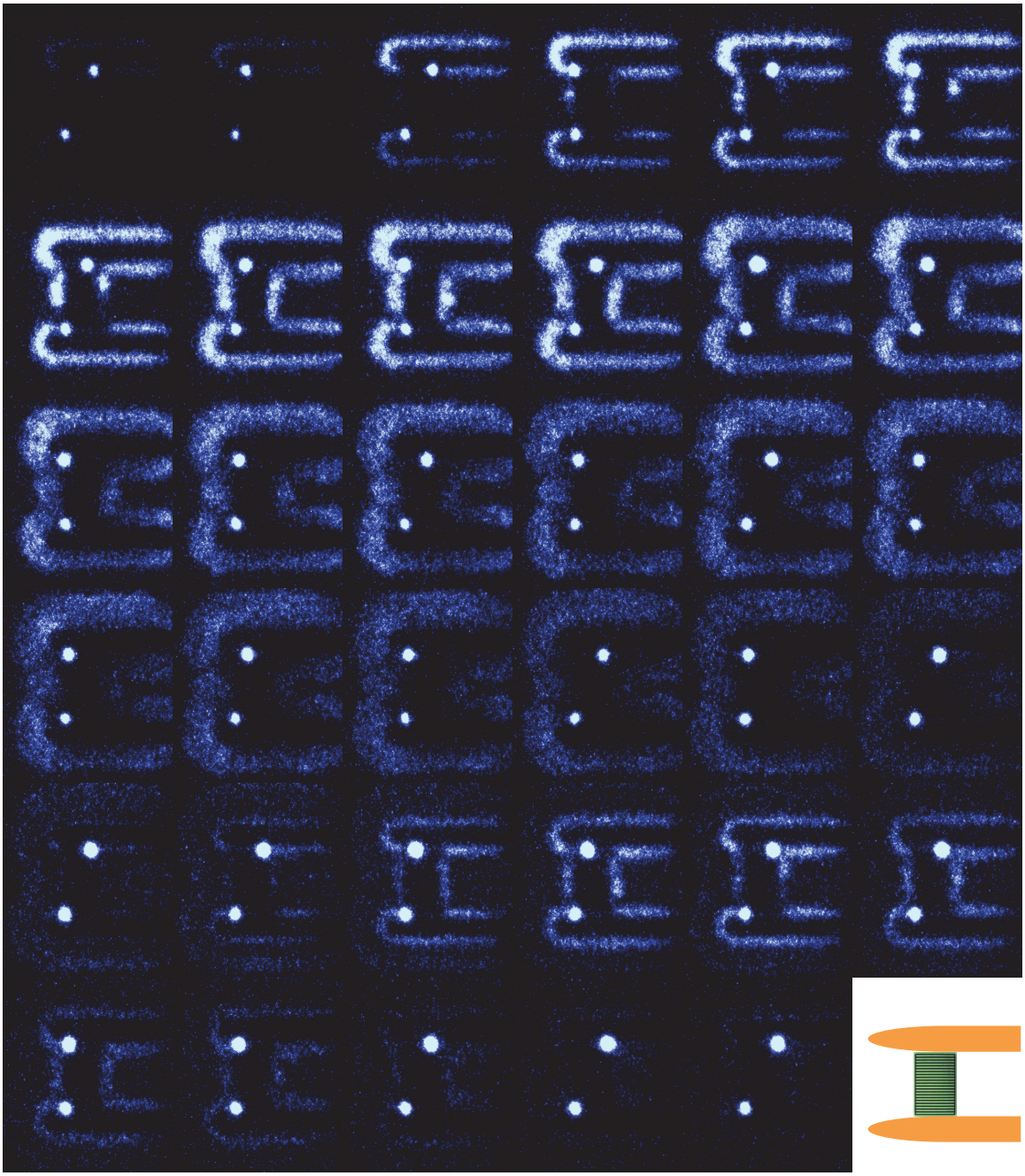

Figure 31. NS SDBD discharge development and plasma generation over the SiC diode surface. U = 20 kV, P = 1 atm, air. Camera gate t = 1 ns, step between frames dτ = 1 ns.

Plasma-assisted Boundary Layer Separation Control

The potential for active flow control by low-temperature plasma is considered to be one of the most promising topics in aerodynamics today. One device that has been widely studied for flow control is the Dielectric Barrier Discharge (DBD). Figure 32 shows the basic arrangement of a DBD plasma actuator. High voltage is supplied to electrodes that are separated by a dielectric material. A plasma discharge, like the one shown in the photograph in Figure 32, in the presence of the electric field gradient produces a body force.

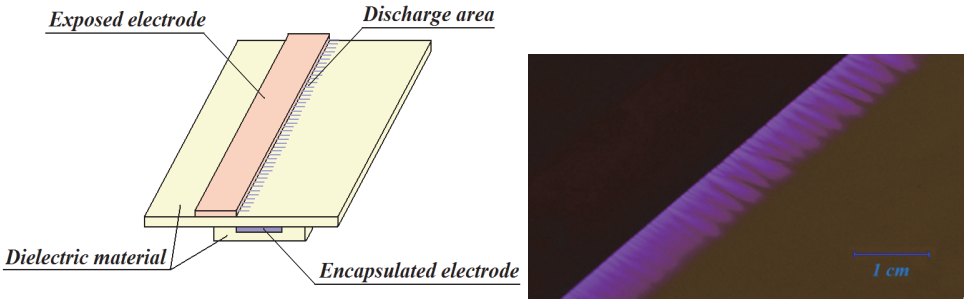

Figure 32. Schematic of the conventional dielectric barrier discharge actuator and photograph of the plasma discharge [32].

Low-speed experiments

Boundary layer separation control by nonequilibrium non-thermal plasma was reviewed in [33] and [34]. In addition, the recent review [35] includes many results of all mechanisms (thermal, electrostatic and MHD) and some applications for flow control for subsonic and supersonic regimes. Paper [36] proposed using pulsed nanosecond periodic discharge for plasma actuator. The *E/N* value for this type of the discharge can exceed the breakdown threshold by several times. The high value of the reduced electric field seems to be an evident advantage of such a discharge. Such characteristics as relatively low energy consumption, the possibility of using such discharges within a wide range of pressures, flow velocities, and gas compositions, including high humidity, also contribute to the advantages of the approach proposed. The first experiments [36] showed that it is possible to firmly control the boundary layer separation using this nanosecond pulsed discharge at velocities up to 75 m/s and energy consumption lower than 1 W/cm of wingspan.

Further, the impact of pulsed sliding discharge on the flow separation has been investigated in [37]. The high efficiency of pulsed discharge was shown for the velocity up to 110 m/s. The main mechanism of plasma influence was concluded to be the boundary layer turbulization, rather than the gas acceleration. An optimum pulsed actuator frequency was found to maximize the actuator effect on lift and drag force and flow re-attachment, such as $f_{opt} = U_0/L$, where U_0 is the main flow velocity and L is the typical distance along the surface to the separation zone. Later, this result was confirmed by Patel et al. [38] in experiments for chord Reynolds numbers up to 10^6 and a maximum free-stream speed of 60 m/s.

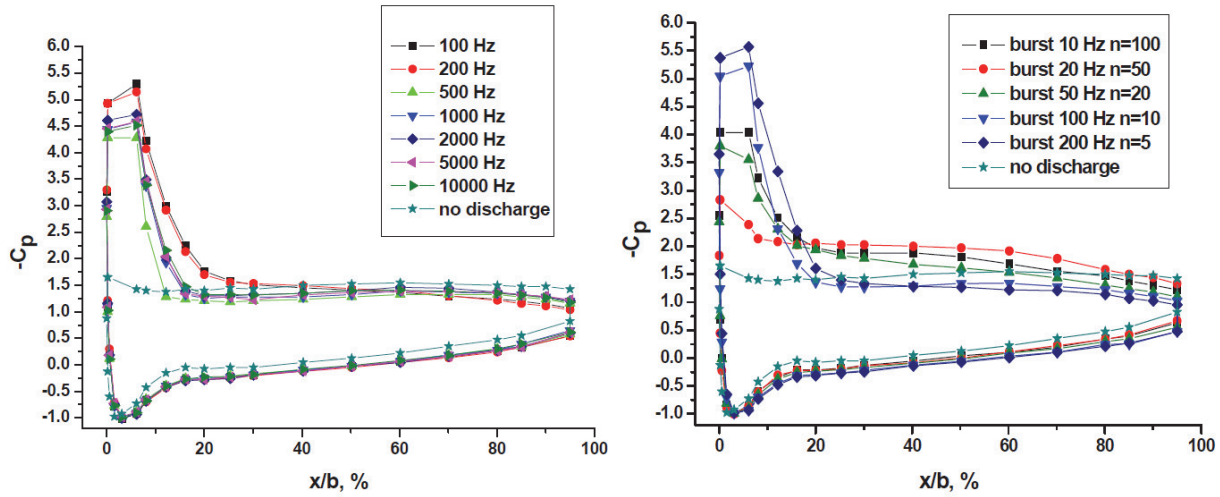

Figure 33. C_p distribution along the model chord
($\alpha = 19^0$; $U^\infty = 19$ m/s; $V = 24$ kV; Re = 0.8×10^6) [39].

Scaling effects of an aerodynamic nanosecond pulsed plasma actuator were investigated in [39]. Separation control experiments on a rectangular wing (dimensions 0.5×1 m^2) were carried out using a dielectric barrier discharge plasma at subsonic speed for chord Reynolds numbers from 0.35 to $0.875\cdot10^6$. Surface pressure measurements and flow visualization show that global flow separation on the wing can be mitigated or eliminated by the plasma actuators (Figure 33). The data were obtained for a wide range of attack angles, flow speeds, plasma excitation frequencies and power. New applications of several kinds of voltage pulses for plasma excitation were discussed, including microsecond and nanosecond pulses. As in [37], it was found there that control efficiency strongly depends on discharge frequency (Figure 34).

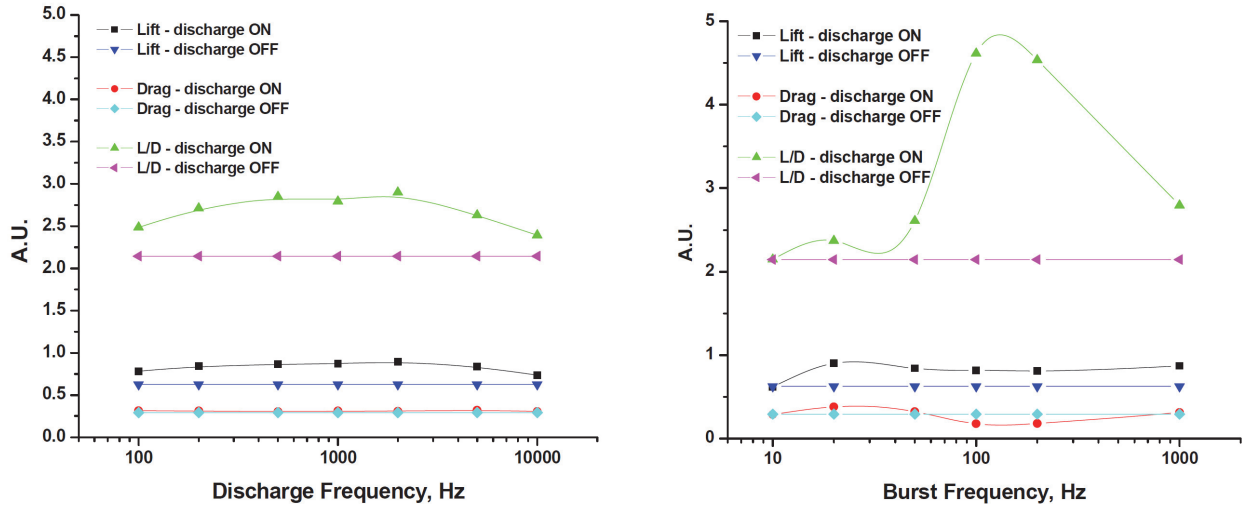

Figure 34. Lift, Drag force and Lift-to-Drag ratio in dependence on the frequency. $\alpha = 22^0$; $U^\infty = 17.4$ m/s; a) – Periodic Mode, $P = 2.5$-250 W for $f = 100 – 10000$ Hz, respectively; b) – Burst Mode, $P = 25$ W for all regimes [39].

High-speed experiments

Separation control experiments on a rectangular wing were carried out using nanosecond dielectric barrier discharge plasma at subsonic speed (M = 0.3 - 0.75) for chord Reynolds numbers between 0.5 and $2 \cdot 10^6$ [35]. This work has demonstrated the possibility to control the flow at cruising velocity with a plasma actuator. A vacuum blow-down wind tunnel has been used for the experiments at transonic velocity. The system was modernized to perform the experiments in pulse regime. The nozzle with working chamber operates at Mach numbers from M = 0.6 to M = 0.9. Figure 35 depicts the installation.

The discharge impact on the flow pattern near the surface has been investigated. The Mach number was equal to M = 0.65 − 0.6; 0.7 − 0.65; or 0.74 − 0.69 in different experiments. The discharge frequency in the experiments was equal to 5 kHz. High-voltage pulses have amplitude of 25 kV, pulse width was 12 ns. Discharge energy was equal to 10 mJ/pulse. The plasma impact was investigated for angles of attack between 0 and 30^0.

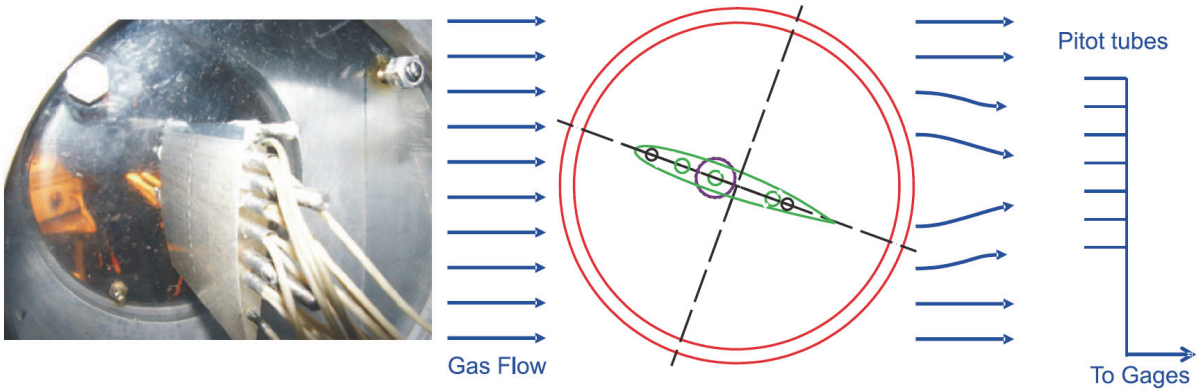

Figure 35. Photo of the model and schematics of pressure measurements. Pressure distribution have been measured in the wake of model and on the model surface [40].

An unseparated flow regime with local supersonic zone and shock wave formation was observed for small angles of attack. These regimes were clearly identified by the pressure jump in the middle of the airfoil surface. This jump is associated with the shock wave location (Figure 36). The discharge impact for angles within the range of $0 - 15^0$ is negligible. For higher angles of attack, the flow separation is observed and the pattern of pressure distribution changes (Figure 36). For angles of attack higher than the stall angle, the discharge switches the flow to the unseparated flow regime. Figure 36,a presents the pressure distribution on the upper surface of the model. The X-value corresponds to the distance from the leading edge of the model to the pressure port. The discharge was able to remove high-frequency pulsations in the wake of the model. The data from the pressure gauges for Mach number M = 0.7 are presented in Figure 36b to illustrate the noise reduction. Gauge 1 recorded the pressure at the upper surface of the model and shows the change in the angle of attack. Gauges 2-4 were placed in the wake of the model. Pressure pulsations in the wake disappear when the discharge is switched on. This effect was observed at high angles of attack (starting with $\alpha = 24^0$) for Mach number M = 0.65−0.75. The mean pressure value near the model surface does not change significantly, while high-frequency pulsation amplitude decreases dramatically. Thus, the study of separation control for the model of C-141 airfoil has been carried out at transonic velocities (M = 0.65 − 0.75). Dielectric barrier discharge plasma was used for separation control. The effects of the angle of attack and flow Mach number on the efficiency of flow control were studied in experiments. Nonequilibrium plasma impact was observed for angles of attack from 18^0 to 30^0.

The discharge removes both flow separation and high-frequency pulsations in the wake. These experiments demonstrate a possibility of transonic flow separation control using low-energy pulsed nanosecond surface dielectric discharges.

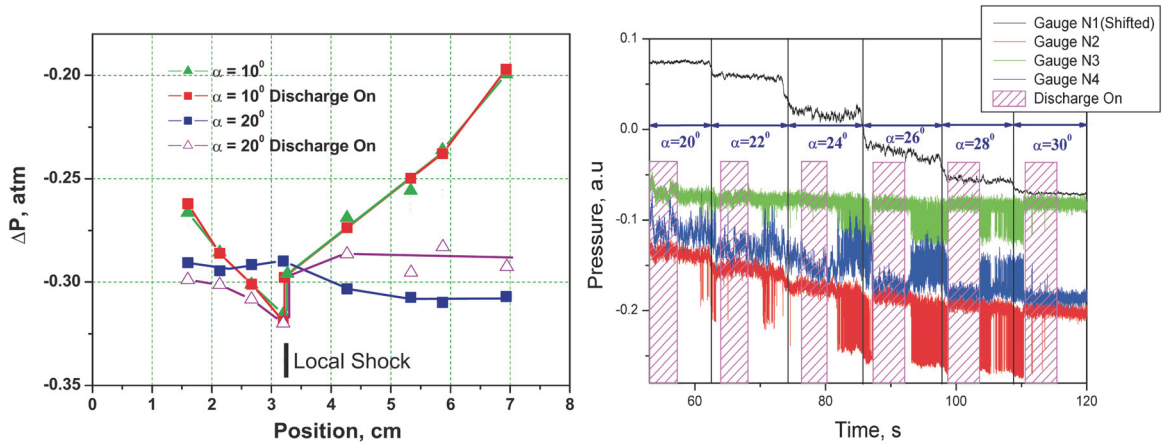

Figure 9. a) Pressure distribution on model surface with and without discharge. Mach number M = 0.74. Total pressure P = 1 atm. b) Noise reduction in the wake of the model. Mach number M = 0.7. Total pressure P = 1 atm [40].

Mechanism of actuation by NS SDBD

Thus, nanosecond pulsed discharges have demonstrated an extremely high efficiency of operation for aerodynamic plasma actuators over a very wide velocity (M = 0.03 - 0.75) and Reynolds number (Re = 10^4 - 2×10^6) range. For further technological development, it is extremely important to understand the physics of the nanosecond plasma actuator and differences between different types of SDBD in terms of their efficiencies [3,16-20].

From this point of view there are several important milestones. Paper [37] experimentally demonstrated that the pulsed nanosecond high-voltage discharge used for boundary layer separation control in a wide range of free stream velocity produces no gas acceleration. In [41] the use of a steady counter-flow DBD actuator as a boundary-layer control device was numerically analyzed. According to calculations, the actuator induced transition and turbulence, and generated a fuller velocity profile. This feature was exploited to delay stall of a NACA 0015 airfoil at high angle of attack using a pulsed counter-flow actuator. Thus, [16] demonstrated that the co-flow gas acceleration is not necessary for boundary layer control. In [16] the mechanism

of pulsed nanosecond high-voltage discharge influence on boundary layer separation was experimentally demonstrated. It was shown that fast nonequilibrium plasma thermalization (on the time scale of hundreds of nanoseconds) produces hot, over-pressurized gas layer in the discharge zone, followed by strong shock wave formation. It should be noted, however, that the shock wave itself does not significantly affect the flow. The most important process is the interaction of the gas density and velocity gradients in the shear layer between the separation bubble and the main flow. This interaction causes formation of large scale vortices in the shear layer separating free stream and separation bubble [16]. Strong flow perturbations provoke the momentum exchange between main flow and the separation bubble and lead to flow re-attachment. Later, experimental results [21] prove that nanosecond SDBD plasma performs as an active trip at pre-stall angles of attack and provides high amplitude perturbations that manipulate flow instabilities and generate coherent spanwise vortices at post-stall angles. These coherent structures entrain freestream momentum thereby reattaching the normally separated flow to the suction surface of the airfoil. Numerical modeling of SDBD development also shows fast formation of plasma layer and shock wave generation [22,42].

Perturbations initiation in shear layer

The process of nanosecond pulsed plasma layer interaction with the flow, formation of perturbations and vortices, and flow re-attachment was investigated in detail in [19]. A model of NACA 63-618 airfoil with the chord of 20 cm and span of 40 cm with the actuator applied was used for experiments. Several different actuators were used, including single, double and triple actuator configurations. The flow speed was 30 m/s. Some results are shown in Figure 37. The shock wave generated by actuators can be clearly seen, as well as large scale vortex structure as it developed 40 microseconds after the discharge [19]. It was observed that after 2-3 discharges the flow pattern changed completely. Flow reattached, separation zone shifted downstream. It was found that placing second actuator into the point to where separation was shifted by the first actuator, shifts the separation further downstream. This allows to achieve attached flow up to AoA = 32^0, using three pairs of the actuators. Summary energy consumption was less than 1 W for 40×20 cm airfoil in 30 m/s flow. Thus typical system reaction time is 10-15 ms and was close to the time of the vortex propagation along the surface of the airfoil (Figure 37). From Figure 37 it is clear that perturbation generated by pulsed actuator initiates instability in the shear

layer. This instability propagates along the shear layer; additional mixing brings additional momentum into boundary layer from the main stream and attaches the flow. It should be noted that the discharge energy plays a secondary role: two different regimes (repetitive pulse mode and burst mode) demonstrated in the columns 1 and 2, correspondingly, demonstrate almost the same dynamics of flow attachment while the discharge energy in the second case is 10 times bigger. This means that a high rate of energy release from discharge to translational degrees of freedom of gas is needed. Fast transition (in time scale shorter than gas-dynamic time in plasma layer) means the efficient generation of the shock wave and efficient excitation of perturbations in the flow [19]. That is why the dynamics of energy transfer from electric field to gas translational degrees of freedom in nonequilibrium plasma is one of the most critical issues for pulsed SDBD actuators.

As it was indicated above, the main mechanism of pulsed nanosecond SDBD effect on the flow is an extremely fast gas heating. Energy release in the gas is sometimes considered to be $Q=V\times I\times\Delta\tau$, whereas gas heating is defined by $\Delta T = Q/C_p$. Such an estimate includes some strong assumptions. The electric field energy is supposed to be completely absorbed by gas. This is not always true in the case of strong electric fields, since part of the energy is lost in radiation processes. In the case of high-current discharges at low electric fields, some energy will be lost in the near-electrode regions. In this case, part of the energy goes to heat the electrodes. Thus, the current multiplied by voltage in the discharge gap gives only the upper estimation of energy release. Estimations of temperature changes in the discharge are still-stronger suppositions. The equation $\Delta T = Q/C_p$ is completely valid for the thermal equilibrium state when internal degrees of freedom of the gas are in equilibrium with the translational degrees of freedom. That is not the case under conditions of strongly nonequilibrium plasma of gas discharge. On the other hand, using specific heat under constant pressure C_p presumes that energy release occurs at times noticeably higher than gasdynamics times. In this case, it is quite reasonable to use the supposition $P = const$. So, when analyzing the thermal mechanism of plasma actuator impact on the flow, it is necessary to take into account not only radiation energy loss, wall heating, etc., but also the rate of energy relaxation as compared to the typical times of plasma layer expansion (see, for example, [7,8,28]).

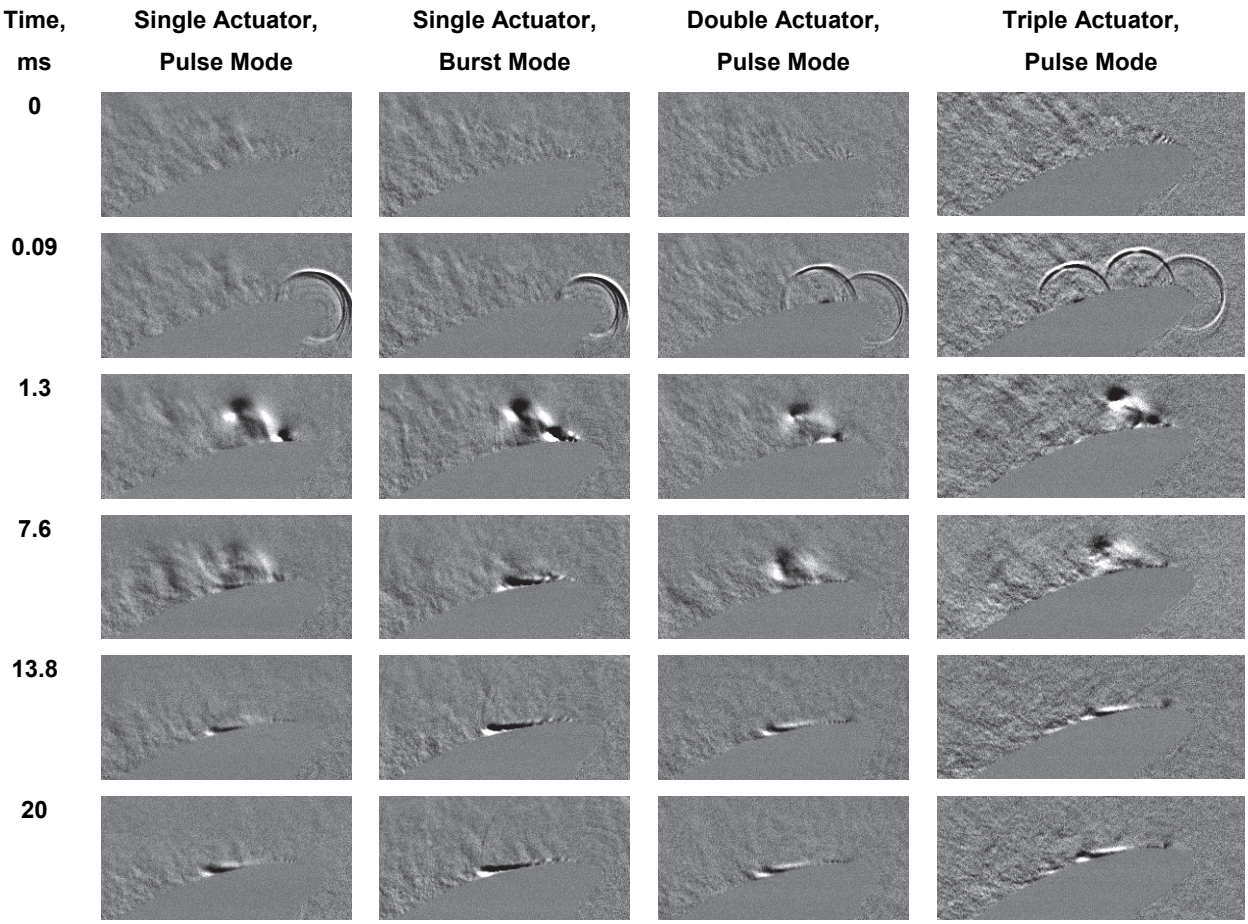

Figure 37. Dynamics of boundary layer re-attachment. V = 30 m/s, AoA = 26^0, NACA 63-618 airfoil, chord length was 20 cm wing span was 40 cm. Discharge energy 5 mJ/pulse, discharge frequency 200 Hz in pulse and burst modes; 10 pulses per burst; $d\tau = 100$ μs [19].

Mechanism of fast gas heating in the discharge

Thermal energy transfer to the flow from an electric discharge is a rather complicated multistep process [8,9], which is strongly dependent on the average energy of the electrons. Because they possess small masses and have long mean free paths, the electrons are the primary particle to gain energy from the electric field. Once background gas ionization is formed, electrons are accelerated by the electric field and their density increases by avalanche ionization of surrounding neutral molecules. In weakly ionized plasmas such as those considered here, the average electron energy is determined by the ratio of the electric field to the density of neutrals

(equivalent to the average energy gained between collisions). The slow rate of energy exchange of electrons with neutral gas results in a significant deviation of the mean electron energy from the energy of translational degrees of freedom of molecules. Depending on the value of the applied electric field, the mean electron energy in the discharge can reach several electron-volts (tens of thousands Kelvin) while the gas remains close to room temperature. Because of this high energy, the electrons couple most efficiently with highly energetic internal degrees of freedom of molecules, as well as their dissociation and ionization by electron impact. At the same time, the direct coupling of electron energy flux into translational and fast-thermalizing rotational degrees of freedom is relatively low.

Consequently, the energy release by vibration-translation (VT) relaxation, recombination of neutral and charged components and quenching of electronically excited molecules are the main mechanisms of gas temperature increase in nonequilibrium plasma. VT relaxation and atom-atom recombination are rather slow and can last tens of microseconds or longer even at atmospheric pressure, which is comparable with the typical gas dynamic times within a scale of several millimeters. Energy release during excitation of electronically excited states and molecular dissociation and ionization by electron impact is a much faster process. For instance, a molecule being excited by electron impact to a repulsive state dissociates to products with high translational energy [43, 44]. The rate of thermalization of such "hot" atoms and radicals usually reaches units of nanoseconds. Quenching of electronically excited molecules and electron-ion and ion-ion recombination proceed at the same time scale. Such a heating mechanism can become a governing process and produce fast gas heating in the discharge region under high values of reduced electric field E/n (close to or higher than the breakdown threshold) [8,9]. In this work the utility of fast heating for the addition of heat in time intervals shorter than acoustic propagation times was explored, allowing the formation of controlled shocks that can be shaped by the surface plasma array configuration and timed to interact with the near field flow such that they lead to separation control and to other control possibilities, including the control of acoustics and transition to turbulence.

Pulsed nanosecond discharges at high overvoltage were used for energy deposition into the flow [8,9]. It has been shown that up to 50-60% of total energy can be transferred to translational

degrees of freedom of the gas in hundreds of nanoseconds through mechanisms of fast plasma thermalization. Thus the approach allows us to overheat the gas layer almost instantaneously with simultaneous flow acceleration. The energy deposition can vary over a very wide range from several tens of K to several hundred K. This excitation guarantees a minimal energy consumption with maximal control because the effective region of energy deposition in the case of pulsed excitation is larger than in AC-discharge case and energy distribution control is more flexible. Smaller power consumption elongates the electrodes and dielectric surface life time. The energy efficiency of the nanosecond Dielectric Barrier Discharge (ns-DBD) plasma actuator was analysed in [45]. The independent measurements of the energy of electrical pulses and the useful part of the energy which heats up the gas in the discharge region were made. A characterization of the relative efficiency of ns-SDBD with different dielectric barrier thickness was performed. It was found to be an inverse proportionality between the thickness of the dielectric barrier and the energy deposition (the thicker the barrier, the lower the efficiency). The experiments [45] demonstrated that high value of electric field in the plasma region and the high dielectric permittivity of the dielectric layer lead to the increase of the efficiency of the actuator.

Static and dynamic stall control

A low turbulence subsonic wind tunnel has been retrofitted for electrical discharge experiments. The Subsonic Variable Speed Plasma wind tunnel with high voltage pulser and timer system can be seen in Figure 38. The tunnel has a cross-section of 250 mm x 360 mm and has generous optical access. The wind tunnel is equipped with 4 screens flow silencer and the intake diffuser has 1:16 contraction ratio, which allows it to achieve a low-turbulence flat flow field in the working section. The schematics and instrumentation for the Subsonic Variable Speed Plasma (SVSP) Wind Tunnel are shown in Figure 39.

Depending on the motor’s blades angle are able to change the flow Mach number from deeply subsonic to high-speed regime. Maximal speed is 180 m/s for small chord models; 100 m/s for large models.

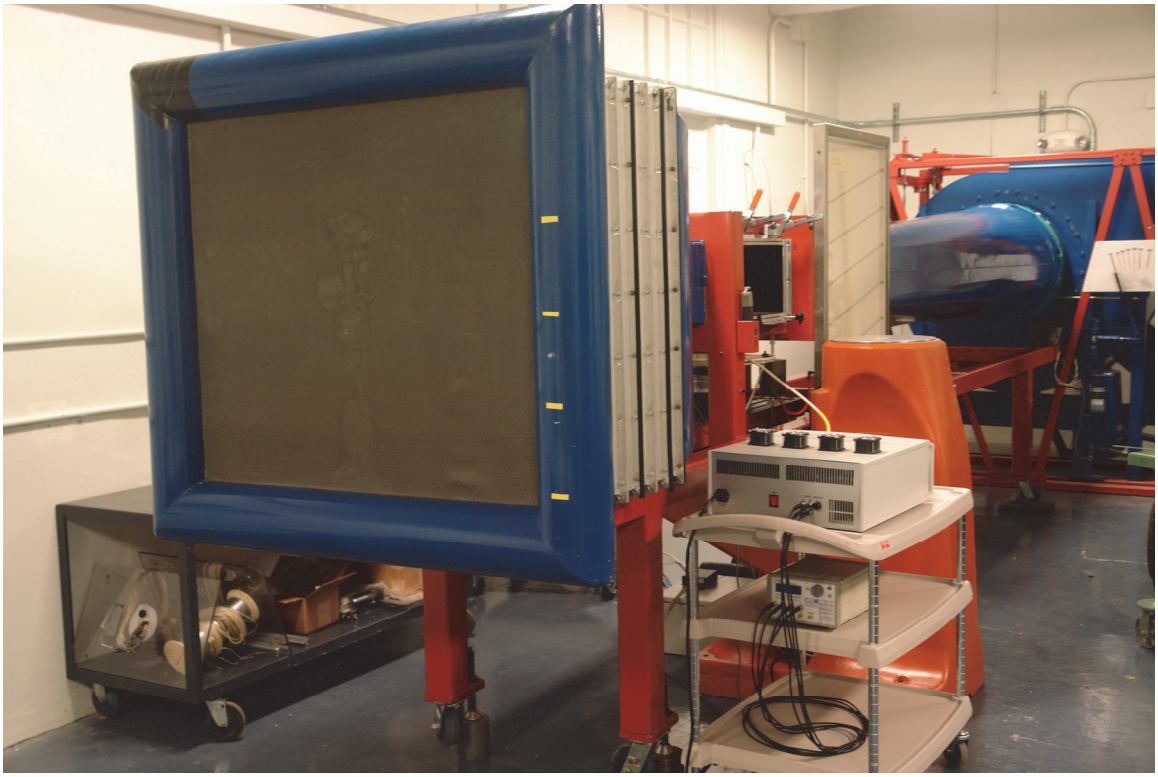

Figure 38. Subsonic Variable Speed Plasma (SVSP) blow-down wind tunnel.

The experimental test section has been replaced with a Plexiglas one to avoid electrical sparks between electrodes and conductive walls. The new test section has 1" dielectric walls and can operate with pulsed NS, PS or combined voltage up to 200 kV.

A new pitching mechanism consists of a direct drive servomotor, equipped with 6-component bridge sensor system. The servomotor is controlled by National Instruments cRIO system together with all other elements of the experiment – including high-voltage generators and wind tunnel velocity. This system allows complete synchronization of all events: pitching angle, free stream speed, actuator's timing, and all 6-component forces measurements using ATI-IA DAQ F/T transducers with variable calibrations. The calibration range is from 32 to 660 N full-scale for forces and from 2.5 to 60 Nm for torque. The direct drive servomotor by Kollmorgen has a peak torque of 160 Nm and maximal speed of 250 rpm (Figure 39). Direct control through EtherCAT NI interface from cRIO control module is utilizing LabView SoftMotion feature, which allows programming of all types of periodical motions – including non-harmonic modes.

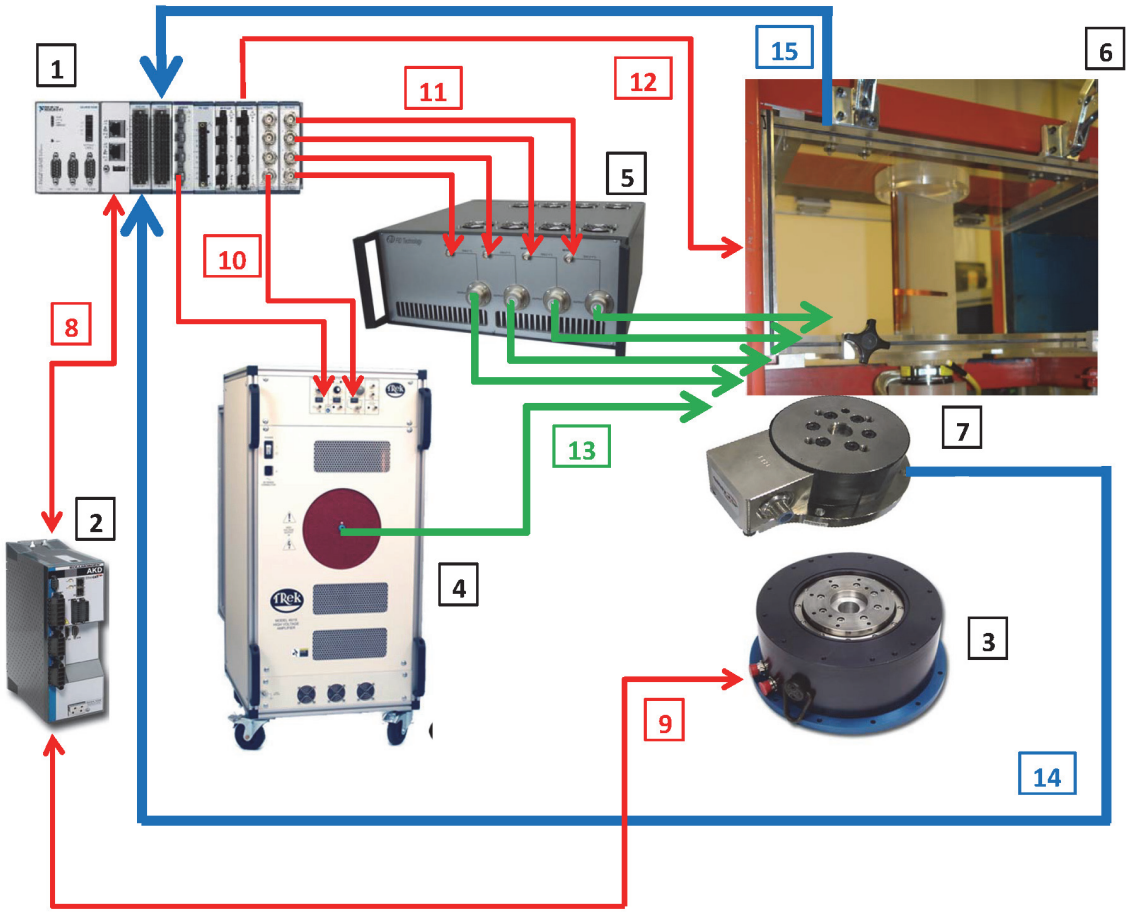

Figure 39. Subsonic Variable Speed Plasma (SVSP) Wind Tunnel schematics and instrumentation. 1 – NI cRIO 9068 control module, including programmable voltage and current sources; 32-ch differential 16-bit analog input modules; 8-ch TTL input/output modules; EtherCAT interface for servomotor control. 2 – servomotor drive. 3 – direct drive Kollmorgen servomotor. 4 – TREK high-voltage amplifier for bias/AC supply. 5 – FID 4-ch pulser. Maximal voltage 36 kV, frequency 20 kHz, pulse duration 15 ns, interchannel jitter less than 100 ps. 6 – wind tunnel. Maximal speed is 180 m/s for small chord models; 100 m/s for large models. 4 screens; 1:16 contraction ratio. 250×360 mm^2 cross-section. 7 – ATI-IA DAQ F/T 6-component transducer. 8 – EtherCAT interface. 9 – servomotor interface. 10 – amplifier control. 11 – FID pulser synchronization. 12 – dynamic control of wind tunnel speed. 13 – high-voltage lines to actuators. 14 – DAQ transducer cable. 15 – Pitot tube and hot wire sensors free-stream velocity data.

The wind tunnel, blade pitching system, plasma generators and control system are completely controlled by computers. The main control computer (Intel Core i7 4770S (3.10GHz) 8GB DDR3 2TB HDD) is running NI LabView program which controls the NI cRIO 9068 real-time

control module, including programmable voltage and current sources; 32-ch differential 16-bit analog input modules; 8-ch TTL input/output modules through Ethernet cable.

NI cRIO 9068 real-time control module controls through EtherCAT interface the direct drive servomotor; TREK high-voltage amplifier for bias/AC supply; FID 4-channel pulser; provided 16-bit analog data acquisition for ATI-IA DAQ F/T 6-component transducer; and controls the wind tunnel speed using electromechanical actuator for motor's blades position and dynamics speed measurements using Pitot tube and hot wire sensors free-stream velocity data.

Figure 40 shows the model airfoil NACA-0015 used in the experiments. The airfoil has 6 inch chord and 10 inch span. A single SDBD plasma actuator was centered on the leading edge with 0.3 mm of PVC dielectric separation. The covered electrode is 50 mm wide and allows relatively long plasma layer formation.

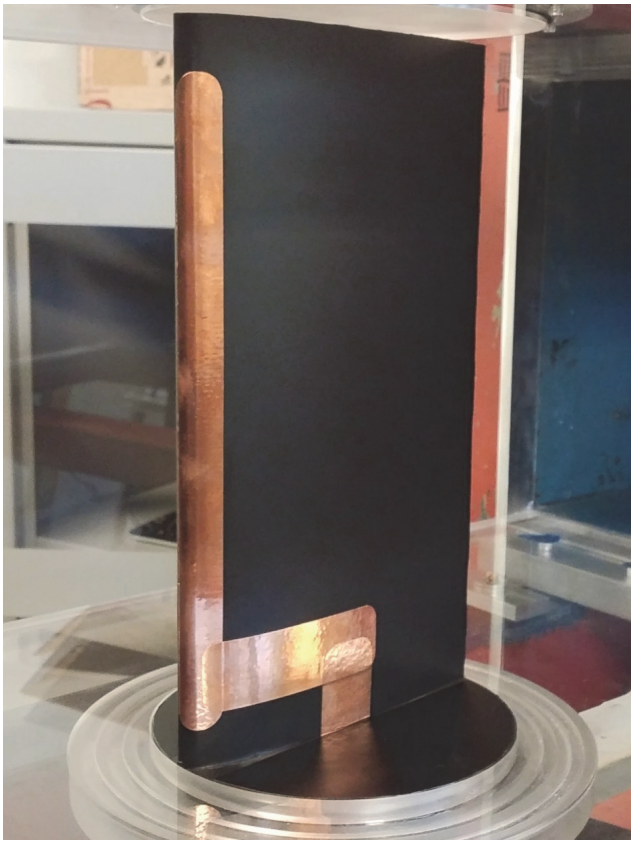

Figure 40. Model NACA 0015 Airfoil 6 inch chord 10 inch span Single DBD plasma actuator centered on the leading edge with 0.45 mm of PVC dielectric separation.

Static stall control

Preliminary results of the lift force measurements by ATI-IA DAQ F/T transducer give the lift force dynamics for flow speed U = 50, 70 and 100 mph. Above AoA=12^0 measurements show a significant lift force decrease because of the flow separation. The SDBD actuators operate in a burst mode. The train consists of 10 pulses with the time interval between pulses in the train dt = 1/f ~ 6.7 ms. The SDBD discharge attaches the flow in less than 10 ms for all tested angles of attack above the critical one. When the burst ends, the flow rapidly detaches for AoA bigger than 16^0 and remains attached in the interval 12-16^0. This observation indicates a delayed flow detachment for smaller AoA and allows to reduce the discharge energy.

The difference between lift forces with and without actuation for different angles of attack reaches the value of 2. It should be noted than the C_L in regimes with actuation are higher than maximal value for C_L without actuation. It means the possibility of the blade lift force increase using higher angles of attack.

The same strong effect was observed for free stream velocity U = 100 mph with almost 2-times lift force increase. Typical time of the lift force increase is a bit shorter than the same time for U = 70 mph and could be estimated as dt ~ 4-5 ms. This acceleration of the transition to the attached flow regime correlates with the increase of the main flow speed.

Thus, the wind tunnel tests of DBD plasma actuation U = 50-100 mph show a significant lift force increase because of actuation. Critical angle of attack increase (from 12 to 25 degrees) is observed at discharge power ~5W/m for static stall conditions. Response time less than 10ms is shown for U = 70 mph and less than 5 ms for U = 100 mph. This fast system response demonstrates the possibility of using NS-SDBD for dynamic stall control.

Results of the lift force measurements by ATI-IA DAQ F/T transducer are shown in the Figure 41. Figure 41,a shows the lift force dynamics for flow speed U = 70 mph. Above AoA=12^0 measurements show a significant lift force decrease. The discharge operates in a burst mode. The first pulse in a train corresponds to t = 0. The train consists of 10 pulses with the time interval between pulses in the train dt = 1/f = 6.7 ms. The SDBD discharge attaches the flow in less than

10 ms (Figure 41,a) for all tested angles of attack. When the burst ends, the flow rapidly detaches for AoA bigger than 16^0 and remains attached in the interval 12-16^0. This observation indicates a delayed flow detachment for smaller AoA and allows to reduce the discharge energy.

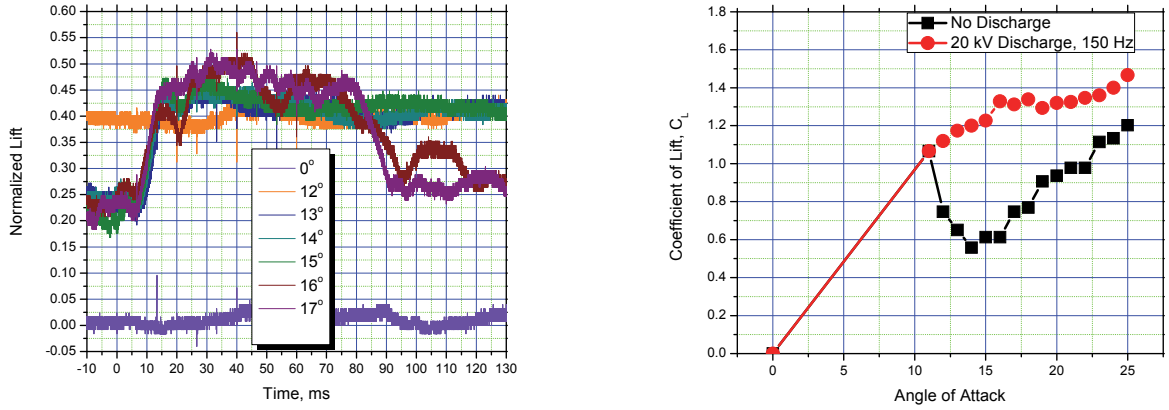

Figure 41. Left. Lift Generated as a function of time. Right. Lift Coefficient as a function of AoA. P_{plasma} = 2 W, f = 150 Hz, E = 15 mJ. U = 70 mph, NACA0015 airfoil.

Figure 41,b demonstrates the difference between lift forces with and without actuation for different angles of attack. It should be noted than the C_L in regimes with actuation is higher than maximal value for C_L without actuation. It means the possibility of the blade lift force increase using higher angles of attack. The same strong effect was observed for free stream velocity U = 100 mph with almost 2-times lift force increase. Typical time of the lift force increase is a bit shorter than the same time for U = 70 mph and could be estimated as dt ~ 4-5 ms. This acceleration of the transition to the attached flow regime correlates with the increase of the main flow speed.

Thus, the wind tunnel tests of DBD plasma actuation U = 50-100 mph show a significant lift force increase because of actuation. Critical angle of attack increase (from 12 to 25 degrees) is observed at discharge power ~5W/m for static stall conditions. Response time less than 10 ms is shown for U = 70 mph and less than 5 ms for U = 100 mph. This fast system response demonstrates the possibility of using NS-SDBD for dynamic stall control.

Dynamics of flow reattachment

Figure 42 shows the influence of number of pulses in the train on the flow attachment dynamics for angle of attack 16^0. The lift force increases during 12 ms in all cases, including a single-shot regime. This time corresponds to the perturbation propagation from the leading edge of the airfoil to the trailing edge and back. After flow attachment the new flow pattern exists for a relatively long time. In a single-shot regime the flow detaches in ~30 ms, while even for a train of two pulses the new pattern exists for 0.1-0.2 sec. The difference demonstrates that in the case of a single pulse there is incomplete flow attachment. All other regimes for AoA = 16^0 show complete flow attachment and slow detachment when actuation stops (Figure 42).

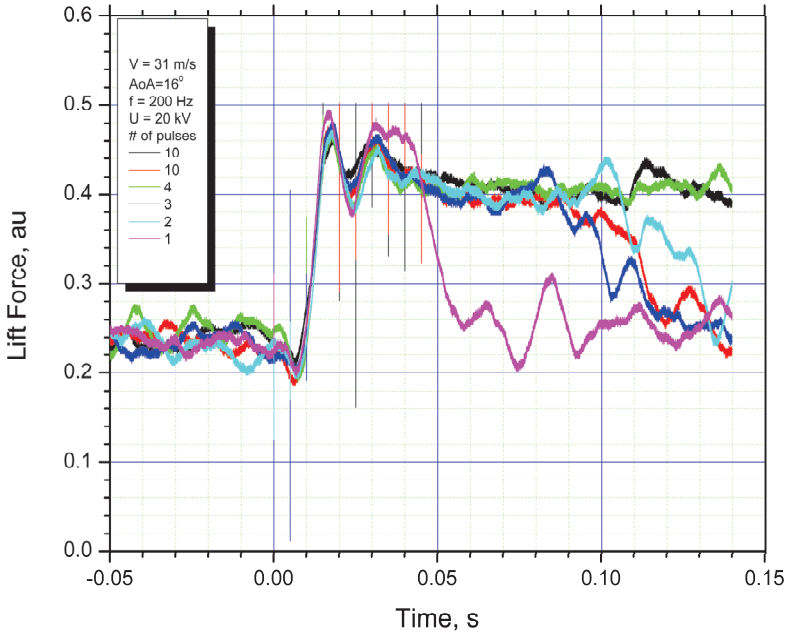

Figure 42. Influence of number of pulses on the flow attachment dynamics. AoA = 16^0.

Figures 43,44 show the influence of number of pulses in the train on the flow attachment dynamics for angle of attack AoA = 20^0 and 26^0. When the angle of attack increases the flow detaches faster. At AoA = 26^0 flow detaches almost immediately after the actuation stops. Thus, at high angle of attack there is no delay between the end of the actuation and flow separation.

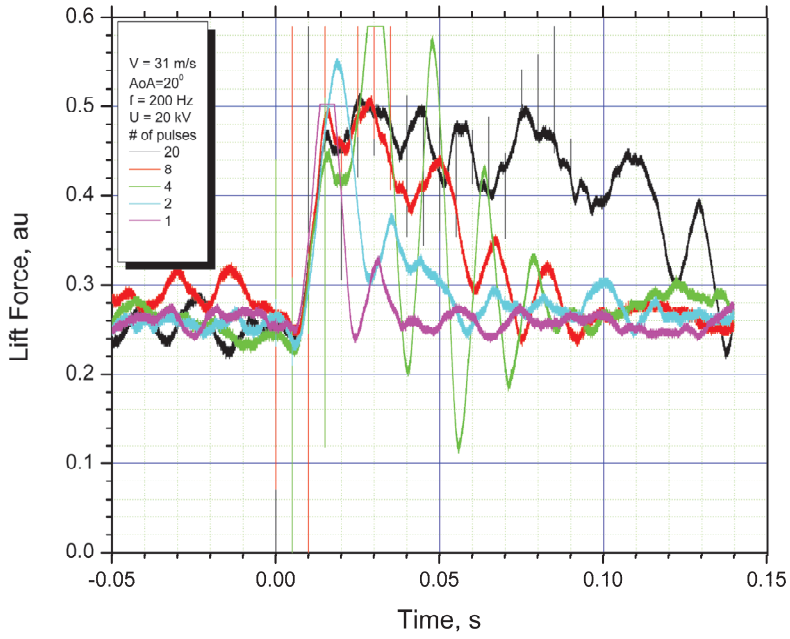

Figure 43. Influence of number of pulses on the flow attachment dynamics. AoA = 20^0.

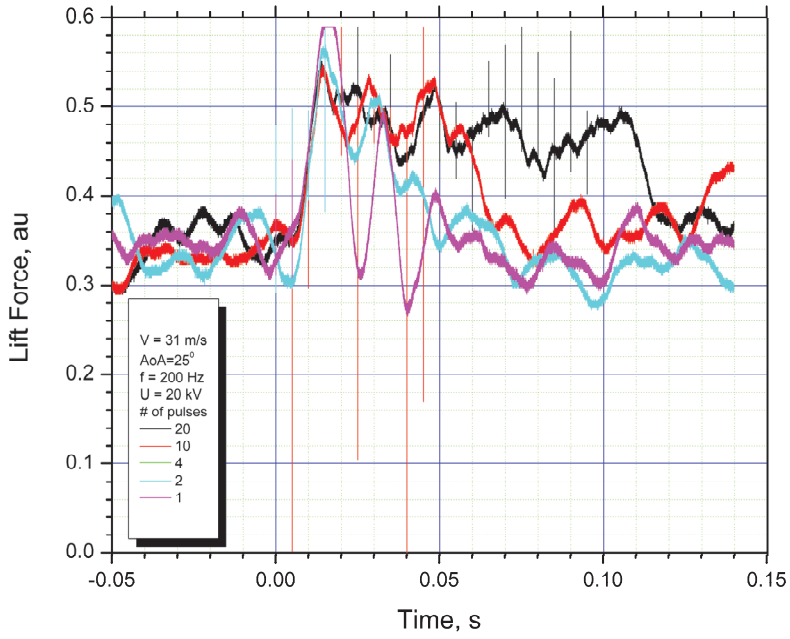

Figure 44. Influence of number of pulses on the flow attachment dynamics. AoA = 26^0.

Dynamic stall control

Figure 45 shows the dynamics of the lift force over the pitching cycle for maximal angle of attack $AoA_{max} = 24^0$. The blade changes the AoA from 0 to 24^0 and back to zero in 300 ms in a sinusoidal motion. When the blade reaches a critical angle (AoA ~ 12^0), the flow detaches and the lift force drops down (Figure 45). Lift force decreases until the AoA drops down to 12^0 again. At this point the flow starts a re-attachment and lift force increases.

There are several different regimes of dynamic stall. When AoA_{max} is smaller than a critical angle of attack, no separation was observed and the lift force increases with AoA increase. When AoA_{max} is higher than the critical value, a significant flow separation and a lift force decrease are observed. The AoA_{max} increase leads to a faster increase in a lift force and a stronger lift force drop when critical AoA is reached.

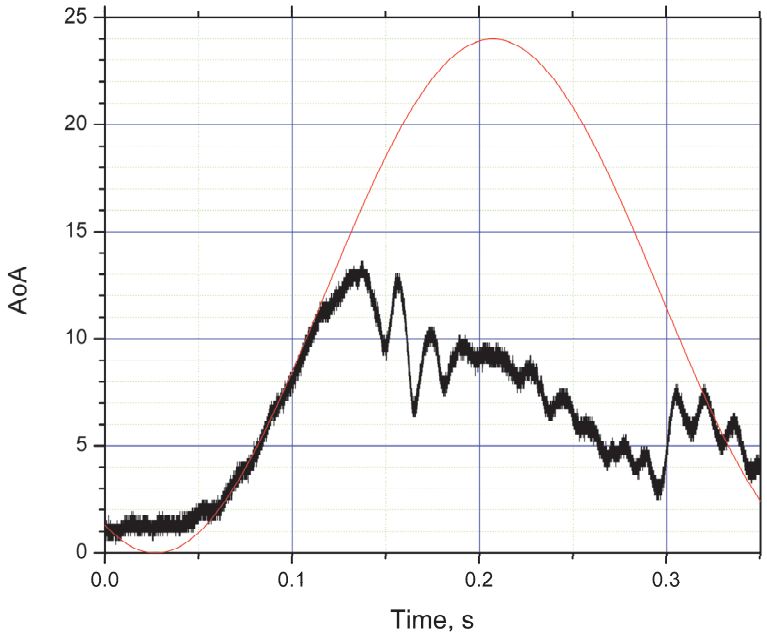

Figure 45. Dynamics of the lift force over the pitching cycle. $AoA_{max} = 24^0$. V = 31 m/s.

The flow actuation with a discharge period of 6 ms prevents the lift force decrease (Figure 46). The black curve shows the lift force dynamics without actuation. When AoA reaches 12^0, the

flow separates and the lift force decreases by 40%. When actuation is on, the lift force does not decrease at all and allows a smooth operation of the pitching airfoil.

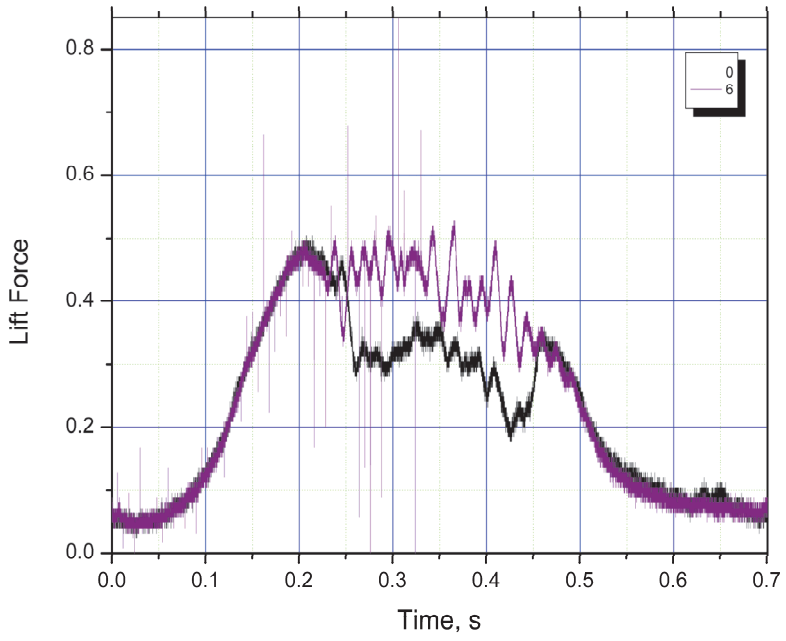

Figure 46. Dynamics of the lift force over the pitching cycle. $AoA_{max} = 26^0$. V = 31 m/s. Actuation period t = 6 ms.

Normal Flow Configuration

Figure 43 shows the the influence of number of pulses in the train on the flow attachment dynamics for angle of attack AoA = 20^0. When the angle of attack increase the flow detaches faster. At AoA = 20^0 flow detaches almost immediately after the actuation stop. Thus, at high angle of attack there is no delay between the end of the actuation and flow separation.

Figure 47 shows the dynamics of the lift force over the pitching cycle for maximal angle of attack $AoA_{max} = 28^0$. The blade changes the AoA from 0 to 28^0 and back to zero in 600 ms. When the blade reaches a critical angle (AoA ~ 12^0), the flow detaches and the lift force drops down (Figure 47). Lift force decreases until the AoA drops down to 12^0 again. At this point the flow starts a re-attachment and lift force increases.

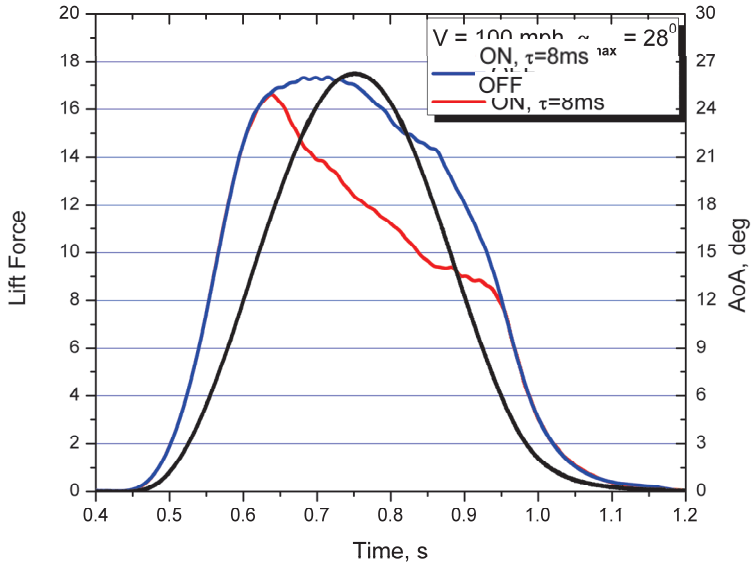

Figure 47. Dynamics of the lift force over the pitching cycle. $AoA_{max} = 28^0$. V = 45 m/s. Actuation period τ = 8 ms.

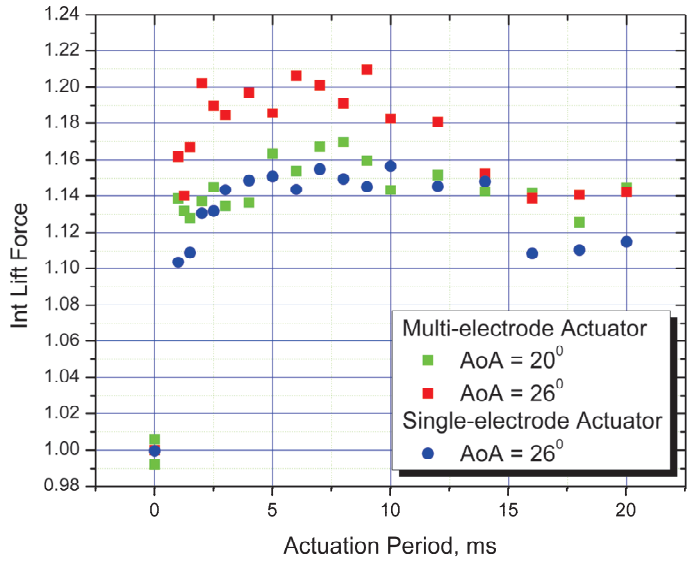

Figure 48. Integral of the lift force over the pitching cycle for single-electrode and multi-electrode configurations. V = 31 m/s.

Figure 48 demonstrates the lift force integral over the pitching cycle for two different electrode geometries. Single-electrode geometry corresponds to the initial configuration with a single discharge located at the leading edge of the airfoil. Multi-electrode configuration utilizes the same electrode on the leading edge of the airfoil with 4 additional electrodes equally distributed along the upper surface of the airfoil. The multi-electrode configuration was designed to enhance the authority of the plasma actuator due to the multiple vortices production during the separation development. It is clear from the Figure 48 that the multi-electrode actuation allows additional lift force increase in comparison to the case of the single-electrode actuator. In a multi-electrode configuration the airfoil at AoA= 20^0 demonstrates the same lift force increase as the airfoil with a single-electrode actuator at AoA =26^0 (Figure 48).

Reverse Flow Configuration

Figure 49 shows the results of the lift force measurements over the pitching cycle for reverse flow configuration. In this case the flow propagates from the sharp trailing edge of the airfoil and the flow separation is stronger than in the case of normal flow configuration.

Figure 49,a demonstrates the lift force change for a slow pitching motion. In this case the reduced frequency is very small and there is a static stall regime. Plasma actuator is ON over the first half of pitching cycle. The figure shows the possibility of a static stall control in a reverse flow configuration and its dependence on the actuation frequency. When the actuator is OFF, the lift force almost immediately drops down to the reference value without actuation.

Figures 49b-49d demonstrate the dynamic stall control in the reverse flow configuration. When AoA_{max} is not very large (Figure 49b) the actuation reattaches the flow completely. At a high AoA (Figures 49c and 49d) there is partial flow reattachment with almost two-times lift force increase (Figure 49c).

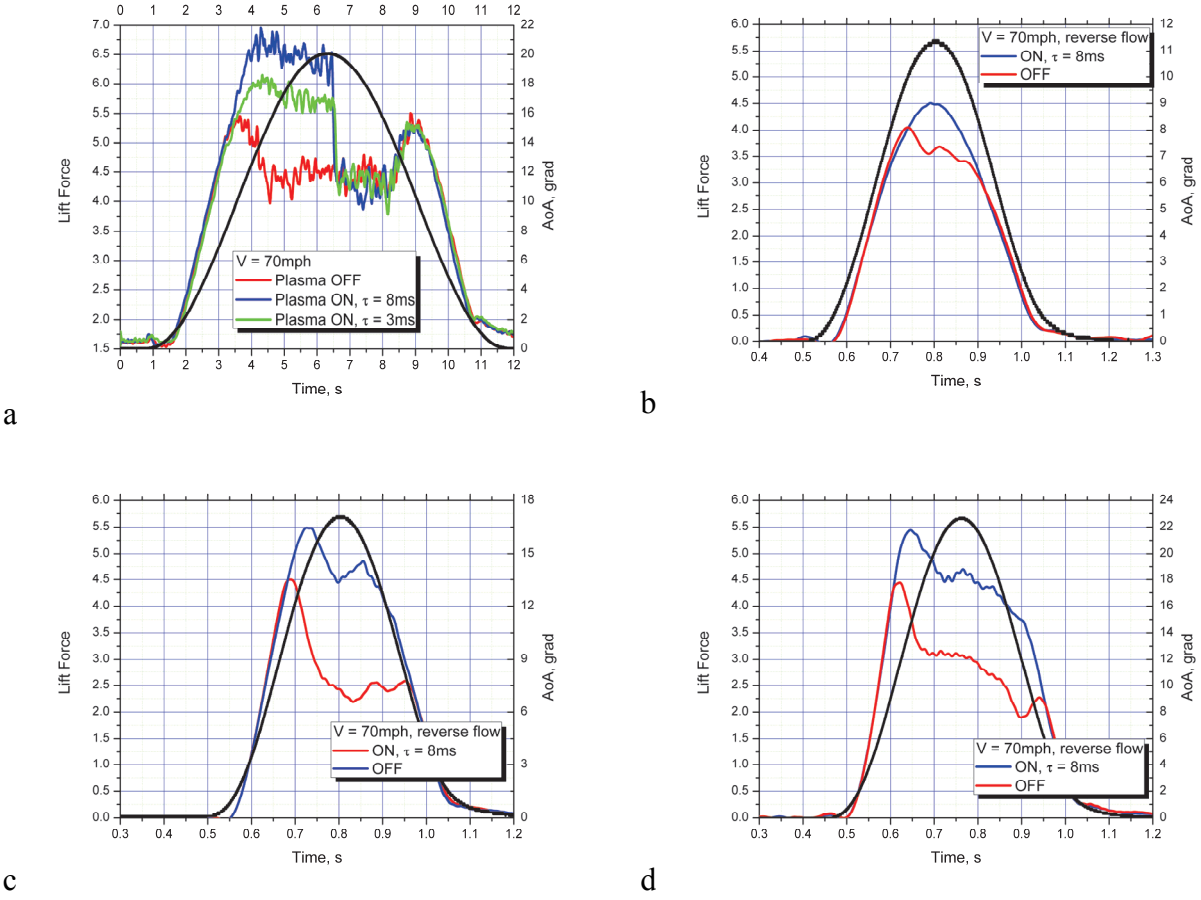

Figure 49. Dynamics of the lift force over the pitching cycle. Reverse Flow. Flow speed 31 m/s. a) Slow pitching – static stall control. Plasma actuator is ON over the first half of pitching cycle; b) Fast pitching – dynamic stall control. $AoA_{max} = 11.5^0$; c) $AoA_{max} = 17^0$; d) $AoA_{max} = 23^0$.

Integral of the lift and drag force over the pitching cycle for reverse flow configuration is shown in the Figure 50. NS SDBD actuation with a discharge frequency of f ~ 110 Hz allows an integral lift force increase up to 1.4 times (Figure 50,a), with almost the same drag force (Figure 50,b).

Five free stream velocities were tested in the reverse configuration: U_∞ = 40mph, 70mph, 100mph, 120mph, and 150mph (Figure 49-50). Similar trends are observed for the pitching dynamics as with the normal flow configuration. These trends include the linearity of lift force increase until separation occurs, then an unsteady period of boundary layer separation above the

critical angle of attack, and a hysteresis between the separation angle and reconnection angle. It should be noted these flows are all quasi-steady, with reduced frequencies $k \leq 0.05$. Integral lift over a single pitching period increases near-monotonically with plasma actuation. Increases in lift are observed to be as large as 55%, while changes in drag are typically below 10% in the stall regime.

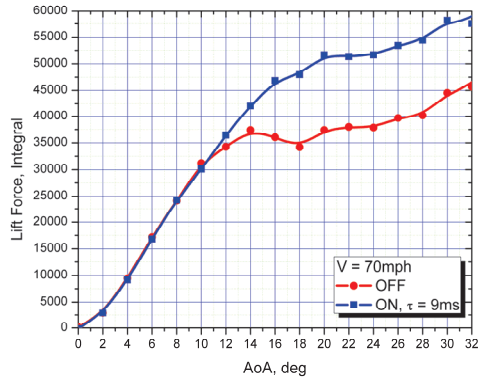

a

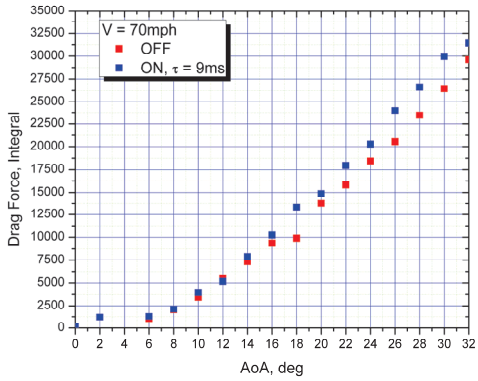

b

Figure 50. Integral of the lift (a) and drag (b) force over the pitching cycle for reverse flow configuration. V = 31 m/s. Actuation period τ = 9 ms.

Lift Force Increase in Hover Mode

The main difference between the results of this chapter and previous studies is the use of rotating blades, which introduces a longitudinal component of the flow velocity along the blade. Rotation of the blades also leads to a large difference in flow velocity near the root of the blade and near its tip, which makes it difficult to optimize the frequency of the actuator. The work also used a constant power drive to rotate the rotor – that is, the total effect of the actuator was composed of both an increase in the lift force coefficient when the flow was attached, and a change in the drag force coefficient, which led to a change in the rotational speed of the blades. Thus, the experiment was as close as possible to the operating conditions of the real helicopter rotor in the hover mode.

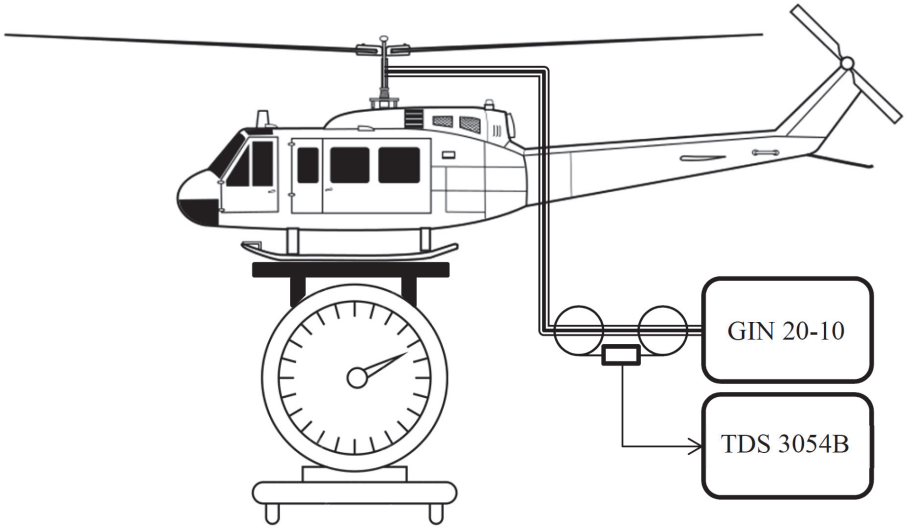

Figure 51. Helicopter model on the scale.

For the experiment, a standard radio-controlled helicopter model was used. The model had 1860-mm blade span and was powered by 4.5 kW electrical motor (Figure 51). The model was additionally equipped with an electrical system which allows delivering NS high-voltage pulses from the pulser to rotating blades. The pulses had amplitude of 20 kV and frequency from 200 Hz to 2 kHz. The asymmetric plasma actuators were flash-mounted on the leading edge of the blades.

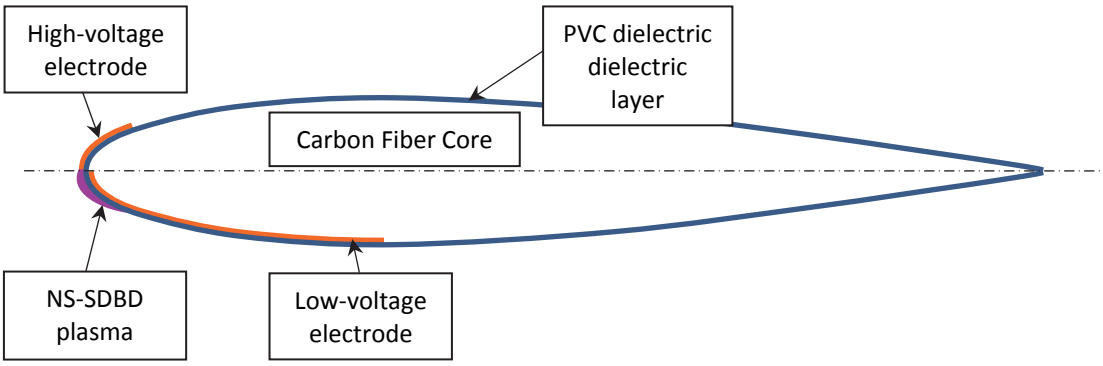

Figure 52. Blade shape and configuration of the electrodes. Chord length was 60 mm.

Figure 52 demonstrates the electrodes location on the surface of the blades. The PVC dielectric layer had a thickness of 0.4 mm. The plasma was generated on the pressure side of the blade. At high angle of attack the perturbation propagated along the surface to the suction side. The shape of the high-voltage pulsed (incident and reflected) is shown in the Figure 53.

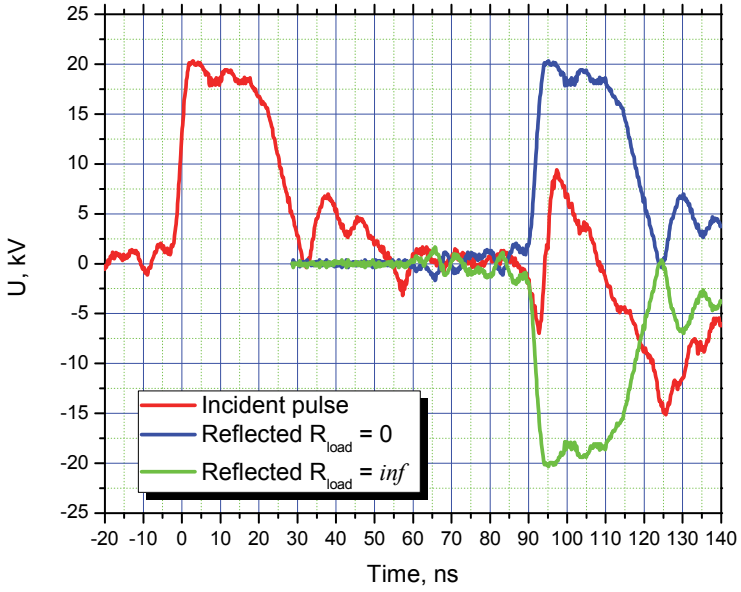

Figure 53. The shape of the high-voltage pulse. Pulser FID 20-10, external synchronization at 1 kHz.

Figure 54 shows the results of direct lift force measurements for the helicopter model for different actuation frequency. The helicopter motor power has been fixed at 30% of maximal to avoid the overheating. Blades rotated at frequency of ~ 18 Hz in all cases. The angle of attack was set to $\alpha = 20^0$, which exceeds the critical angle $\alpha_{crit} \sim 12^0$. A lift force up to 50% was observed when changing the actuation frequency from 300 to 2000 Hz (Figure 54). Almost linear increase of the lift force for the actuation frequency range 300-1500 Hz reflects the fact that different parts of the blades have different linear speed and an optimal actuation frequency increases with the distance from the rotor axis. The external parts of the blades generate more lift and the frequency increase leads to overall performance increase. It should be mentioned that

significant further optimization is possible using different actuation frequencies for different parts of the blades.

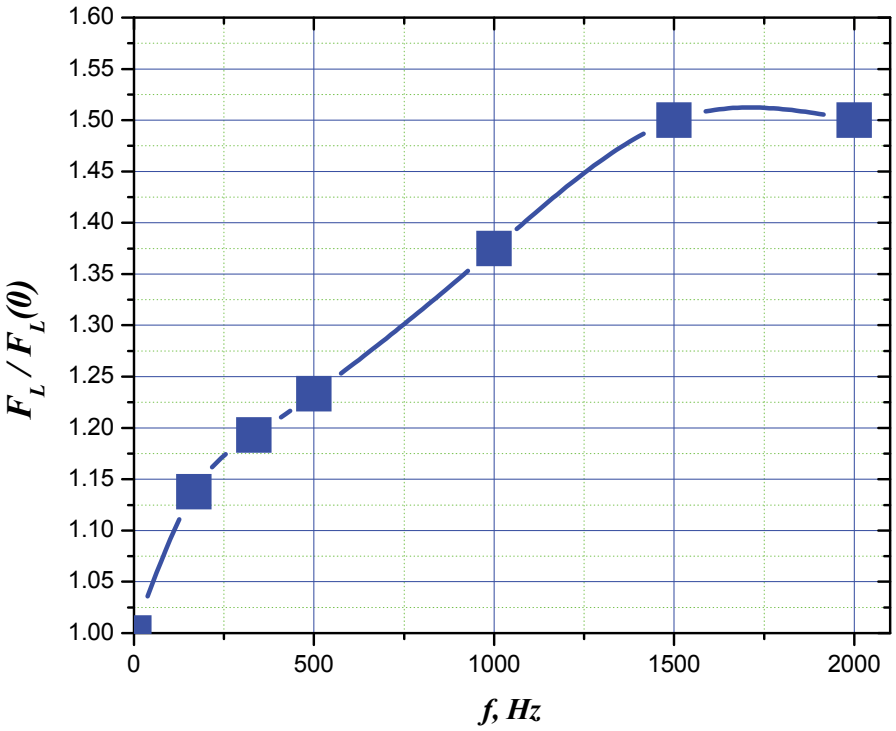

Figure 54. Lift force dependence on the actuation frequency. Angle of attack $\alpha=20^0$.

Figure 55 shows the results of the lift force measurements in the hover mode for different angles of attack in three cases: without actuation; actuation at f = 1 kHz; and actuation at f = 2 kHz. Without actuation the blades achieve the maximal lift force at $\alpha = 12^0$. Further increase of the angle of attack leads to the flow separation and the lift force decrease (Figure 55). When actuator is on, a significant lift force increase was observed at high angle of attack – up to 7% for actuation frequency of 1 kHz, and up to 20% for actuation frequency of 2 kHz. It means that the payload and/or extend the flight envelope of the helicopter can be significantly increased using plasma actuation.

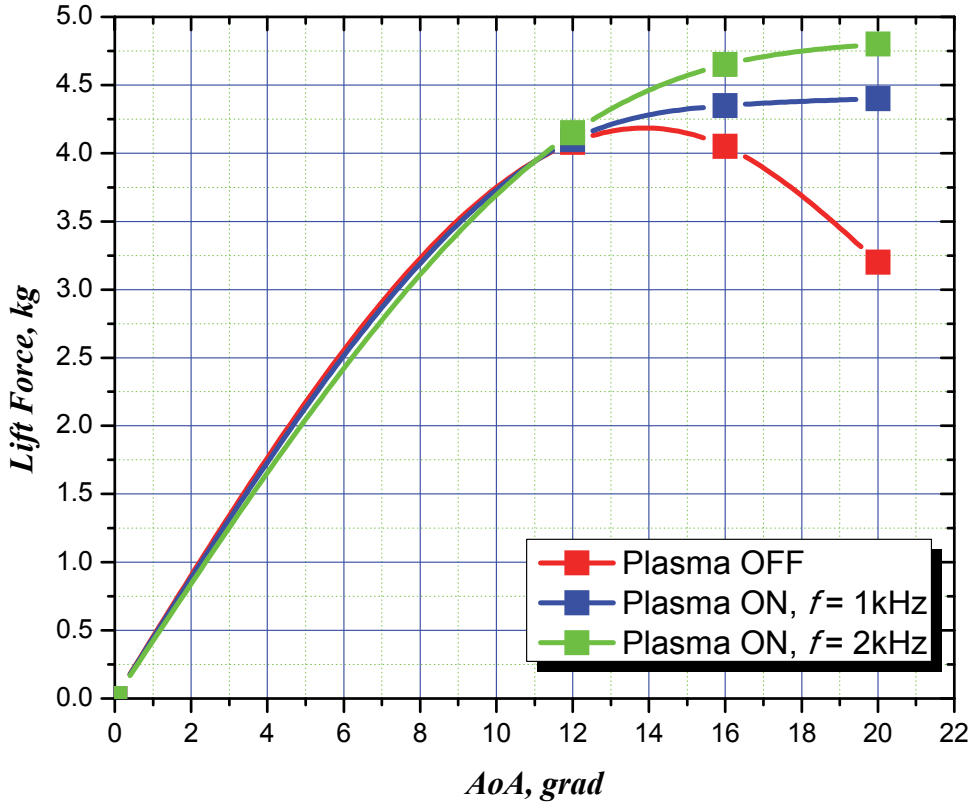

Figure 55. Lift force dependence on angle of attack.

Nanosecond pulsed SDBD plasma actuators show great potential to be able to address the problems associated with dynamic stall in rotorcraft, specifically RBS. The inherent benefits of plasma actuators, such as fast response times, high frequency bandwidth, and being an active control method, are important advantages over mechanical actuation methods. This study is the first demonstration of dynamic stall control for reversed flow over an airfoil, as well as demonstrates stall control at higher velocities than previously demonstrated. The lift force increase up to 20% in a hover mode is demonstrated for a fixed engine power.

Conclusions

We have reviewed the results of the experimental studies of a nanosecond SDBD in air for various pressures and voltages. In these studies, discharge propagation length, propagation velocity, plasma layer thickness and discharge energy characteristics were measured. For low rates of voltage pulses, the discharge properties were independent of the rate. In most cases the discharge plasma layer dimensions were almost inversely proportional to the gas pressure. The limiting length of the plasma layer and the thickness of the plasma layer were proportional to the pulse voltage. The propagation velocity of the discharge ionization front was inversely proportional to the square root of the pressure. The measured energy input and mean electric field in the center of the discharge zone decreased with increasing gas pressure. For negative voltage polarity, the corresponding reduced electric field was 1150 Td for 220 Torr and 800 Td at atmospheric pressure.

Ozone observations in the air SDBD plasma showed that the ozone concentration increases with increased gas pressure and decreased gas temperature. Ozone molecules are produced due to an O atom association with O_2 molecules in three-body reactions. Calculations showed that, at high, reduced electric fields measured in SDBD plasmas, the dominant channels of O atom production are (i) electron-impact dissociation of O_2, (ii) electron-impact excitation of N_2 followed by dissociative quenching in collisions with O_2 and (iii) electron recombination with a positive oxygen ion. We obtained agreement between measured and calculated ozone concentrations assuming anomalously high electric fields in the discharge plasma and assuming the absence of O_2 dissociation in electron recombination with O_4^+ ions. The products of this recombination process are poorly understood. The assumption that only molecular products are formed in this case also allows an agreement to be reached between the calculated and experimentally estimated fractional electron power rapidly transferred into heat in the SDBP plasma at atmospheric pressure and in the decaying plasma produced by a pulsed high-voltage nanosecond discharge at low (20 Torr) pressures. However, this assumption is in contradiction with available interpretations of the measured ozone yield in the pulse radiolysis of gaseous oxygen at high dose radiation. Additional observations under well controlled conditions are required to determine branching ratios of recombination processes in oxygen and air plasmas. This information is of considerable significance for simulating rapid gas heating and ozone production in nanosecond SDBD plasmas produced at high, reduced electric fields.

New SiC diodes-based design is proposed to increase the induced jets velocity. The “pull-it-forward” concept of SDBD performance enhancement was developed and tested. Momentum generation by synchronized NS-SDBD is demonstrated. The “microblast” SDBD flow control technology was demonstrated using 4-electrode SDBD synchronization in microsecond time scale.

The inherent benefits of plasma actuators, such as fast response times, high frequency bandwidth, and being an active control method, are important advantages over mechanical actuation methods. This study is the first demonstration of dynamic stall control for reversed flow over an airfoil, as well as demonstrates stall control at higher velocities than previously demonstrated. Wind tunnel testing of SDBD plasma actuators at V = 50-150 mph were performed. Critical angle of attack increase (from 12 to 25 degrees) is observed at discharge power ~5 W/m for static and dynamic stall conditions. Fast response time was demonstrated. Dynamic stall control using NS SDBD has been demonstrated. It was shown that low-energy actuation could increase the integral lift force for more than 10% and prevent the abrupt lift force decrease when the blade reaches the critical value of the angle of attack. Dynamic stall control by NS SDBD plasma actuators has been shown for the first time for normal and reverse flow configuration. Lift force increase up to 40% is shown for both cases for maximal angle of attack up to 32^0 for flow speed 20-70 m/s. The lift force increase up to 20% in a hover mode is demonstrated for a fixed engine power.

Acknowledgments

This work was supported by the Army Research Office (ARO) Grant W911NF-15-1-0236 "Control of Static and Dynamic Stall in a Wide Range of Mach Numbers by Plasma Actuators with Combined Energy/Momentum Action" under Grant Officer Representative Dr. Matthew J. Munson.

References

1. Bletzinger P., Ganguly B.N., VanWie D., and Garscadden A. Plasmas in high speed aerodynamics. J. Phys. D: Appl. Phys. 38 (2005) R33-R57
2. Moreau E. Airflow control by non-thermal plasma actuators. J. Phys. D: Appl. Phys. 40 (2007) 605-636
3. Nikipelov A., Nudnova M., Roupassov D., Starikovskiy A. Acoustic Noise and Flow Separation Control by Plasma Actuator. AIAA-2009-695. 47th AIAA Aerospace Sciences Meeting including The New Horizons Forum and Aerospace Exposition, Orlando, Florida, Jan. 5-8, 2009
4. Starikovskiy A., Aleksandrov N. *Plasma-assisted ignition and combustion.* Progress in Energy and Combustion Science 39 (2013) 61-110.
5. Starikovskii A., Anikin N., Kosarev I., Mintoussov E., Nudnova M., Rakitin A., Roupassov D., Starikovskaia S., Zhukov V., Nanosecond-Pulsed Discharges for Plasma-Assisted Combustion and Aerodynamics. Journal of Propulsion and Power 2008. 0748-4658 vol.24 no.6 (1182-1197)
6. Raizer Yu.P. Gas Discharge Physics. Berlin, Heidelberg, New York. Springer-Verlag. 1991.
7. Popov N.A. Investigation of the mechanism for rapid heating of nitrogen and air in gas discharges. Plasma Physics Reports.27, 866 (2001).
8. Aleksandrov N.L., Kindusheva S.V., Nudnova M.M. and Starikovskiy A.Yu. Mechanism of ultra-fast heating in a nonequilibrium weakly-ionized air discharge plasma in high electric fields. J. Phys. D: Appl. Phys. 43 (2010) 255201 (19pp)
9. Nudnova M.M, Kindysheva S.V, Aleksandrov N.L, Starikovskii A.Yu. Fast gas heating in N_2/O_2 mixtures under nanosecond surface dielectric barrier discharge: the effects of gas pressure and composition. Phil. Trans. R. Soc. A. 2015. 373 20140330.
10. Likhanskii A.V., Shneider M.N., Opaits D.F., Miles R.B., Macheret S.O. Limitations of the DBD effects on the external flow. 48th AIAA Aerospace Sciences Meeting Including the New Horizons Forum and Aerospace Exposition 4 - 7 January 2010, Orlando, Florida AIAA 2010-470.
11. Starikovskaia S.M., Anikin N.B., Pancheshnyi S.V., Starikovskii A.Yu. Time resolved emission spectroscopy and its applications to study of pulsed nanosecond high-voltage discharge. Proceedings of SPIE, 2002. V. 4460, pp. 63-73.
12. Opaits D.F., Roupassov D.V., Starikovskaia S.M., Starikovskii A.Yu., Zavialov I.N., Saddoughi S.G. Plasma Control of Boundary Layer Using Low-Temperature Non-equilibrium Plasma of Gas Discharge. 43-rd AIAA Aerospace Sciences Meeting and Exhibit, 2005. Reno, Nevada, USA, paper AIAA 2005-1180, 2005.
13. Loiseau J.F., Batina J., Noel F., and Peyrous R. Hydrodynamical simulation of the electric wind generated by successive streamers in a point-to-plane reactor. 2002. J. Phys.D: Appl. Phys. 35 1020-31

14. Zouzou N., Moreau E., and Touchard G. Precipitation electrostatiquedansune configuration pointe-plaque. 2006. J.Electrostat. 64 537-42
15. Rickard M., Dunn-Rankin D., Weinberg F., and Carleton F. Maximizing ion-driven gas flows. 2006. J. Electrostat. 64 368-76
16. Roupassov D., Nudnova M., Nikipelov A., Starikovskii A. Sliding DBD for Airflow Control: Structure and Dynamics. 46th AIAA Aerospace Sciences Meeting and Exhibit 7 - 10 Jan 2008 Grand Sierra Resort Hotel Reno, Nevada.Paper AIAA-2008-1367.
17. Roupassov D.V., Starikovskii A.Y., Development of Nanosecond Surface Discharge in Actuator Geometry. IEEE Transactions on Plasma Science Volume 36, Issue 4, Part 1, Aug. 2008 Page(s):1312 – 1313
18. Roupassov D., Nikipelov A., Nudnova M., Starikovskii A., Flow Separation Control by Plasma Actuator with Nanosecond Pulsed-Periodic Discharge. AIAA Journal (2009) 0001-1452 vol.47 no.1 (168-185)
19. Correale G., Popov I.B., Rakitin A.E., StarikovskiiA.Yu., Hulshoff S.J., Veldhuis L.L.M. Flow Separation Control on Airfoil with Pulsed Nanosecond Discharge Actuator. 49th AIAA Aerospace Sciences Meeting. Orlando, Florida. Jan 2011. Paper AIAA-2011-1079
20. Rios M., Nudnova M., Kindusheva S., Aleksahdrov N., Starikovskiy A. Fast Nonequilibrium Plasma Thermalization in N2-O2 Mixtures for Different Pulse Polarities. 49th AIAA Aerospace Sciences Meeting. Orlando, Florida. Jan 2011. Paper AIAA-2011-1275.
21. Samimy M., Kim J-H., Kastner J., Adamovich I., and Utkin Y. 2007 Active control of high-speed, and high-Reynolds number jets using plasma actuators. Journal of Fluid Mechanics 578: 305-330, 2007.
22. Starikovskii A.Yu., Nikipelov A.A., Nudnova M.M. and Roupassov D.V. SDBD plasma actuator with nanosecond pulse-periodic discharge Plasma Sources Sci. Technol. 18 No 3 (August 2009) 034015 (17pp)
23. Popov N.A. Fast gas heating in a nitrogen-oxygen discharge plasma: I. Kinetic mechanism 2011 J. Phys. D: Appl. Phys. 44 2852012
24. Pancheshnyi S., Nudnova M., and Starikovskii A. Development of a cathode-directed streamer discharge in air at different pressures: Experiment and comparison with direct numerical simulation. Physical Review E , 2005. 71, 016407 2005.
25. Gregory J., Enloe C., Font G., and McLaughlin T. Force Production Mechanisms of a Dielectric-Barrier Discharge Plasma Actuator. 45-th AIAA Aerospace Sciences Meeting and Exhibit, Reno, Nevada, USA, paper AIAA-2007-185
26. Phelps A.V., Pitchford L.C. Anisotropic scattering of electrons by N_2 and its effect on electron transport. Phys. Rev. A 31 (1985) 2932.
27. Nudnova M.M., Kindysheva S.V., Aleksandrov N.L., Starikovskii A.Yu. Fast gas heating in N_2/O_2 mixtures under nanosecond surface dielectric barrier discharge: the effects of gas pressure and composition. Phil. Trans. R. Soc. A 2015 373 20140330. 2015.

28. Flitti O. and Pancheshnyi S. Gas heating in fast pulsed discharges in N_2–O_2 mixtures. Eur. Phys. J. Appl. Phys. 45, 21001 (2009)
29. Florescu-Mitchell A.I. and Mitchell J.B.A. Dissociative recombination. Physics Reports. 430. (2006) 277-374
30. Willis C., Boyd A.W., Young M.J. and Armstrong D.A. Radiation chemistry of gaseous oxygen: experimental and calculated yields. 1970. Can. J. Chem. 48 1505.
31. Ghormley J.A., Hochanadel C.J. and Boyle J.W. Yield of ozone in the pulse radiolysis of gaseous oxygen at very high dose radiation. Use of this system as a dosimeter. 1969. J. Chem. Phys. 50 419.
32. Opaits, D., Zaidi, S., Shneider, L., Miles, R., Likanskii, A., and Macheret, S., "Improving Thrust by Suppressing Charge Build-up in Pulsed DBD Plasma Actuators," AIAA 2009-0487, January 2009.
33. Knight D. "Survey of aerodynamic drag reduction at high speed by energy deposition". Journal of Propulsion and Power 24: 1153-1167, 2008. 12
34. Corke TC, Enloe CL, and Wilkinson SP. "Plasma actuators for flow control". Annual Review of Fluid Mechanics 42: 505-529, 2010. 11
35. Miles R.B., "Plasma Flow Control, Fundamentals, Modeling, and Applications," von Karman Institute for Fluid Dynamics , Rhode Saint-Genese, Belgium VKI LS 2011-02, ISBN-13 978-2-87516-014-0 (2011)
36. Kinefuchi K., Starikovskiy A., and Miles R. "Control of Shock-Wave/Boundary-Layer Interaction Using Nanosecond-Pulsed Plasma Actuators". Journal of Propulsion and Power, 1-11. December 20, 2017.
37. Roupassov D.V., Zavyalov I.N., Starikovskii A.Yu., Saddoughi S.G. "Boundary Layer Separation Plasma Control Using Low-Temperature Non-Equilibrium Plasma of Gas Discharge". 44th AIAA Aerospace Sciences Meeting and Exhibit, 9 - 12 January 2006, Reno, Nevada. AIAA 2006-373
38. Patel,M.P., Ng,T.T., Vasudevan,S., Corke,T.C., Post,M.L., McLaughlin,T.E., Suchomel,C.F. "Scaling Effects of an Aerodynamic Plasma Actuator". 45th AIAA Aerospace Sciences Meeting and Exhibit 8 - 11 January 2007, Reno, Nevada AIAA 2007-635
39. Sidorenko A.A., Zanin B.Yu., Postnikov B.V., Budovsky A.D., Starikovskii A.Yu., Roupassov D.V., Zavialov I.N., Malmuth N.D., Smereczniak P., Silkey J.S. "Pulsed Discharge Actuators for Rectangular Wing Separation Control". 45th AIAA Aerospace Sciences Meeting and Exhibit 8 - 11 January 2007, Reno, Nevada. AIAA 2007-941
40. Roupassov D.V., Zavyalov I.N., Starikovskii A.Yu., Saddoughi S.G. "Boundary Layer Separation Control by Nanosecond Plasma Actuators". AIAA 2007-4530. Joint Propulsion Conference, 2007, Miami, Florida.
41. Visbal M.R., Gaitonde D.V. "Control of Vortical Flows Using Simulated Plasma Actuators". 44th AIAA Aerospace Sciences Meeting and Exhibit 9 - 12 January 2006, Reno, Nevada AIAA 2006-505.
42. Unfer T. and Boeuf J.P. "Modeling of a nanosecond discharge actuator", J. Phys. D: Appl. Phys. 42 194017 (2009)
43. Starikovskiy A. "On the role of 'hot' atoms in plasma-assisted ignition". Phil. Trans. R. Soc. A 2015 373 20140343; DOI: 10.1098/rsta.2014.0343. Published 13 July 2015

44. Aleksandrov N., Ponomarev A., Starikovskiy A. “Monte Carlo simulation of the effect of “hot” atoms on active species kinetics in combustible mixtures excited by high-voltage pulsed discharges”. Combustion and Flame 176, 181-190, 2017.
45. Correale G., Avallone F., Starikovskiy A. “Experimental method to quantify the efficiency of the first two operational stages of nanosecond dielectric barrier discharge plasma actuators”. Journal of Physics D: Applied Physics 49 (50), 505201. 2016